

REPORT DOCUMENTATION PAGE

Form Approved
OMB No. 0704-0188

The public reporting burden for this collection of information is estimated to average 1 hour per response, including the time for reviewing instructions, searching existing data sources, gathering and maintaining the data needed, and completing and reviewing the collection of information. Send comments regarding this burden estimate or any other aspect of this collection of information, including suggestions for reducing the burden, to the Department of Defense, Executive Service Directorate (0704-0188). Respondents should be aware that notwithstanding any other provision of law, no person shall be subject to any penalty for failing to comply with a collection of information if it does not display a currently valid OMB control number.

PLEASE DO NOT RETURN YOUR FORM TO THE ABOVE ORGANIZATION.

1. REPORT DATE (DD-MM-YYYY) 25-03-2011	2. REPORT TYPE Final Report	3. DATES COVERED (From - To) April 2008 - March 2011		
4. TITLE AND SUBTITLE YIP-08 - DEVELOPMENT AND APPLICATION OF A HIGH-SPEED THREE-DIMENSIONAL DENSITY MEASUREMENT TECHNIQUE FOR AERO-OPTIC APPLICATIONS		5a. CONTRACT NUMBER FA9550-08-1-0150		
		5b. GRANT NUMBER		
		5c. PROGRAM ELEMENT NUMBER		
6. AUTHOR(S) Thurow, Brian S. 211 Davis Hall Auburn, AL 36830 thurow@auburn.edu		5d. PROJECT NUMBER		
		5e. TASK NUMBER		
		5f. WORK UNIT NUMBER		
7. PERFORMING ORGANIZATION NAME(S) AND ADDRESS(ES) Auburn University 107 Samford Hall Auburn, AL 36849-0001 (334) 844-4428		8. PERFORMING ORGANIZATION REPORT NUMBER FOP 203150-128001-2000		
9. SPONSORING/MONITORING AGENCY NAME(S) AND ADDRESS(ES) AF Office of Scientific Research 875 N. Randolph St. Room 3112 Arlington, VA 22203 Joyce Burch Program Manager: Dr. Douglas Smith (douglas.smith@afosr.af.mil)		10. SPONSOR/MONITOR'S ACRONYM(S) AFOSR		
		11. SPONSOR/MONITOR'S REPORT NUMBER(S) AFRL-OSR-VA-TR-2012-0091		
12. DISTRIBUTION/AVAILABILITY STATEMENT Distribution A - Approved for Public Release				
13. SUPPLEMENTARY NOTES				
14. ABSTRACT A density measurement technique based on the planar laser induced fluorescence (PLIF) of acetone vapor was developed and shown to be practical for 2-D density measurements in a high-speed wind transonic wind tunnel. The technique was applied to visualize the shock induced separation and turbulent wake of a hemisphere mounted in a Mach 0.78 free stream. Density images clearly showed the presence of shock waves, a flapping wake structure and significant density drops within the cores of vortices formed in the separating free shear layer. The density drops could reach magnitudes up to 50% from the free stream value confirming that compressibility effects on density fluctuations within a weakly compressible shear layer are significant and cannot be explained through mixing models alone. Attempts to extend the technique to time-resolved or three dimensional density measurements (3-D LIF) using a MHz rate pulse burst laser system and high-speed camera were unsuccessful due to the unavailability of a sufficiently sensitive MHz rate camera. A background oriented Schlieren (BOS) imaging system was developed as a novel and cost-effective means to measure wavefront distortions in a large-scale flow facility.				
15. SUBJECT TERMS Compressibility, Fluid Mechanics, Diagnostics, Aero-optics				
16. SECURITY CLASSIFICATION OF: a. REPORT U		17. LIMITATION OF ABSTRACT UU	18. NUMBER OF PAGES 94	19a. NAME OF RESPONSIBLE PERSON Brian S. Thurow
				19b. TELEPHONE NUMBER (Include area code) 334-844-6827

Reset

Standard Form 298 (Rev. 8/98)

Prescribed by ANSI Std. Z39-18

Adobe Professional 7.0

FINAL REPORT

GRANT TITLE:

YIP - DEVELOPMENT AND APPLICATION OF A HIGH-SPEED THREE-DIMENSIONAL
DENSITY MEASUREMENT TECHNIQUE FOR AERO-OPTIC APPLICATIONS

AFOSR Grant Number: FA9550-08-1-0150

Submitted to:

Dr. Douglas R. Smith Civ USAF AFMC AFOSR/RSA
Flow Interactions & Control, Program Manager
Air Force Office of Scientific Research
875 N Randolph St, Suite 325, Room 3112
Arlington, VA 22203

ph: 703.696.6219
fax: 703.696.7320
email: douglas.smith@afosr.af.mil

Submitted by:

Brian S. Thurow, Ph.D.
W. Allen and Martha Reed Associate Professor
Department of Aerospace Engineering
211 Davis Hall
Auburn University, AL 36849-5338
(334) 844-6827
thurow@auburn.edu
<http://www.eng.auburn.edu/users/thurobs/>

Table of Contents

Executive Summary	3
Other Source of Information	4
I. Introduction	5
A. Motivation: Aero-Optics	5
B. Arrangement of Report.....	6
C. Background: Aero-Optics	6
D. Background: Acetone PLIF.....	10
E. Objectives of Present Work	19
II. Development of Acetone PLIF for Density Measurements.....	20
A. Basic Concept.....	20
B. Fluorescent Signal Equation.....	20
C. Image Processing.....	21
D. Signal Dependence on Pressure and Temperature	28
E. Conversion to Density.....	29
F. Measurement Uncertainty	30
G. Limitations:	32
1. Acetone Condensation.....	32
2. Signal Strength	34
3. Image Processing.....	34
4. Modeling of Acetone Photophysics	35
H. Conclusions	35
III. Transonic Test Section.....	36
A. Tunnel Design	36
B. Hemisphere Model	39
C. Facility Characterization	40
D. Acetone Seeder Design	43
IV. 2-D Density Measurements of the Turbulent Wake Behind a Hemisphere.....	46
A. Experimental Arrangement	46
B. Results and Discussion.....	48
1. Centerline Images.....	48
2. Off-Centerline Images.....	55

3. Separation Region – Centerline.....	59
C. Conclusions and Recommendations for Future Work with Acetone PLIF.....	60
V. Wavefront Measurements using Acetone PLIF.....	61
VI. Time-Resolved & 3-D LIF.....	67
VII. Background Oriented Schlieren Wavefront Sensor.....	71
A. Introduction	71
B. BOS Wavefront Sensor Concept.....	72
C. BOS Sensitivity	74
D. Test Case	78
E. BOS Wavefront Sensor Conclusions	84
VIII. Synergistic Activities	86
IX. Conclusions and Future Work	87
X. Works Cited	89

Executive Summary

A density measurement technique based on the planar laser induced fluorescence (PLIF) of acetone vapor was developed and shown to be practical for 2-D density measurements in a high-speed wind transonic wind tunnel. The random uncertainty in density measurements was estimated to be on the order of 8% without pixel binning and as low as 3% with pixel binning, thus showing that acetone PLIF is a viable technique for measurement of density in compressible flow fields.

The technique was applied to visualize the shock induced separation and turbulent wake of a hemisphere mounted in a Mach 0.78 free stream. Density images clearly showed the presence of shock waves, a flapping wake structure and significant density drops within the cores of vortices formed in the separating free shear layer. The density drops could reach magnitudes up to 50% from the free stream value confirming that compressibility effects on density fluctuations within a weakly compressible shear layer are significant and cannot be explained through mixing models alone.

Tools were developed to virtually project an optical wavefront through the measured density field. These tools allow for arbitrary selection of beam size, wavelength and propagation direction. Preliminary results examining a single angle of propagation (30 degrees back) and beam size (1/3 diameter of hemisphere) show that the most significant source of aero-optic aberrations are due to the flapping motion of the overall wake more so than the density fluctuations associated with vortices in the separating shear layer.

Attempts to extend the technique to time-resolved or three dimensional density measurements (3-D LIF) using a MHz rate pulse burst laser system and high-speed camera were unsuccessful due to the unavailability of a sufficiently sensitive MHz rate camera. Cameras tested in this study, while useful for 3-D flow visualization, were estimated to be up to 3 orders of magnitude less sensitive than the most sensitive high-speed cameras available. 3-D LIF measurements, however, were determined to be viable given the proper instrumentation.

A background oriented Schlieren (BOS) imaging system was developed as a novel and cost-effective means to measure wavefront distortions in a large-scale flow facility. The technique only requires a camera, random background and a light source. Preliminary results indicate that the technique has sufficient sensitivity for aero-optic measurements with the potential to yield better spatial resolution and be applied for the measurement of larger aperture wavefronts than a Shack-Hartmann wavefront sensor.

For future work, it is recommended to continue development and application of the technique with enhanced instrumentation such that larger field of views can be visualized and the 3-D potential of the technique can be realized. Continued study of the wake behind a hemisphere under varying conditions (i.e. varying Mach number, incident boundary layer state, etc.) as well as the study of other canonical flows (e.g. compressible free shear layers) is also recommended.

Other Source of Information

Peer Reviewed Journals

- Thurow, B., Reid, J. Z., and Lynch, K., “Planar density measurements in a compressible flow field using acetone PLIF” under preparation for submission to AIAA J., 2011.
- Thurow, B. and Bichal, A. “Development of a Background Oriented Schlieren-Based Wavefront Sensor,” under preparation for submission to Measurement Science and Technology, 2011.

Thesis

- Reid, J. Z., Development of a Direct Density Measurement Technique for Aero-Optic Analysis of a High-Velocity, Compressible Flow Field, M.S. Thesis, Auburn University, March 2011.

Professional Conference Proceedings

- Reid, J. Z., Lynch, K.P. and Thurow, B.S., “Density Measurements of a High-Speed Compressible Flow Field Using Acetone Planar Laser Induced Fluorescence (PLIF),” 49th Aerospace Sciences Meeting and Exhibit, Orlando, FL, January 2011.
- Lynch, K., Reid, J. and Thurow, B., “Further Development of Acetone Laser Induced Fluorescence for Aero-Optics,” AIAA Paper 2010-4844, 40th AIAA Fluid Dynamics Conference, Chicago, IL, June 2010.
- Bichal, A and Thurow, B., “Development of a Background Oriented Schlieren-Based Wavefront Sensor for Aero-Optics,” AIAA Paper 2010-4842, 40th AIAA Fluid Dynamics Conference, Chicago, IL, June 2010.
- Reid, J.Z., Wall, D., Lynch, K. and Thurow, B., “Initial Development of Acetone Laser Induced Fluorescence (LIF) for Aero-Optics,” AIAA Paper 2009-4295, 39th AIAA Fluid Dynamics Conference, San Antonio, TX, June 2009.
- Thurow, B. and Lynch, K., “Preliminary Development of a High-Speed 3-D Laser Induced Fluorescence Technique,” AIAA Paper 2009-1446, 47th AIAA Aerospace Sciences Meeting Orlando, Florida, January 2009

Student Conference Proceedings

- Lynch, K., “Development of Three-Dimensional Acetone LIF Using a Pulse Burst Laser System,” Proceedings of the AIAA 2009 Southeastern Regional Student Conference, Huntsville, AL, April 2-3, 2009. ***Received 2nd place in Undergraduate Student Paper Competition**
- Wall, D. “Design of a Solid-Wall Transonic Wind Tunnel,” Proceedings of the AIAA 2009 Southeastern Regional Student Conference, Huntsville, AL, April 2-3, 2009.

I. Introduction

A. Motivation: Aero-Optics

The field of aero-optics has received increasing attention over the last few decades as the number of applications involving lasers onboard aircraft, such as targeting and directed energy systems, continues to grow. The most well known and largest scale of these systems is the Airborne Laser (ABL) program in which a megawatt-class chemical oxygen iodine laser (COIL) laser is mounted on a Boeing 747-400 aircraft. The ABL's mission is to identify, target and destroy missiles soon after launch. The effectiveness of this system and ones like it depend heavily on the efficiency with which the energy in the laser beam can be delivered to the target. The density-varying (i.e. index-of-refraction) flow field that surrounds the near field of the aircraft, however, causes an adverse effect by distorting the optical wavefront as it passes through the flow field, causing such things as beam jitter, steering and defocus, all of which contribute to a significant reduction in the amount of energy delivered to the target. The study of these phenomena is known as aero-optics.

Quantitatively, the distortion of an optical wavefront can be described by variations in the optical path length (OPL), or more commonly, the optical path difference (OPD):

$$OPL(x, y, t) = \int_{z_1}^{z_2} n(x, y, z, t) dz \quad (1)$$

$$OPD(x, y, t) = OPL(x, y, t) - \overline{OPL(x, y, t)} \quad (2)$$

where z is taken as the direction of light propagation. The index of refraction is related to the flow field density by:

$$n = 1 + K\rho \quad (3)$$

where K is the Gladstone-Dale constant ($2.23 \times 10^{-4} \text{ m}^3/\text{kg}$ for air) and ρ is the density in kg/m^3 . Thus, *the distortion of an optical wavefront is the integrated effect of the three-dimensional density (index-of-refraction) field through which the beam passes*.

Conventional flow diagnostics, however, are unable to provide direct measurements of the density field and must rely on indirect methods (e.g. velocity field measurements or line-of-sight integrated techniques such as Schlieren imaging) to infer details about the density field. Although direct wavefront measurements are also possible, this only reveals information about the integrated effect of the density field, thus obscuring the underlying flow physics that led to the distortion in the first place. Furthermore, unsteady flow fields, such as those associated with turbulent boundary layers and separated shear layers, are marked by fluctuating timescales (several kHz) beyond the limit of current adaptive optic systems. Nonetheless, past investigations have succeeded in using a variety of experimental methods to characterize the spatial and temporal scales of turbulent flow fields and the resulting wavefront aberrations [(Truman and Lee 1990) (Chew and Christiansen 1993) (Hugo, et al. 1997) (Dimotakis, Catrakis and Fourguette 2001) (Yanta, et al. 2000) (Jumper and Fitzgerald 2001) (Stanek, et al. 2002) (Thurow, Samimy, et al. 2003) (Thurow, Samimy and Lempert 2003) (Wyckham 2003)

(Aguirre, et al. 2005)]. A common limitation of these efforts, however, is the lack of density field data. For the design of a turret or flow control system to mitigate aero-optic effects, however, direct knowledge of the flow induced density changes is critical.

B. Arrangement of Report

Based on the preceding discussion, there is a clear need in the field of aero-optics (and fluid dynamics, in general) for diagnostics capable of making spatially resolved density measurements in high-speed flows. The development of such a diagnostic was the primary objective of this work and the main topic of this report. The technique chosen to achieve this objective is planar laser induced fluorescence (PLIF) of acetone vapor seeded into a flow field. This technique is shown here to be a viable technique for such measurements and has the tantalizing potential to be extended to a 3-D measurement technique using high repetition rate lasers and cameras.

Before proceeding, a brief review of the most relevant background material is provided below. Section II then picks things up with a description of the acetone PLIF technique and the developments made over the course of this project to adapt its use for density measurements in high-speed turbulent flow fields. This is followed by a description of a transonic wind tunnel test section (Sec. III) built specifically to test these ideas out (Sec. IV). Sec V describes some of the tools and methodologies developed for using 2-D density data for the prediction of aero-optic wavefront distortion. Sec VI discusses attempts to extend the technique for acquisition of time-resolved or 3-D density measurements. In a tangential, but related effort, Sec. VII describes the development of a new wavefront sensor based on the principles of Background Oriented Schlieren Imaging. Sec. VIII lists a number of synergistic (collaborative) relationships between the PI and the Air Force community that are the direct result of the PI's involvement with this project. Lastly, Sec. IX gives conclusions based on this work and makes recommendations for any future work conducted along these lines.

C. Background: Aero-Optics

In this section, a brief background on the most relevant aspects of aero-optics is provided. This section can be skipped by readers already familiar with the aero-optics problem.

Wavelength Dependence

The severity of the aero-optic distortion is not only dependent on the density fluctuations as described in Eqs. 1 – 3, but is also dependent on the wavelength of the wavefront passing through the flow field, with the distortion of a wavefront often normalized by the wavelength of light, OPD/λ . One common measure of the degree of wavefront distortion is the Strehl ratio (SR). The Strehl ratio is the ratio of the maximum beam irradiance with distortion relative to that without distortion:

$$SR(t) = \frac{I(t)}{I_0} \quad (4)$$

Under the assumption that the beam aperture is large relative to the spatial scale of distortions in the flow, SR can be statistically related to variations in OPD and the wavelength of light through:

$$\overline{SR} = \exp \left[- \left(\frac{2\pi OPD_{rms}}{\lambda_{wf}} \right)^2 \right] \quad (5)$$

This indicates that the effect of flow induced aberrations is significantly worse at shorter wavelengths of light. Consider that the directed energy source for the airborne laser project, for example, is a chemical oxygen-iodine laser (COIL), which has a wavelength of approximately 1315 nm (Jumper and Fitzgerald 2001). This wavelength is relatively short when compared with other lasers, such as a CO₂ laser which has a wavelength of approximately 10,600 nm. This would imply that longer wavelength laser systems would be more beneficial; however, one must also consider that the value of I_0 decreases as the wavelength increases as the size of the airy disc (shape of a beam at the focal point) is directly proportional to the beam wavelength. Thus, there are competing mechanisms that determine the selection of laser wavelength for a particular application.

In terms of the work reported here, direct density measurements are advantageous as they provide the ability to consider virtual wavefronts of varying wavelength, aperture size and direction, which can be propagated through the flow field to determine the amount of distortion that would occur for a wide range of optical parameters. Thus, for a given flow geometry, significantly fewer experiments are required to understand the resulting aero-optic effects.

Recent Aero-Optic Work and Research

A significant body of work in aero-optics has accumulated over the last couple decades leading up to this work. This work has included traditional aero-optic distortion measurement techniques, flow control attempts, flow visualization experiments, modeling efforts, and an aero-optic distortion measurement technique using acetone PLIF. Only a brief portion of this work is highlighted in this report with the emphasis here being on studies focused directly on the physical flow mechanisms responsible for aero-optic distortion.

Recently, several groups [e.g. (Gordeyev, Hayden and Jumper 2007), (Gordeyev, Post, et al. 2007)] have investigated the aero-optic distortion of a hemisphere mounted on top of a cylinder/pedestal with a flat or conformal aperture window. Wavefront measurements included time-resolved point-based wavefront measurements using a Malley probe and spatially resolved measurements using a Shack-Hartmann wavefront sensor. In these experiments, the wavefront propagation angle was varied by rotating the turret to various azimuthal/elevation positions such that the wavefront distortion could be categorized over a wide range of look angles. These tests were conducted over several Mach numbers where it was observed that the distortion increased with Mach number, freestream density, and azimuth angle. In particular, and as expected, angles propagating through the shear layer/wake region exhibited the largest amount of wavefront distortion. Conformal aperture/window data revealed that separation occurs later than for the flat window turret, but is not steady. The conformal aperture/window aero-optic distortion data is more random than the aero-optic distortion data for the flat window turret.

To go along with traditional wavefront measurements of turret flow fields, several flow control techniques have been investigated to mitigate the aero-optic distortions [(S. Gordeyev, E. Jumper and B. Vukasinovic, et al. 2009), (Vukasinovic, et al. 2009)] investigated the use of suction/blowing jet actuators on turrets. The purpose of these actuators is to delay flow

separation over the surface of the turret, which will enable larger backward facing angles for a laser beam to exit the turret with less aero-optic distortion. In addition, the purpose of these actuators is to dissipate and decrease downstream turbulence. Several backward facing angles and Mach numbers (0.3, 0.4, and 0.5) were investigated with different combinations of jet actuators and jet velocities. The OPD_{rms} was measured with a Malley probe and for the most part there was an improvement in the OPD_{rms} with the jet actuators as opposed to the same cases with no jet actuators. Other flow control techniques, such as work by (Cain, et al. 2008), have looked into fairing designs for the turret, coupled with aeroacoustics. For information on additional flow control techniques see (Gordeyev and Jumper 2010).

Modeling efforts have also been made in order to better characterize weakly compressible flows, in particular separated shear layer flows, such that experiments are not needed for every different geometry considered. The work of (Jumper and Fitzgerald 2001), (E. Jumper 2006), and (Fitzgerald and Jumper 2004) established the Weakly Compressible Model that uses the unsteady Euler equations, the isentropic relationship between temperature and pressure, and the ideal gas law in an iterative process in order to find pressure, temperature, and density at all points in the flow from velocity field data. The main purpose of this model is to allow efficient incompressible flow solvers to be used for prediction of aero-optic phenomena with initial results showing excellent agreement between actual and predicted wavefronts.

(Rennie, et al. 2008) further evaluated the accuracy of the WCM using CFD (COBALT) to find the temperature, pressure, and density fields of the same velocity field (compressible, separated shear layer flow). It was found that the WCM predicts the pressure field quite well, as seen in Figure 1, but displays significant errors in the prediction of the temperature and density fields (see Figure 2). Complicating matters, however, is the fact that experimentally acquired wavefront data in weakly compressible shear layers is more consistent with the WCM version of density fluctuations as opposed to the CFD determined values. In the absence of experimental density data for proper validation, the accuracy of the WCM remains an open question.

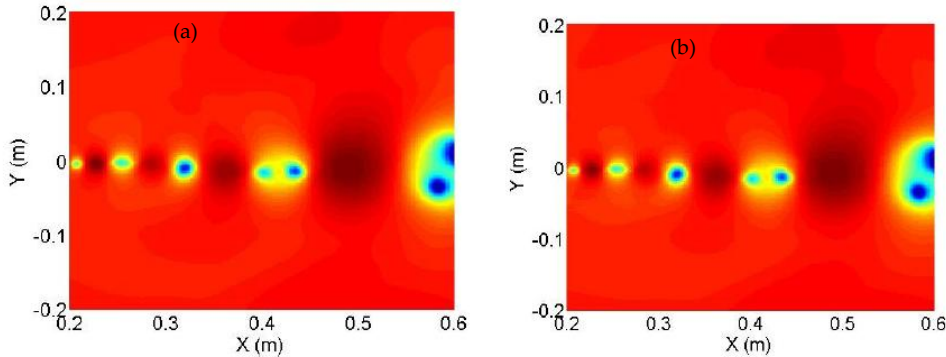


Figure 1: Calculated Pressure Field (a) CFD – COBALT (b) WCM [(Rennie, et al. 2008)]

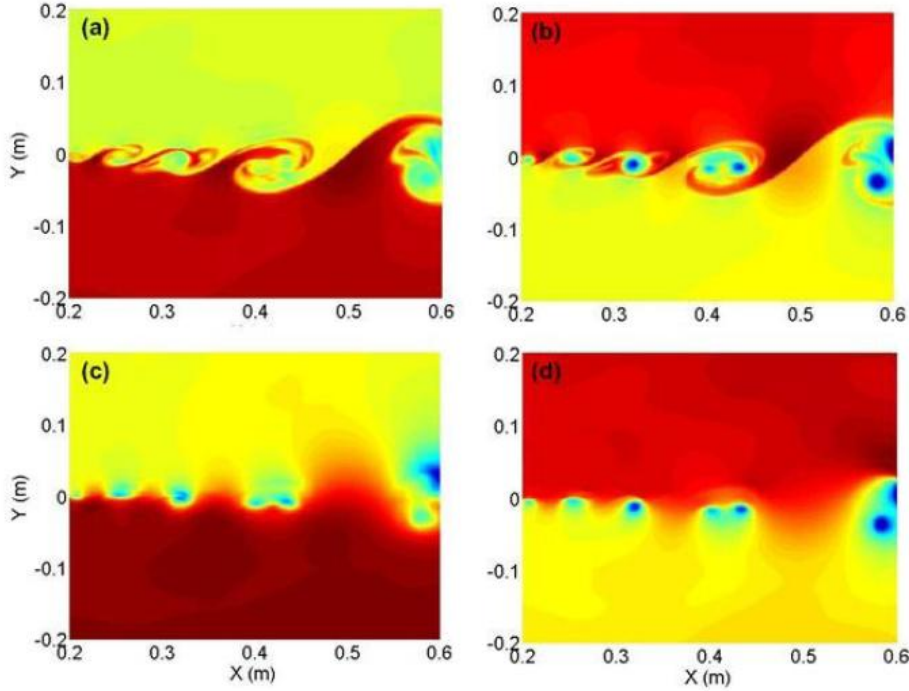


Figure 2: Calculated Static Temperature Field (a) CFD – COBALT (c) WCM
 Calculated Density Field (b) CFD – COBALT (d) WCM [Rennie et al. (2008)]

Even without full validation of the WCM, its very development spurred new explanations for the aero-optic behavior observed in weakly compressible shear layers. Of particular significance, they determined that local pressure changes play a significant role in creating density fluctuations (and thus distortions) as opposed to the traditional school of thought where pressure fluctuations are considered negligible such that density is directly tied to fluctuations in temperature. Although somewhat obvious in hindsight, it was determined that the shear layer flow region possesses well-defined, vortex structures that create significant streamline curvature and are associated with low pressure regions at the core that results in a significant drop in density as well. This resulting drop in density is of greater magnitude (i.e. more detrimental) than would be explained by pure mixing between two streams of different temperature/density. In addition, there are also regions of high density and high pressure in the braid region between structures.

Aero-optic measurements in a compressible shear layer were also conducted using acetone PLIF in the work of (Catrakis, Garcia and Natham 2006), (H. Catrakis, Aero-Optical Wavefront Propagation and Refractive Fluid Interfaces in Large-Reynolds-Number Compressible Turbulent Flows 2006). Related works can also be found in (Catrakis, Aguirre and Ruiz-Plancarte 2002) and (Dimotakis, Catrakis and Fourguette 2001). The impetus and approach in their work was similar to that illustrated in this report; however, there are some key differences between their work and this work that must be highlighted. In Catrakis et al.'s work, a compressible shear layer was formed using a wall jet exhausting into a large pressurized tank. The jet flow was seeded with acetone vapor and visualized using laser-induced fluorescence. It is important to note that the tank was not seeded with acetone vapor. The resulting PLIF images were thus a

measure of the local number density of acetone molecules contained in the flow at a particular point in space. As one stream was unseeded, this measure will thus be dominated by the degree of mixing between the seeded and unseeded streams. The critical assumption implicitly made by Catrakis et al., however, was that the flow density at any point can also be modeled as a function of the local mixing between high-speed (seeded, low density) and low-speed (unseeded, high density) flow. It was under this assumption that their work proceeded. A major limitation of this assumption, however, is that it neglects possible changes in density due to true compressibility effects. Catrakis et al. may have felt justified in this assumption due to the statistically small magnitude of pressure fluctuations; however, as shown by Jumper (and discussed in the previous paragraph), fluctuations in pressure, density and temperature due to compressibility effects can be a significant, and even, dominant mechanism of wavefront distortion. Thus, Catrakis et al.'s approach to the aero-optics problem neglected one of the most important physical mechanisms of aero-optics.

In contrast, the method in which acetone PLIF is applied in this work is not affected by this assumption. Rather, an approach was developed whereby the entire flow is uniformly seeded with acetone vapor such that the acetone mole fraction is a constant. In this case, the observed PLIF signal is a direct function of the local flow density so that a true density measurement can be made. To accomplish this goal, however, an accurate understanding of how the PLIF signal varies with pressure, density and temperature is necessary. Further background on acetone PLIF is discussed in the next section.

D. Background: Acetone PLIF

Planar laser induced fluorescence (PLIF) is based on the absorption and fluorescence of laser light by molecules either already present or seeded into a flow field. Using an appropriate light source with strong spectral overlap, light can be efficiently absorbed by the molecule, raising its energy level. For acetone PLIF, a 266 nm laser sheet passes through the flow field of interest, the acetone molecules absorb the 266 nm light, and a fraction of the acetone molecules fluoresce with a signal that can be captured using a CCD camera. The fluorescence signal can be correlated to a density value, allowing a density field to be determined from an acetone PLIF image.

Photophysics/Characteristics of Acetone (CH_3COCH_3)

Acetone was chosen as the tracer molecule for this work because of the favorable characteristics it possesses, which include low cost, high vapor pressure, safe handling characteristics, and a broadband absorption spectrum. In addition, acetone is a well studied molecule [e.g. (Thurber 1999), (Lozano 1992)] due to its ease of access and common use as a fuel tracer in combustion diagnostics. It has broadband absorption and fluorescence spectrums of 225-320 nm and 350-550 nm, respectively. The absorption peaks at 260-290 nm and thus overlaps with the fourth harmonic output of Nd:YAG lasers. The fluorescence, on the other hand, peaks at 435 nm and 480 nm, which is in the visible regime and compatible with many CCD cameras. Acetone has short fluorescence and phosphorescence lifetimes of 5 ns and 200 μ s, respectively with the phosphorescence fully quenched in flow fields with relatively small partial pressures of oxygen such that the phosphorescence can be considered negligible in the current work[(Thurber 1999), (Tran, Acetone Planar Laser-Induced Fluorescence and Phosphorescence for Mixing

Studies of Multiphase Flows at High Pressure and Temperature 2008), (Hartwig 2010), (Bryant, Donbar and Driscoll 2000), (Kohse-Hoinghaus and Jeffries 2002)].

Briefly, acetone fluorescence occurs when molecules are energized to a level of the S₁ first excited singlet state from the S₀ ground electronic state (Tran, Kochar and Seitzman, Measurements of Acetone Fluorescence and Phosphorescence at High Pressures and Temperatures 2006). In order to return to the ground electronic state, there are five possible events that the acetone molecules can experience (a combination of several of these is also possible). These events are fluorescence, relaxation through vibration, internal conversion, intersystem crossing to the triplet state, and collisional quenching (Tran, Kochar and Seitzman, Measurements of Acetone Fluorescence and Phosphorescence at High Pressures and Temperatures 2006). For more in-depth information on these five events, see (Thurber 1999), (Hartwig 2010), (Tran, Kochar and Seitzman, Measurements of Acetone Fluorescence and Phosphorescence at High Pressures and Temperatures 2006). Relaxation through vibration takes the energy of the acetone molecules to a lower energy level within S₁ where any of the five events can still occur. Internal conversion, collisional quenching, and fluorescence take the energy of the acetone molecules to the S₀ ground electronic state. Acetone molecules that have intersystem crossing to the triplet state can also experience events closely related to those in the singlet state. However, instead of fluorescence, longer time-elapsed phosphorescence is experienced (Tran, Kochar and Seitzman, Measurements of Acetone Fluorescence and Phosphorescence at High Pressures and Temperatures 2006).

By having different events that could de-excite the acetone molecules in terms of their energy at multiple energy levels, the fluorescence of acetone molecules is broadband. If the excited acetone molecules move to a lower energy level within S₁ due to vibrational relaxation, for example, any of the five events could occur to continue to move the acetone molecules all the way to the ground state or to a lower energy level. Fluorescence can occur at any point as the acetone molecules are moving to lower and lower energy levels.

Advantages and Disadvantages of Acetone

Acetone was chosen as the seeding particle for this work because it is relatively inexpensive, it is safe to humans, it has a high vapor pressure at standard atmospheric conditions, and it has a broadband absorption spectrum. Being inexpensive and safe to humans enables acetone PLIF to be used for high flow rate applications. The fact that acetone has a high vapor pressure at atmospheric conditions is important because in this work the acetone was seeded in the liquid form far upstream of the test section and had to evaporate before entering the test section. The broadband absorption spectrum in the ultra violet is important because 266 nm light, the fourth harmonic of Nd:YAG, is rather easily obtained using a KDP or BBO crystal. Finally, acetone is well established in literature as a molecular tracer for PLIF and its photophysical behavior is well-characterized. (Thurber 1999), (Lozano 1992), (Hartwig 2010), (Kohse-Hoinghaus and Jeffries 2002), (Tran, Kochar and Seitzman, Measurements of Acetone Fluorescence and Phosphorescence at High Pressures and Temperatures 2006)

Acetone for all of its advantages still has two main disadvantages. The first disadvantage is acetone is very corrosive to many types of rubber and plastic. Before using acetone in an experimental manner it is highly advised to consult a chemical properties sheet which should outline materials that acetone corrodes and materials that acetone does not corrode. In this work,

liquid acetone was only injected in short bursts, so the wetted parts that the liquid acetone came into contact with were only exposed momentarily and then the acetone evaporated. In addition, most (but not all) of the wetted materials were either metal or were compatible with acetone. The second disadvantage is there is a limit to the acetone mole fraction. If too much acetone is injected into a flow field in an effort to increase the signal, the acetone will remain in its liquid state or condense in regions of the flow with lower temperatures. Thus, care must be taken to determine an adequate acetone mole fraction that prevents condensation, while also reaching a maximum in fluorescence signal. Condensation is discussed in more detail later on.

Comparison of Acetone to Other Flow Tracers

There are other flow tracers that have been used for PLIF experiments besides acetone. These tracers are either seeded into the flow field or they naturally exist in the flow field. (Lozano 1992) performed extensive research into different flow tracers used for PLIF and although this work eventually centered upon biacetyl and acetone, discussion of other tracers is also provided. For example, NO PLIF has been performed in the past by (Danehy, et al. 2006). This tracer was determined to not be a possible tracer candidate for the work in this thesis for multiple reasons. First and foremost, NO is hazardous and the work presented in this thesis involves high-flow rates, so large amounts of NO would have been too dangerous to use for PLIF. In addition, the harmonics of Nd:YAG lasers were used in this work for excitation purposes (specifically 266 nm, the 4th harmonic). The harmonics of these lasers could not be used to excite NO as NO is excited by approximate wavelengths of 193 nm, 214 nm, 226 nm, 236 nm, and 248 nm. Finally, oxygen causes quenching of the fluorescence of NO. The flow field in this work is mainly air and thus oxygen quenching of fluorescence would certainly exist. Biacetyl was also determined to not be a possible tracer candidate for this work. Lozano explained that biacetyl is only a viable tracer for obtaining phosphorescence data. In addition, biacetyl has a phosphorescence lifetime that is long and it cannot be used as a tracer in flows that contain oxygen and flows that are not isothermal. The current work involves a flow field that does not meet these two requirements as the flow is almost entirely dry air and it is not isothermal. Based upon the characteristics of acetone and the comparison to other PLIF flow tracers established in literature, acetone was chosen as the ideal flow tracer for this work.

Recent Acetone Photophysics and Acetone PLIF Work

The photophysics of acetone have been studied extensively in order to better understand the viability of acetone as a flow tracer in flow diagnostic experiments. In addition to this research into photophysical behavior, acetone PLIF experiments have been performed in multiple flow fields to investigate temperature, concentration/mixing, convective velocity, and index of refraction fields. The information presented here is meant to show the reader that acetone PLIF is a widely used flow diagnostic technique and to provide the reader with a frame of reference so they can truly appreciate the work presented in this thesis with acetone PLIF and its contribution to previous work.

Acetone Photophysics Work

A large portion of acetone PLIF research has been performed at Stanford University, such as modeling work as well as experimental work with the PLIF of acetone and other flow tracers. (Thurber 1999) developed a fluorescence quantum yield (ϕ) model for acetone based upon personal research and past research of others that takes into account excitation wavelength, temperature, pressure, and type of bath gas. Thurber performed flow cell measurements where fluorescence signal and absorption cross-section data for acetone in a nitrogen bath gas were obtained for different excitation wavelengths and temperatures at a constant pressure of 1 atm. Fluorescence quantum yield data was calculated from the fluorescence signal and absorption cross-section data. Thurber's absorption cross-section verses temperature data for different excitation wavelengths can be extrapolated or interpolated at specific temperature values. Thurber also performed static gas cell measurements where absorption cross-section and fluorescence signal data were obtained for acetone in multiple bath gases while the temperature was held constant (297 K, room temperature) and the pressure and excitation wavelength were varied. The fluorescence quantum yield model was optimized to fit the data from literature and the data from the static and flow cell experiments.

Thurber's final fluorescence quantum yield model is based upon the fluorescence quantum yield equation seen in Equation 6. The terms in this equation are k_{NR} (rate of non-radiative relaxation/rate of intersystem crossing), k_f (rate of fluorescence), k_{coll} (rate of collision), and k_{O_2} (rate of oxygen quenching).

$$\phi = \frac{k_f}{k_f + k_{coll} + k_{NR,1} + k_{O_2}} + \sum_{i=2}^{N-1} \left(\frac{k_f}{k_f + k_{coll} + k_{NR,i} + k_{O_2}} \prod_{j=1}^{i-1} \left[\frac{k_{coll}}{k_f + k_{coll} + k_{NR,j} + k_{O_2}} \right] \right) + \frac{k_f}{k_f + k_{NR,N} + k_{O_2}} \prod_{j=1}^{N-1} \left[\frac{k_{coll}}{k_f + k_{coll} + k_{NR,j} + k_{O_2}} \right] \quad (6)$$

Thurber also provides a source code (C++) for a simpler version of the final fluorescence quantum yield model where pressure, temperature, and excitation wavelength are inputs and the fluorescence quantum yield is the output. In this original source code, k_{coll} is only calculated for acetone in a nitrogen bath gas. However, Thurber outlines steps to modify the bath gas.

In Thurber's work, the acetone mole fraction was very small and the bath gas mole fraction was approximately 1. Thus, the fluorescence quantum yield model assumes that the bath gas mole fraction is also approximately 1. This enabled Thurber to model collision frequency, a component of k_{coll} , in the fluorescence quantum yield model with a Lennard-Jones potential. The Lennard-Jones potential is typically used to calculate collision frequency between non-polar molecules. Acetone is a polar molecule and thus the Stockmayer potential should technically be implemented instead of the Lennard-Jones potential when modeling collisions between acetone molecules in order to include the dipole moment (Stockmayer potential is similar to the Lennard-Jones potential, except dipole interactions are not included in the Lennard-Jones potential as they are in the Stockmayer potential, (Hirschfelder, Curtiss and Bird 1954)). However, for low acetone mole fraction applications, such as in Thurber's work, the Lennard-Jones potential and Stockmayer potential yield similar results, in terms of collision frequency, within a few percent. The work presented in this thesis conveniently uses a small acetone mole fraction as well, approximately 3%, and thus Thurber's model is assumed to be valid in this regard.

In contrast, for flow fields with a significant acetone mole fraction, Thurber's model should be updated where the Stockmayer potential is used instead of the Lennard-Jones potential when modeling collisions between acetone molecules. Also, for collisions of the bath gas molecules

(non-polar) with acetone molecules (polar), the calculated terms for molecule collision diameter and collision potential energy should be updated to include the dipole moment (Thurber 1999) (these parameters do not need to be modified for collisions between polar acetone molecules). The equations and variables for updating these terms are clearly presented in (Hirschfelder, Curtiss and Bird 1954). Thurber explains the reasoning for using Lennard-Jones in this model instead of Stockmayer potential in much greater detail in (Thurber 1999). Additional information on Lennard-Jones potential and Stockmayer potential can be found in (Reid, Prausnitz and Sherwood 1977), (Brokaw 1969), (Mourits and Rummens 1977), and (Troe 1977).

Photophysical work with acetone has also been conducted at other universities/research facilities to test Thurber's model under different conditions and to offer improvements to the model. (Hartwig 2010) performed laboratory experiments to test Thurber's fluorescence quantum yield model at high pressure and temperature conditions. Based upon these experiments and results, which were performed for an excitation wavelength of 282 nm, Hartwig modified Thurber's model so it better fit his data and other data established in literature (excitation wavelengths in addition to 282 nm), including Thurber's original data. (Tran 2008) investigated the photophysics of acetone vapor, as well as the photophysics of liquid acetone. Tran tested the validity of the fluorescence quantum yield models of Thurber at high pressure and temperature values. (Bryant, Donbar and Driscoll 2000) performed static gas cell measurements to test the behavior and sensitivity of the acetone fluorescence signal at low temperature and low pressure values. The pressure and temperature values tested were from 0.1-1atm and 240-295 K, respectively. It was found that for the temperature values investigated, the acetone fluorescence signal increased by 8% as the temperature increased. It was found that for the pressure values investigated, the acetone fluorescence signal fluctuated by +/-5%.

Researchers have updated variables in Thurber's model and suggestions have been made in order to improve Thurber's original model or in order to modify it to fit specific experimental data [(Hartwig 2010), (Tran 2008), (Braeuer, Beyrau and Leipertz 2006), (Koch, et al. 2004)]. The reader should keep in mind that Thurber's model is not perfect and it can be improved. With that being said, the work presented in this thesis was not specifically about the photophysics of acetone or other flow tracers for PLIF, as an entire dissertation can comprise that sort of work (see (Lozano 1992)). Instead this work was about testing the validity of using acetone as a flow tracer for a flow diagnostic technique (PLIF) that would enable density field calculation in a high-velocity, compressible flow field. Therefore, Thurber's fluorescence quantum yield model in its original form in (Thurber 1999) was used, with the only modifications coming in the form of the additional oxygen quenching term and updating the model to take into account bath gas type.

Temperature, Concentration/Mixing, and Convective Velocity Measurements with Acetone PLIF

As photophysical work on acetone has progressed, so have the acetone PLIF experiments and their use as a flow diagnostic tool. (Thurber 1999) showed the viability of acetone PLIF to obtain temperature field data for the flow over a heated cylinder and the flow of a heated jet subject to a cross-flow. The cylinder was very small in scale ($D = 3$ mm) and the flow was very slow ($Re=6$). At 248 nm excitation, quality fluorescence images were obtained and converted to temperature data, as seen in Figure 3.

For the heated jet in cross-flow experiments, the jet and cross-flow had the same uniform acetone mole fraction and pressure and only the temperature varied. Fluorescence images of this flow field were obtained with initial excitation of 266 nm and were converted to temperature data, as seen in Figure 4.

Thurber also introduced a technique of using two excitation wavelengths (248 nm and 308 nm, although 266 nm and 308 nm could also be used) and using the resulting fluorescence images at each excitation wavelength to yield final results of temperature and pressure data (if acetone mole fraction is uniform) or temperature and acetone mole fraction data (if pressure is uniform). Another experiment of note is the work of (Kearney and Reyes 2003) who used acetone PLIF to investigate the temperature fields created by Rayleigh-Bénard convection between a hot and cold plate.

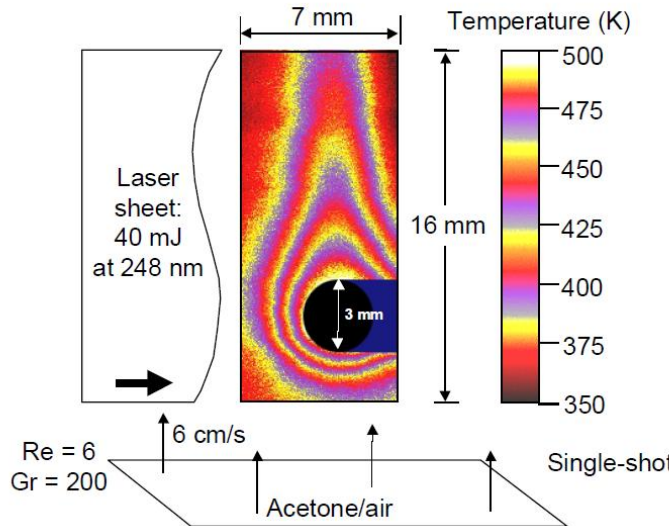


Figure 3: Temperature Field for Flow Over Heated Cylinder [Thurber (1999)]

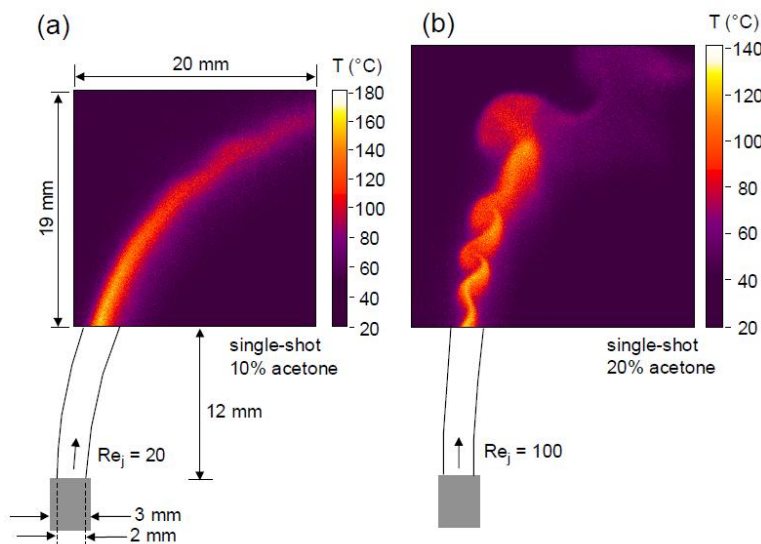


Figure 4: Temperature Field of Heated Jet in Cross-Flow (a) $Re=20$ (b) $Re=100$ [(Thurber 1999)]

In addition to temperature measurements with acetone PLIF, concentration/mixing experiments have also been performed. (Nygren, et al. 2002) successfully performed 3-D acetone LIF (acetone mixed with ethanol) to study fuel location and concentration in an HCCI (homogenous charge combustion ignition) engine. Information about the combustion can be drawn from this data. (Choi, Ko and Chung 2002) used acetone PLIF (excitation $\lambda=280\text{nm}$) to study fuel/air mixing in a non-premixed vortex ring, as seen in Figure 5. Acetone vapor and propane were mixed in a reservoir and then a speaker created the vortex ring.

The amplitude of the speaker was varied and the mixing of fuel and air in the inner ring of the vortex ring was affected. It was found that lower amplitude values resulted in greater mixing of fuel and air in the inner ring of the overall vortex ring. The temporal characteristics of the vortex ring were also investigated (Schlieren and acetone PLIF) and diameter of the inner ring of the overall vortex ring was found to grow over time, as seen in Figure 6. Also, mixing increased throughout time.

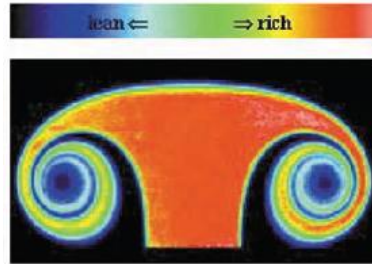


Figure 5: Acetone PLIF Image of Vortex Ring Mixing of Fuel/Air [(Choi, Ko and Chung 2002)]

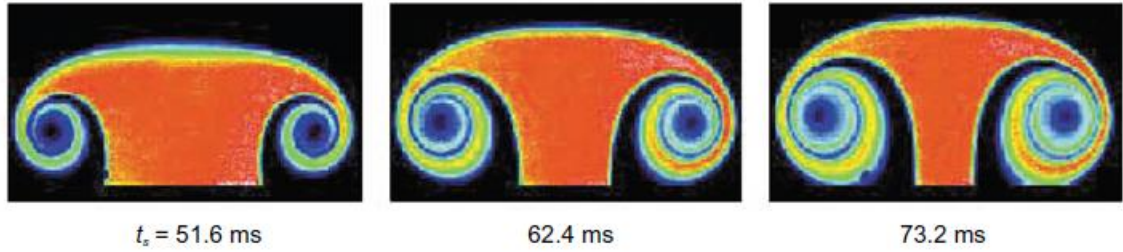


Figure 6: Temporal Acetone PLIF Images of Vortex Ring Mixing [(Choi, Ko and Chung 2002)]

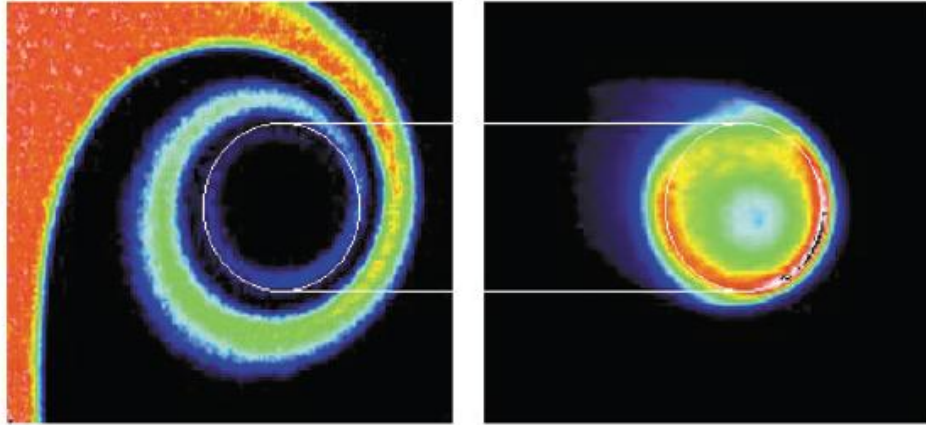


Figure 7: Vortex Ring Flame Propagation (a) Acetone PLIF Image of Vortex Ring Mixing Structure (b) Direct Image of Intensity of Propagating Flame [(Choi, Ko and Chung 2002)]

Propagation of a flame through the vortex ring was also investigated and it was concluded that the stoichiometric region, the low intensity core region of Figure 7(a), of the inner ring of the overall vortex ring is where the flame passed through. The flame intensity structure is seen in Figure 7(b).

Convective velocity measurements of eddies of a Mach 1.5 jet have also been performed by (Murakami and Papamoschou 2000) using an acetone PLIF based flow visualization technique and a 2D cross correlation technique.

Aero-Optic Measurements with Acetone PLIF

As previously mentioned, acetone PLIF has also been used in aero-optics research by (Catrakis, Garcia and Natham 2006), (H. Catrakis 2006), and (H. Catrakis 2004). In their work, a wall jet was seeded with acetone vapor whereas the environment in which the jet was exhausted was not seeded. In this fashion, they were able to obtain high contrast images with signal proportional to the local number density of acetone molecules. As discussed, an implicit assumption in their work was that the local fluid density can be modeled as a simple mixing process between two streams of varying density. Thus, by tagging one stream with acetone, the degree of mixing at any given point can be determined from the PLIF signal and subsequently the density. A significant shortcoming to this approach, however, is that it inherently neglects the possibility of density changes *due to compressibility effects*. Figure 8 shows an example of the images acquired in this technique. As will be seen in the results of this work, we also observe structures with sharp interfaces between high and low density fluids (a feature of mixing), but we also observe circular regions of low density fluid associated with the core of vortices not observed in these visualizations. As the density drop in the core of a vortex is more readily associated with the pressure well formed at the core of the vortex, the technique employed by Catrakis should not be expected to reveal such features and is inherently flawed from a pure aero-optics point of view.

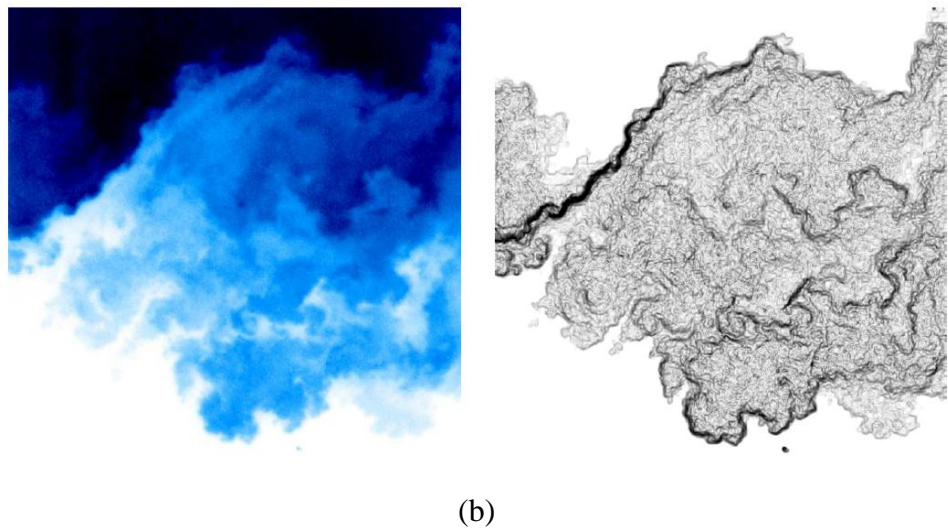


Figure 8: Image of Compressible Shear Layer (a) Index of Refraction Field (b) Interfacial Fluid Thickness Field [(Catrakis, Garcia and Natham 2006)]

E. Objectives of Present Work

While some of the finer points of the objectives of this work changed over the course of the project, the primary objective remained the same: *To develop acetone PLIF into a viable diagnostic for the measurement of density fluctuations in compressible flow fields.* The achievement of this objective is the main outcome of this proposal and expected to have the broadest impact on the greater fluid dynamics research community.

The context and motivation for such an effort is the field of aero-optics where knowledge of the fluctuating density field behind a turret at high subsonic Mach numbers is essential for understanding the aero-optically relevant flow features and the design of strategies to mitigate wavefront distortions. To this ends, another objective of the work was: *To apply acetone PLIF for the investigation of density fluctuations in the turbulent shear layer and wake formed by a hemisphere.* Related to this, a secondary objective was *to develop the computational tools necessary to calculate the distortion of an optical wavefront passing through such a flow field.* To facilitate completion of these objectives, a special transonic test section was designed and fabricated to be compatible with existing infrastructure at Auburn University and the acetone PLIF technique.

As implied by the title of the proposal, however, a broader objective was to develop acetone PLIF into a 3-D density measurement technique. The potential to adapt acetone PLIF for 3-D measurements is through the use of a unique MHz rate pulse burst laser system developed by the PI, along with a scanning mirror and high-speed camera whereby a high-speed sequence of 2-D acetone PLIF images is acquired from which a 3-D measurement of the density field can be made. As will be discussed in detail, this objective was not fully met mainly due to technical limitations associated with available high-speed cameras. Even so, the work conducted here still clearly shows that, *given the proper instrumentation, the 3-D density measurements based on acetone PLIF is a viable technique.*

Lastly, a new objective was developed over the course of this project: *To assess the feasibility of using background oriented Schlieren (BOS) imaging for the measurement of wavefront distortion.* BOS is a technique commonly used for the visualization of compressible flow fields and achieves its effect through the refraction of light by density gradients naturally present in the flow. BOS is also inherently quantitative due to the method in which the refraction is determined. As such, it occurred to the PI that such a technique could be used to measure the distortion of an optical wavefront passing through the flow field with the main advantages being that it would be significantly less expensive and could provide higher spatial resolution than competing wavefront sensors such as Shack-Hartmann wavefront sensors. In light of its potentially significant relevance to the aero-optics community, development of this concept was deemed within the scope of the present work. It should be noted that this development effort, while significant, was only a minor objective of this work and utilized only a small portion of the overall resources so that it did not interfere with the completion of the above objectives.

II. Development of Acetone PLIF for Density Measurements

A. Basic Concept

The fundamental concept of this work is to utilize the fluorescence of acetone vapor seeded into a flow field for the purposes of measuring the flow density. To first order, the fluorescent signal of acetone (or any fluorescent species for that matter) is directly proportional to the local number density of molecules. For a flow field that is uniformly seeded (i.e. constant mole fraction throughout the entire flow), the signal will thus be proportional to local flow density. Assuming the flow is uniformly seeded, the main challenges associated with the implementation of acetone PLIF is accounting for secondary effects, such as a weak (but non-negligible) influence of pressure and temperature on the signal and experimental considerations, such as calibrating for a non-uniform laser sheet intensity and pulse-to-pulse variations in laser power. This section describes these various issues and the steps taken to account for them.

B. Fluorescent Signal Equation

The acetone fluorescence signal, S_f , in collected photons, is quantified by the fluorescence signal equation:

$$S_f = \frac{E}{hc/\lambda} \eta_{opt} dV_c \left[\frac{\chi_{acetone} P}{kT} \right] \sigma(\lambda, T) \phi(\lambda, T, P, \sum \chi_i) \quad (7)$$

Most of the terms in this equation are constants for this work, including h (Planck's constant), c (speed of light), λ (wavelength of excitation), dV_c (collection volume), $\chi_{acetone}$ (acetone mole fraction), and k (Boltzmann's constant). The assumption of constant acetone mole fraction is crucial for the use of this technique for density measurements as it allows for Eq. 7 to be written as

$$S_f = CE \eta_{opt} \rho \sigma(T) \phi(T, P) = CE \eta_{opt} \rho \sigma(P, \rho) \phi(P, \rho) \quad (8)$$

Where C represents all of the constant terms in the equation. Thus, it can be seen that the fluorescent signal is directly proportional to density. The non-constant terms in Equations 7 and 8 are E (local laser fluence), η_{opt} (optical collection efficiency), P (local pressure – total of acetone and air partial pressures), T (local temperature), σ (absorption cross-section), and ϕ (fluorescence quantum yield). Optical collection efficiency is temporally, but not spatially constant because the solid collection angle, which is a component of the optical collection efficiency, varies throughout an image. Local laser fluence is also not constant throughout the flow field because the laser sheet spreads outwardly as it propagates through the imaging region, resulting in drops in laser sheet intensity along lines of constant propagation angle. Also, the laser sheet intensity is roughly Gaussian and thus the laser sheet energy distribution is most concentrated at its center.

The laser sheet non-uniformity, due to local laser fluence differences, causes differing 266 nm intensity values to reach the acetone molecules throughout the imaging region. This results in differing fluorescence signal values throughout the imaging region purely due to excitation energy differences and not necessarily due to density, temperature, or pressure differences. This is compounded by optical collection efficiency differences (COS^4 drops in intensity as distance

from the center of the image is increased, a type of vignetting) when this fluorescence signal is collected by a CCD.

Thus, the main challenge to solving Eq. 8 for density is to come up with a suitable method for estimating the local laser fluence and pressure for the region of interest. In this regards, we utilize an in-situ calibration method where the signal in the turbulent regions of the flow is normalized by the signal found in the free stream region of the flow, where the conditions are expected to be approximately constant. As such, we are able to measure, in an in-situ fashion, the distribution of laser fluence throughout the entire image. To account for pressure, we consider the range of pressure fluctuations expected in the flow and define an error bounds on our measurement accuracy based on variations in σ and ϕ over this range. Details to each of these steps are provided below.

C. Image Processing

In order to reduce the fluorescence signal at each point in an acetone PLIF image down to a density value, an image processing procedure must be performed which involves an in-situ calibration. This procedure is designed to correct for background noise, vignetting (COS^4 intensity drops), and laser sheet non-uniformity, as well as normalize the signal at each point in the image to freestream conditions (which are assumed to be known), as seen in Figure 9.

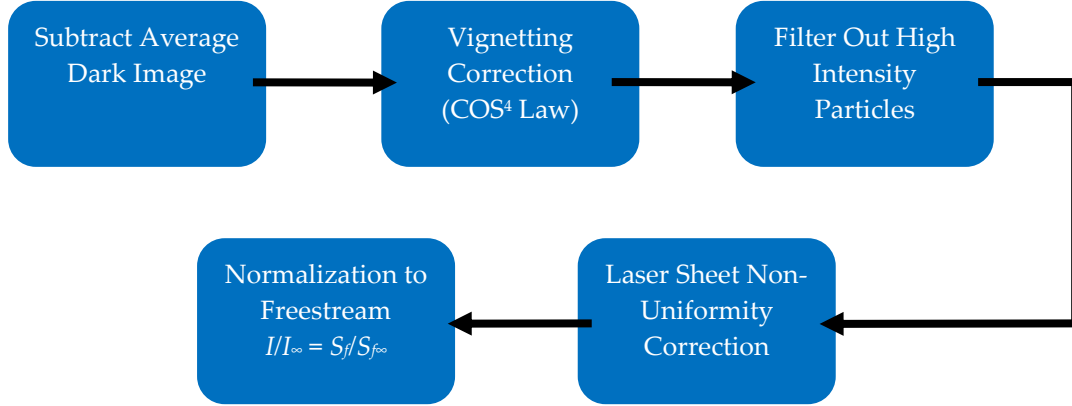


Figure 9: Flow Chart of Image Processing and In-Situ Calibration Procedure

Images in the form of $S_f/S_{f\infty}$ are the result of this procedure. When Equation 8 is normalized by a value representing freestream conditions, Equation 9 results and is a mathematical relationship for $S_f/S_{f\infty}$ that can be applied to images that are in the form $S_f/S_{f\infty}$.

$$\frac{S_f}{S_{f\infty}} = \frac{\rho\sigma(T)\phi(T, P)}{\rho_\infty\sigma(T_\infty)\phi(T_\infty, P_\infty)} = \frac{\rho\sigma(T)\phi(T, \rho RT)}{\rho_\infty\sigma(T_\infty)\phi(T_\infty, \rho_\infty RT_\infty)} = \frac{\rho\sigma\left(\frac{P}{\rho R}\right)\phi\left(\frac{P}{\rho R}, P\right)}{\rho_\infty\sigma\left(\frac{P_\infty}{\rho_\infty R}\right)\phi\left(\frac{P_\infty}{\rho_\infty R}, P_\infty\right)} \quad (9)$$

Dark Image Subtraction, Vignetting Correction, and Laser Sheet Non-Uniformity Correction

The image processing and in-situ calibration procedure begins with average dark image subtraction, vignetting correction for COS^4 intensity drops, and filtering of high intensity particles. An average dark image is subtracted from each acetone PLIF raw image to eliminate background noise in the signal, as seen in Figure 10. Next, a vignetting correction corrects for the fact that light intensity in an image decreases as the distance from the center of the image is increased. This decrease in light intensity follows the COS^4 law (Kingslake 1992), (Clemens 2002), (Aggarwal and Ahuja 2001) and based upon this law, correction coefficients are created for and applied to each point in an image as seen in Figure 11. Unfortunately, this method does not account for other attributes that can lead to vignetting, such as angular sensitivity of the CCD and imaging lens. An average flat field correction image is the best means of correcting for this type of vignetting, however, suitable flat field images were not obtained at the time of this report. Thus, the COS^4 Law method implemented here has room for improvement. *A more robust flat field correction will be used in all future work based on this technique.*

After the vignetting correction, high-intensity fluorescent particles (e.g. oil droplets), if any, are filtered out of the images. These particles are infrequent but when they pass through the flow field they fluoresce and/or scatter fluorescing light. This creates infrequent bright dots in some of the images, which affects the laser sheet non-uniformity correction explained in the next paragraph. A filtering procedure was used to eliminate these particles by setting the intensity value of these pixels in the image to the average intensity of a group of nearest neighboring pixels, as seen in Figure 12.

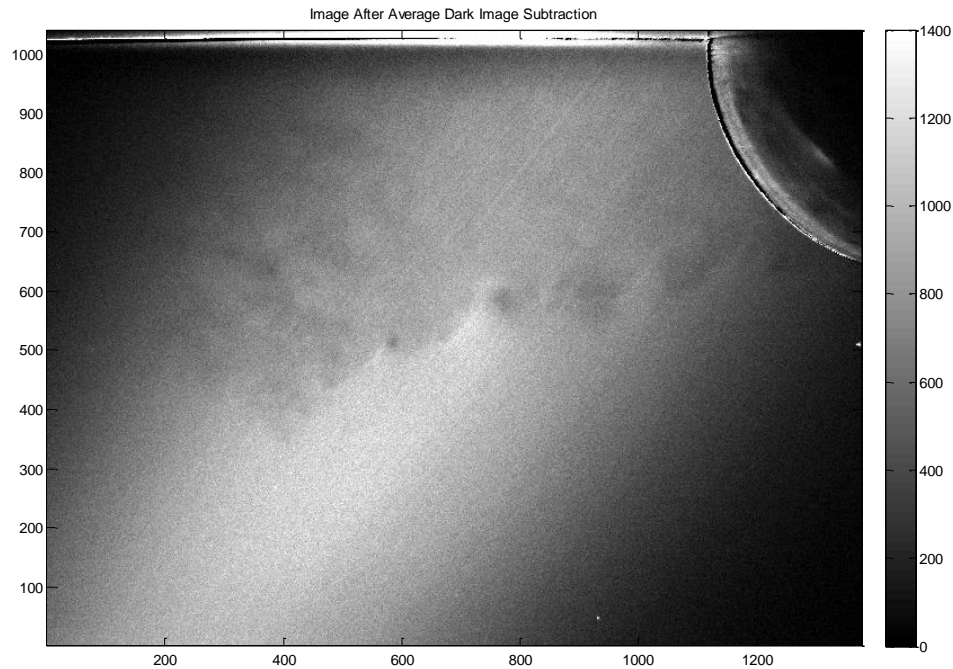


Figure 10: Image After Average Dark Image Subtraction

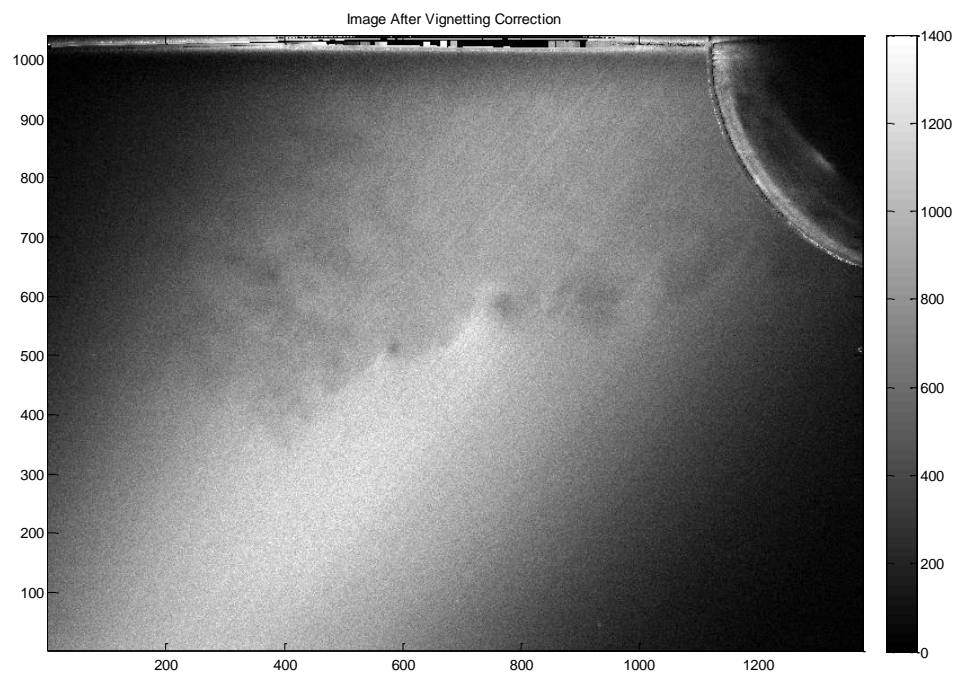


Figure 11: Image After Vignetting Correction

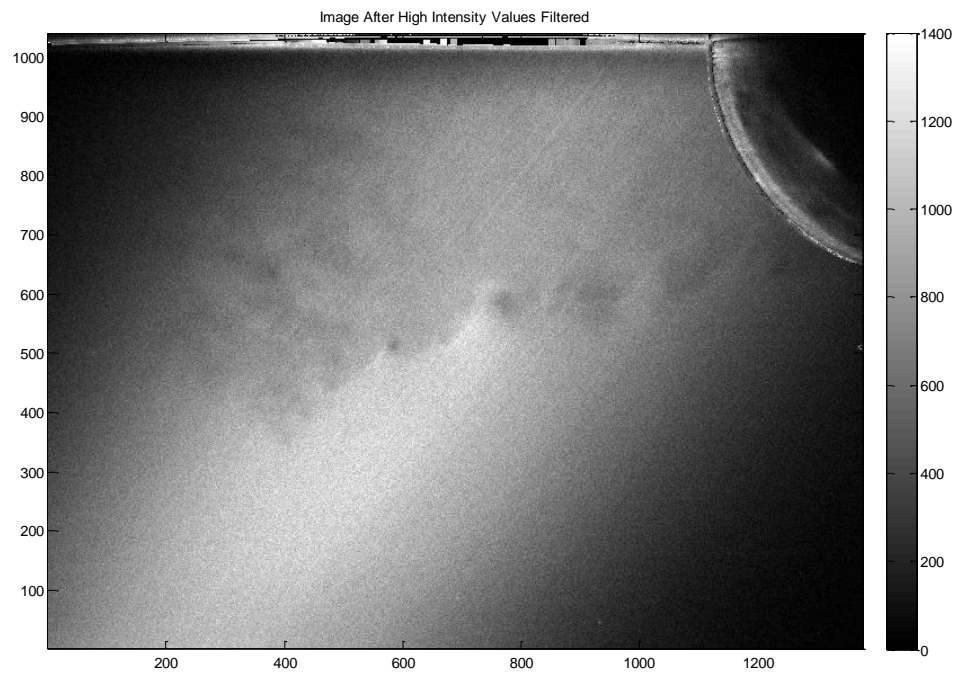


Figure 12: Image After Filtering Out Particles

The most important step in the entire process is the laser sheet non-uniformity. The laser sheet appears trapezoidal in the imaging region because it propagates and spreads from a virtual starting point outside of the imaging region. Therefore, a theoretical origin for the laser sheet exists, giving every point in each image (x_{ij} and y_{ij}) a radial propagation length (R_{ij}) and propagation angle (θ_{ij}) value relative to this origin. Equation 10 is used to calculate the radial propagation length and the propagation angle is calculated using Equation 11. Note x_o and y_o are the distances of the origin to the bottom left corner of the imaging region, as seen in Figure 13.

$$R_{ij} = \sqrt{(x_o + x_{ij})^2 + (y_o + y_{ij})^2} = \sqrt{X_{ij}^2 + Y_{ij}^2} \quad (10)$$

$$\theta_{ij} = \tan^{-1} \left(\frac{y_o + y_{ij}}{x_o + x_{ij}} \right) = \tan^{-1} \left(\frac{Y_{ij}}{X_{ij}} \right) \quad (11)$$

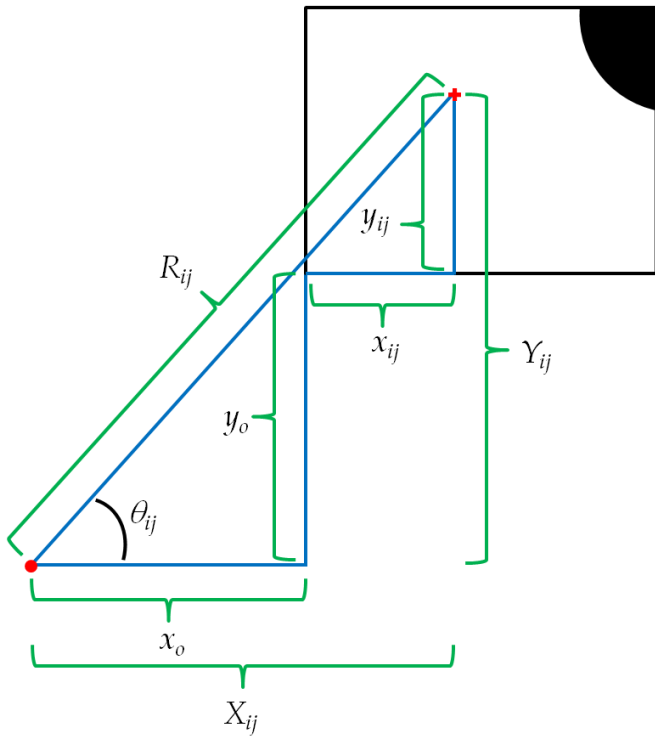


Figure 13: Propagation Angle and Radial Propagation Length

As the laser sheet propagates and spreads from the origin, it is assumed that along lines of constant propagation angle (relative to the origin) any drops in laser intensity ($I_{Laser,ij}$), which subsequently result in drops in fluorescence signal and thus fluorescence intensity ($I_{f,ij}$), are proportional to the radial propagation distance from the origin ($I_{Laser,ij} \propto \frac{1}{R_{ij}}$). Drops in laser

intensity due to absorption throughout the test section are negligible in this work because the acetone mole fraction is low ($\approx 3\%$). At each point in the image, the fluorescence intensity $I_{f,ij}$ is multiplied by the corresponding radial propagation distance R_{ij} . This makes the laser sheet intensity constant along lines of constant propagation angle, as seen in Figure 14.

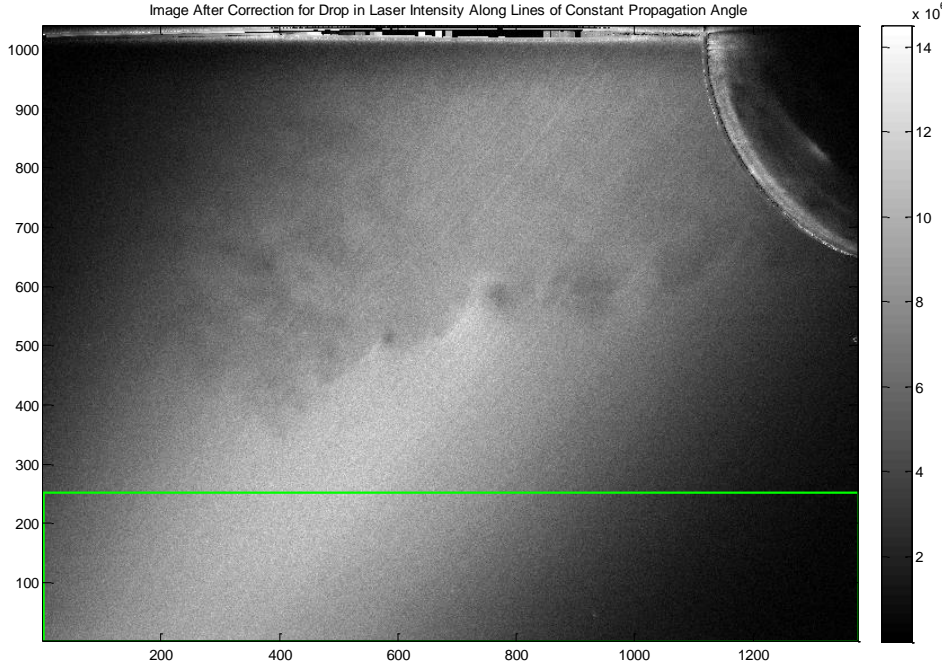


Figure 14: Correction for Drop in Laser Intensity Along Lines of Constant Propagation Angle

The fluorescence intensity values in the freestream region were used to create correction coefficients vs. propagation angle which could be used to make the laser sheet energy distribution constant as opposed to roughly Gaussian. As stated previously, conditions of ρ_∞ , T_∞ , and P_∞ are assumed to be approximately constant in the freestream and thus fluorescence signal should be constant as well in this region. Thus, any signal variations seen in the free stream are attributed to variations in the laser sheet intensity. After the previous steps in the in-situ calibration were completed, fluorescence intensity values in the freestream along arcs of constant radius R_{ij} (approximately pixels; mm) were 2-D interpolated for a constant set of propagation angles θ_{ij} (approximately 56° - 62°). The boundaries of these arcs and angles can be seen in Figure 14. All of the intensity values for each constant angle (for all the arcs) were averaged, resulting in a single set of average intensity values versus θ_{ij} . The maximum intensity value in this set was divided by the intensity values in this entire set. This resulted in a single group of correction coefficients versus θ_{ij} , which is plotted in Figure 15. Note that the correction coefficients were only found over the range of θ_{ij} values in the image where freestream intensity values could be clearly seen (i.e. the laser sheet width). Correction coefficients outside of this θ_{ij} range were set to zero.

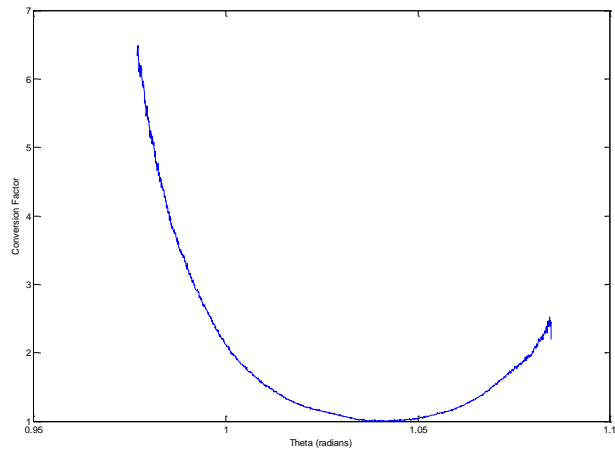


Figure 15: Plot of Correction Factor vs. Propagation Angle

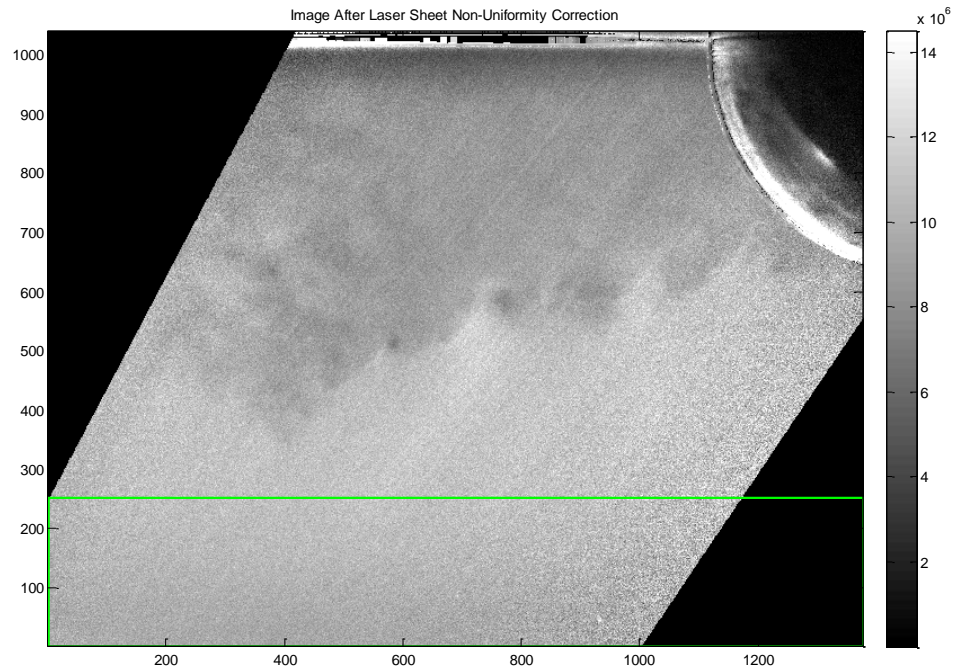


Figure 16: Image After Laser Sheet Non-Uniformity Correction

These correction coefficients were applied to all points in the image along lines of constant propagation angle. A correction coefficient could be interpolated for each pixel in the image, as θ_{ij} was known for each pixel, and be multiplied by the fluorescence intensity value of each corresponding pixel. Once this was complete, the local laser fluence was approximately constant throughout the entire image. The image after laser sheet non-uniformity correction is shown in

Figure 16

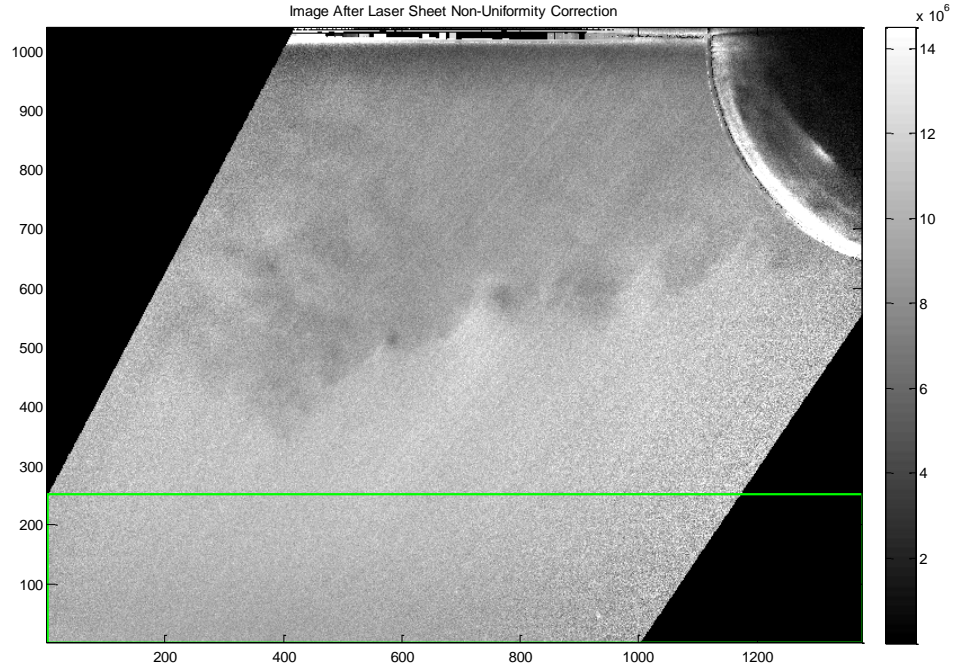


Figure 16.

Note that during this image processing and in-situ calibration process, the theoretical origin was moved iteratively to different locations until a “best” corrected image was found. The criteria for “best” was the image after the in-situ calibration did not have intense streaks in the image, more flow data/features are visible than in the raw image, and the intensity values in the freestream are approximately constant (with the exception of a few dark regions that could not be corrected). Slight darkness near the edges suggests that there is still room for improvement in this in-situ calibration. Once the laser sheet non-uniformity correction was completed, the intensity of every pixel in each image was divided by the average freestream intensity value to yield an image of $I_f/I_{f\infty} = S_f/S_{f\infty}$ values, as seen in Figure 17.

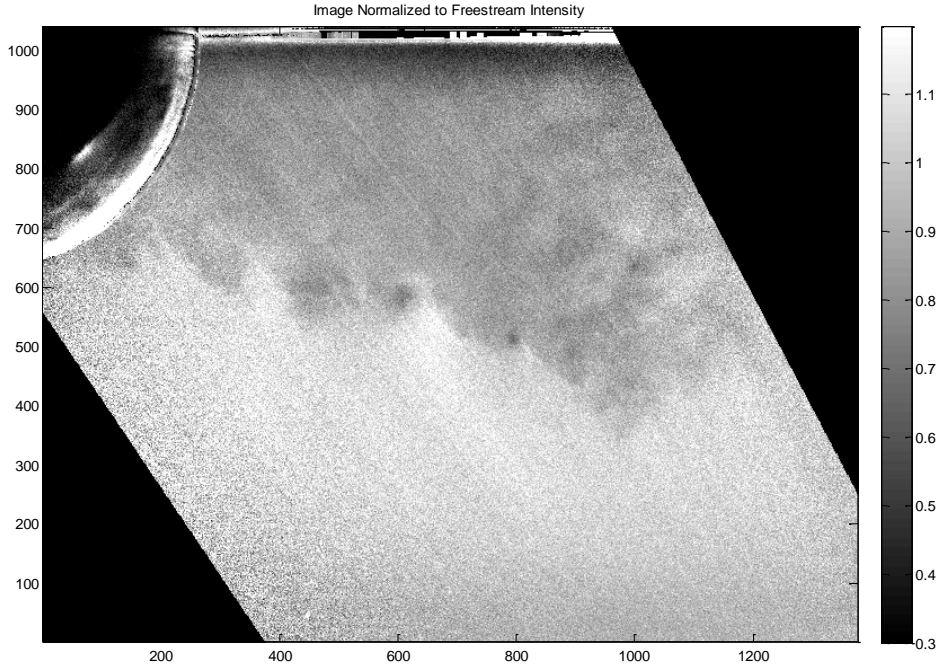


Figure 17: Image Normalized to Freestream Intensity $I_f/I_{f\infty} = S_f/S_{f\infty}$

D. Signal Dependence on Pressure and Temperature

The behavior of the absorption cross-section and fluorescence quantum yield with changes in density, temperature, and pressure must be understood before Eqn. 8 can be utilized to determine density from the image intensity data. As explained previously, (Thurber 1999) created a model for ϕ and also obtained σ vs. T data for acetone (in a nitrogen bath gas) at multiple wavelengths. Thurber provides a C++ source code that calculates the fluorescence quantum yield for acetone in a nitrogen bath gas when given an input temperature, pressure, and wavelength of excitation. This source code was modified here to be used in MATLAB and to be applicable with air as the bath gas, as opposed to having nitrogen as the bath gas and to allow input of an acetone mole fraction (should be small percentage as the air mole fraction should be close to 1).

For this work, the model was modified to also include oxygen and argon as dry air (the bath gas in this work) is made up primarily of nitrogen, oxygen, and argon. In addition, a k_{O_2} term was added to the original model to account for slight oxygen quenching of fluorescence. The acetone mole fraction was small, approximately 3%, so adding a term for collisions between acetone molecules did not significantly change the overall value of the k_{coll} term, although this term was added nonetheless. As explained earlier, the Lennard-Jones potential was used in certain areas in this model when the Stockmayer potential actually should have been implemented. Collisional effects from the polarity of acetone were not modeled exactly in the correct manner as a result, i.e. dipole interactions were not included. Also, the equations used to calculate the overall molecule collision diameter and collision potential energy for collisions between polar acetone molecules and non-polar molecules (nitrogen, oxygen, and argon) do not include the dipole moment. However, for low acetone mole fraction applications, these shortcomings in the model were assumed to not have a significant effect.

Thurber's absorption cross-section versus temperature data for 266 nm was added to the code so it could be interpolated/extrapolated at the specific input temperature and multiplied by the corresponding fluorescence quantum yield calculated from the input pressure and temperature. Thus, when the code executed, it produced values of

$$\sigma(T)\phi(T, P) = \sigma(T)\phi(T, \rho RT) = \sigma\left(\frac{P}{\rho R}\right)\phi\left(\frac{P}{\rho R}, P\right)$$

to be used in Equation 9. Note that the

absorption cross-section versus temperature data was only collected by Thurber down to a temperature of 296 K. For temperatures in this flowfield that were below 296 K, a linear extrapolation had to be used. This obviously induces some error in results, but with the proper lab equipment, one could obtain their own absorption cross-section versus temperature data and eliminate the error from this assumption. For more information on Thurber's fluorescence quantum yield model and absorption cross-section, see (Thurber 1999), (Hartwig 2010), (Tran 2008), (Braeuer, Beyrau and Leipertz 2006), and (Koch, et al. 2004).

Sensitivity of σ and ϕ over range of conditions considered here

Thurber verified the original fluorescence quantum yield model at 266 nm excitation for pressures and temperatures as low as 1 atm and 296 K. In this work, the minimum freestream conditions of pressure and temperature are approximately 1.503 atm and 257 K, respectively. Therefore, in this work, Thurber's modified model and absorption cross-section data have to be interpolated for higher temperature values and extrapolated for lower temperature values. Over the range of conditions expected in this work, Thurber's model predicts an increase in ϕ of approximately 15% and a decrease in σ of approximately 5%, so that they counteract each other to some extent. While additional data over this range of conditions may improve the overall accuracy of the technique, the relatively weak dependence of the signal on these parameters and the expectation that the data would produce the same trends as shown by the current model indicate that the improvement would be quite modest. Thus, further refinement of Thurber's model was not undertaken here.

E. Conversion to Density

In order to extract density information from the normalized signal $S_f/S_{f\infty}$ images, calibration curves of normalized signal $S_f/S_{f\infty}$ versus normalized density ρ/ρ_∞ were created for each image. Equation 9 shows that $S_f/S_{f\infty}$ is a function of ρ and either P or T , as ρ , P , and T are related through the ideal gas law. Uncertainty exists in this density measurement technique in the form of the local temperature or local pressure as these two parameters cannot be directly measured at every point in the flow field. Experimental bounds are thus placed on either of these two values for their maximum and minimum possible conditions in the flow field. Pressure values were constantly monitored in the test section during each test run (freestream static pressure and static pressure behind the hemisphere). Local pressure values in the flow field were assumed to fall within the bounds established by the freestream static pressure (maximum pressure) and the static pressure behind the hemisphere in the wake region (minimum pressure).

Curves of $S_f/S_{f\infty}$ vs. ρ/ρ_∞ were created for the two pressure bounds. Density was increased from zero to the stagnation density for each image. These density values, along with the pressure bounds were used to find the corresponding temperature values for each curve. Equation 9 was calculated with these input values (P , T , and ρ) and the freestream input values (P_∞ , T_∞ , and ρ_∞),

resulting in constant pressure curves of $S_f/S_{f\infty}$ vs. ρ/ρ_∞ . An average of the two curves was created and used to calculate the density data in each processed and normalized signal image. An example set of calibration curves for a single image is shown in Figure 18.

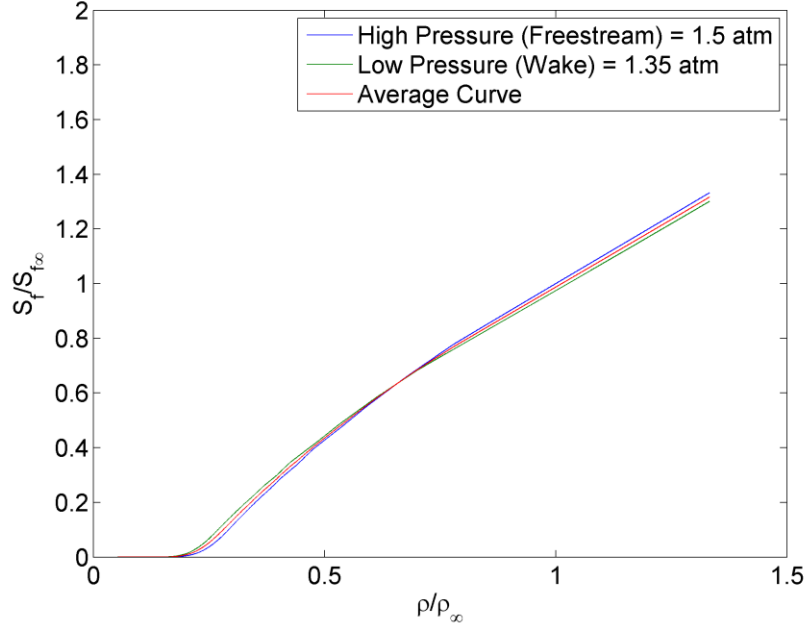


Figure 18: Curves of $S_f/S_{f\infty}$ vs. ρ/ρ_∞ for a Single Image

Figure 18 demonstrates that the uncertainty in density due to pressure is relatively modest with typical uncertainties being less than 2.5% of the free stream value. In addition, it is observed that the uncertainty actually decreases at lower densities. This is due to the relationship between pressure and temperature (equation of state) such that changes in absorption cross-section and fluorescent yield with pressure/temperature happen to cancel each other out over the range of conditions modeled here.

It is also observed that there appears to be a minimum density in which a measurement can be made. This is a consequence of enforcing a limited pressure range such that low densities lead to unrealistically high temperatures. Such conditions, however, were not observed in the current work.

F. Measurement Uncertainty

It is appropriate at this point to comment on the measurement uncertainty associated with the acetone PLIF technique. The uncertainty analysis presented here is based on data to be presented later in this report, but given here for relevance. There are generally two types of errors of interest in a measurement system: bias error and random error.

Bias error (or systematic error) is the error that would be expected in the measurement of the absolute value of density. The error can vary across the image, but would be constant in time. The largest source of bias error in the current experiments is due the calibration procedure described above where incorrect assumptions about the variation in local laser fluence and optical collection efficiency across the image can lead to a constant error. This error was

assessed by acquiring an image of the flow field without a hemisphere, thus creating a condition where a constant value of density should be expected across the entire image. Such an image is shown in Figure 19. It is clear from this image that improvements can clearly be made in the calibration procedure with a notable gradient observed at the outer edges of the images. This error source can be corrected for using a set of images such as those shown in Figure 19 and performing a flat-field correction. An insufficient number of images were acquired to perform such a step for the data presented here; however, all future work will include this step. We conservatively estimate bias errors to be on the order of 10 - 15% although it should also be noted that in the region of the interest (shear layer and wake), this error is considerably less. In addition, the nature of this error source has a low spatial frequency so that it is not expected to significantly affect our ability to visualize the high spatial frequency fluctuations associated with vortices and shock waves. In addition, as the bias error is steady, the magnitude of turbulent fluctuations (i.e. unsteady component) determined here are still expected to be valid.

The second type of error is random error, which characterizes the random fluctuations in signal from one shot to the next. This error consists of shot noise, dark noise, CCD read out noise and other sources of noise associated with the acquisition of an image. In the present case, it also includes uncertainty in pressure, which affects the fluorescent yield and absorption cross-section and leads to a ~2.5% uncertainty in density. The random error was estimated by observing variations in the signal ratio $S/S_{f\infty}$ in the free stream where signal levels are expected to be constant. It was found that the fluctuating values were on the order of 6-7%. This can also be partially observed in Figure 19 as the ‘graininess’ of the image. Combined with the 2.5% uncertainty associated with pressure, this leads to a total uncertainty of approximately 8%. A simple way to reduce this level of error is through low-pass filtering of the image. For example, using a 3 x 3 averaging filter reduces the uncertainty from 6-7% to ~2% such that the total error can be reduced to ~3-4%, albeit at reduced spatial resolution.

A few comments are appropriate for better understanding the influence of measurement uncertainty on the results reported in this work. First, the structures observed in this work are large enough to span across several tens of pixels, but small enough to be contained in region of relatively constant bias error. Thus, when one observes a decrease in local density, such as that associate with a vortex core, the extent of the region is large enough (spans 10s of pixels) so that the overall magnitude of the decrease is not dominated by the random measurement uncertainty, the value of which is more directly applicable to the signal at a single pixel. Thus, *we are confident that the images in the remainder of the report accurately represent the flow structures and associated drops in density of this flow field.*

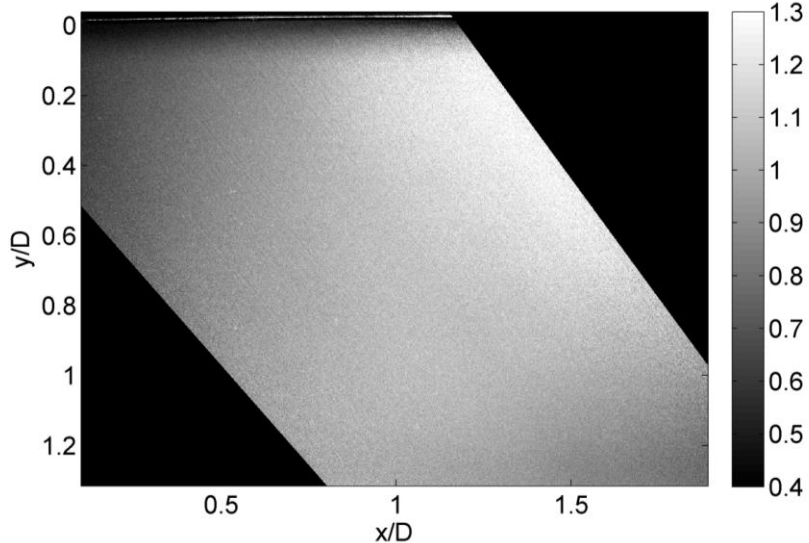


Figure 19: No Hemisphere Single-Shot Acetone PLIF Density Image (values normalized to freestream)

G. Limitations:

This section would not be complete without addressing the limitations associated with acetone PLIF. Overall, acetone PLIF has proved to be a viable technique for density measurements, particularly under the conditions of the present experiments. There are some limitations to the technique, however, that could affect its application and accuracy in other facilities or flow conditions.

1. Acetone Condensation

The signal collected for a given experiment depends directly on the amount of acetone seeded into the flow field. In the current work, the seeding is approximately 3% (mole fraction) and is primarily limited by the acetone vapor pressure, where too high of an acetone concentration will result in condensation. Understanding where this limit exists is very important because the fluorescence quantum yield model in this work is for acetone vapor and has not been validated for small liquid droplets of acetone. We do note, however, that indirect evidence seems to indicate that the fluorescent properties of small acetone droplets (such as those that initially form in the condensation process) is virtually indistinguishable from the vapor state. Thus, it is possible to withstand a finite amount of condensation and still make valid measurements; however, the exact limits of this have not been investigated. Thus, conservatively, one would desire to maintain flow conditions where condensation does not take place.

The properties that influence the vapor pressure of a liquid are encapsulated in:

$$\log p = A - \frac{B}{t + C} = 7.11714 - \frac{1210.595}{t + 229.664} \quad (12)$$

$$p = 10^{A - \frac{B}{t+C}} = 10^{7.11714 - \frac{1210.595}{t+229.664}} \quad (13)$$

Known as the Antoine equation (Dean 1999) these equations comprise of three coefficients, A, B, and C, that differ depending on the type of chemical. When this equation is simplified, as seen in Equation 13, it can be used to obtain the vapor pressure curve (vapor pressure, p , is in mm Hg and temperature, t , is in Celsius). For acetone, these coefficients have the following values: A=7.11714, B=1210.595, C=229.664. Figure 20 shows the vapor pressure of acetone plotted for a temperature range from 220 K to 300 K, which is approximately what is encountered in the current set of experiments. A curve for methanol is also included for reference as methanol is sometimes used for PIV seeding. Condensation will occur if the partial pressure of acetone in the flow exceeds the vapor pressure.

To illustrate the influence of acetone seeding on the current experiments, horizontal lines are drawn at various molar concentrations. It can be seen that for the low temperature conditions considered here, we are operating at close to this threshold. To further investigate this, tests were conducted to detect condensation by passing a 532 nm laser light sheet through the flow. In the presence of condensation, the light sheet would scatter significant amounts of light whereas in the absence of condensation, the light should pass through cleanly. It was observed that at the beginning of a test run, condensation was virtually undetected; however, halfway through a run, condensation occurred. This was later determined to be due to a gradual drop in total temperature as the storage tank was evacuated. Fortunately, the condensation was repeatable so that we could determine which images were influenced by condensation.

Interestingly, it is not possible to detect condensation in the PLIF images as images with and without condensation do not possess any noticeable distinctions. Thus, we are led to believe that the LIF behavior of small acetone particles is the same as acetone vapor. Nonetheless, the images presented here are restricted to those where condensation does not occur.

The major limitation condensation imposes on this technique is the reduction in signal that accompanies the reduced seeding levels required for operation at lower temperatures. For cold facilities, temperature is dictated by Mach number preventing application of the technique at large Mach numbers where the seed level must be kept small. This limitation can be partially overcome by using higher power lasers and/or more sensitive cameras. We note that acetone PLIF has been applied in a Mach 2.0 cold flow for flow visualization purposes providing a rough upper bounds on the technique's application. Alternatively, one might consider the use of acetone in a heated flow facility such that the static temperature can remain large at higher Mach numbers. Before doing so, one would need to consider the safety aspects associated with using acetone (which is flammable) in such an environment. We believe it is feasible, but would require a detailed and thorough safety analysis.

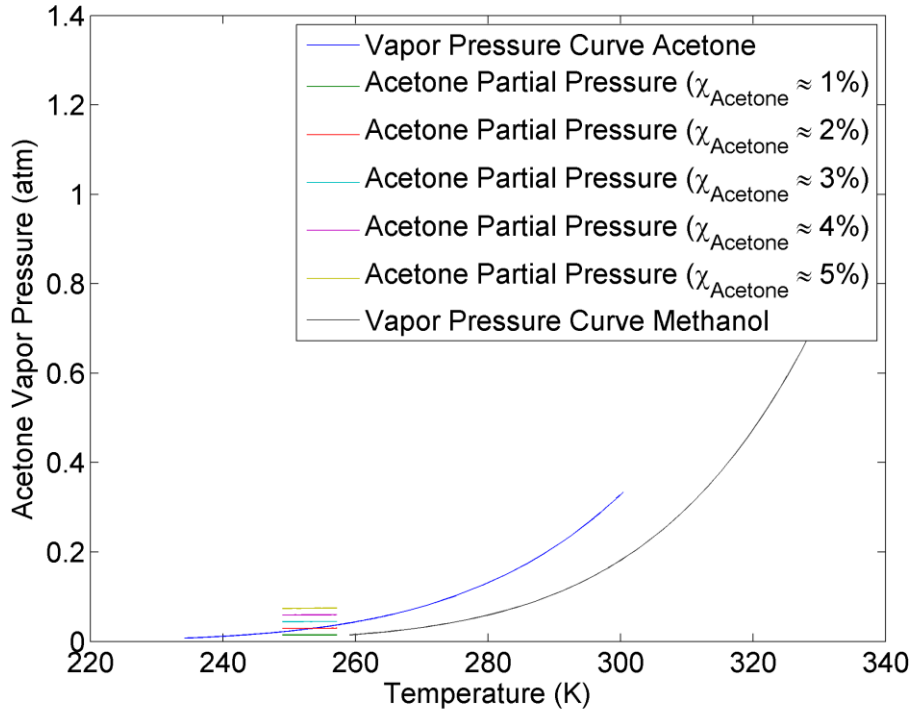


Figure 20: Plot of Acetone Vapor Pressure Curve (partial pressure curves created using freestream pressure and temperature values for valid data region)

2. Signal Strength

As alluded to in the previous paragraph, maintaining sufficient signal for a proper measurement is the key limitation to the application of acetone PLIF in other environments. The previous section discussed this limitation with respect to acetone mole fraction and condensation; however, one might also consider its dependence on the size of the imaging region. In this work, the laser energy was on the order of 20 – 30 mJ at 266 nm for a field of view of $\sim 1.5'' \times 1.5''$.

Increasing the field of view would require a proportional increase in laser energy or camera sensitivity. Commercially available pulsed Nd:YAG lasers are able to achieve pulse energies in excess of 200 mJ/pulse. In addition, back illuminated, cooled CCD cameras are available with sensitivity that is several factors better than the camera used here. This can be further enhanced through the use of pixel binning to reduce noise and increase the number of photons collected. As such, a well designed experiment with the appropriate instrumentation should be able to view an area up to 10 times larger than that viewed here under the same flow conditions.

3. Image Processing

As mentioned, the bias errors associated with the current implementation of acetone PLIF are relatively large. Improvements could easily be made through the introduction of an appropriate flat field correction. This could be conducted by keeping the experimental arrangement the same and simply removing the model from the flow field to produce a flat field image. Unfortunately, this was not implemented in this current work; however, the tools are now developed so that

implementation in the future will be easier. Random errors can be reduced by increasing the signal level as discussed in the previous paragraph.

4. Modeling of Acetone Photophysics

The last limitation mentioned here is that the current technique is limited by the accuracy of the fluorescent yield and absorption cross-section data, which was acquired under different conditions than experienced in the flow. This model could be improved by acquiring data under more relevant flow conditions using a well calibrated flow cell in which the bath gas, pressure, temperature and mole concentration of acetone can be modified. While not difficult or complex, the experiments would be time consuming and would require equipment not available in the PI's lab with the improvements in accuracy expected to only be modest.

H. Conclusions

The overall conclusions of our analysis and development of acetone PLIF is that it is a more than suitable and viable technique for measuring the 2-D density field in a compressible flow field. The technique is relatively easy to implement in a traditional blow-down style wind tunnel outfitted with UV grade windows for the introduction of a laser light sheet. The key points to the implementation of acetone PLIF for density measurements is a uniform mole fraction of acetone vapor seeded into the flow, a robust image processing scheme to account for variations in laser sheet intensity and optical sensitivity and a suitable model to account for a weak dependence on pressure in the signal. Under these constraints, we were able to make measurements with a bias error on the order of 10-15% and random uncertainty of 8%. We feel that the bias error can be reduced significantly through a more robust flat-field calibration. The random error can easily be reduced using pixel binning (or low-pass filtering) with a floor on the order of 2-3% due to uncertainty in pressure. The main limitations to application of this technique to other facilities is reduced signal level that accompanies a larger field of view or reduced seeding levels to avoid condensation at higher Mach numbers. Both limitations can be overcome using high power lasers and more sensitive cameras. It is estimated that given the right instrumentation, an order of magnitude increase in signal is possible. Thus, acetone PLIF appears to be a promising technique for density measurements in a wide variety of flow fields.

III. Transonic Test Section

As part of this work, a transonic wind tunnel was designed to produce a high subsonic free stream flow of Mach 0.78, which is close to the cruise condition of many military aircraft. A small hemisphere, meant to represent a turret, is mounted in the tunnel to visualize the fluctuations in density associated with the separated flow of the wake. In this section, the design of this transonic test is presented. This test section will be available for future Air Force projects as well.

A. Tunnel Design

The transonic wind tunnel was designed to take advantage of existing infrastructure already in place for a supersonic wind tunnel and shown in Figure 21. The supersonic tunnel consists of a high pressure compressor and air storage system, air supply line, pressure regulator, settling chamber, test section and diffuser. To utilize as much existing infrastructure as possible, the supersonic test section was mounted on a stand with casters so that it could be removed from the settling chamber as shown in Figure 22. For transonic operation, a new test section and diffuser were built that could be directly mounted to the settling chamber.



Figure 21: High-Pressure Air Supply Line and Settling Chamber



Figure 22: Supersonic Wind Tunnel Mobile Unit

In the design of the transonic test section, five main design constraints had to be met:

- The test section had to be large enough to contain a hemisphere model of reasonable size, while also minimizing blockage effects

- The test section had to have optical access on at least three sides
- The inlet nozzle had to be compatible/interchangeable with an existing settling/stagnation chamber (used for an already existing supersonic wind tunnel)
- The test section had to exhibit transonic conditions
- Everything had to be economical and relatively easy to build

Taking all of the above factors into account, the inlet, test section (4" x 4"), and diffuser for the transonic wind tunnel were designed and fabricated with a nominal freestream Mach number of 0.78. A schematic representation of the transonic wind tunnel is shown in Figure 23, along with two images of the wind tunnel seen in Figure 24. A key feature of the tunnel is the use of a downstream "choke block" to force the choke point in the tunnel to be downstream of the test section. In this fashion, the test section Mach number is dictated by the area ratio between test section and the downstream throat. This proved to be a critical design feature as the pressure regulator was not designed to maintain the pressure ratio necessary to maintain constant transonic conditions in the test section. Thus, the upstream pressure provided by the regulator could vary with time with the test Mach number remaining constant. This results in a slight change in Reynolds number (change of ~10%) over the course of the run as the test section pressure slowly decreases; however, this tradeoff was considered reasonable in light of the constant Mach number conditions that it allows.

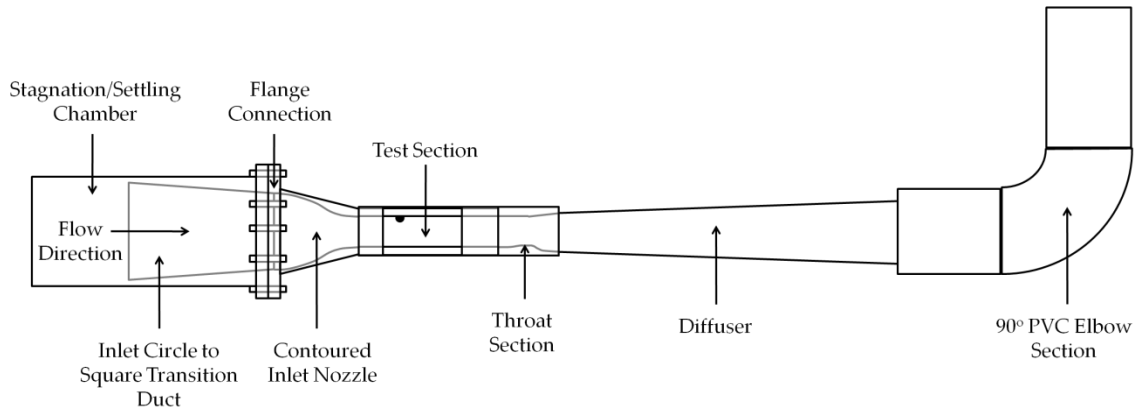


Figure 23: Schematic of Transonic Wind Tunnel (not drawn to scale)



Figure 24: Transonic Wind Tunnel

Design Details

A steel circular flange and an aluminum inlet section form the backbone of the transonic wind tunnel, as seen in Figure 25. A steel circle to square transition duct is welded to the upstream side of the steel circular flange. The contoured inlet section is bolted to the downstream side of this flange. This inlet section is specifically designed and contoured to ensure uniform flow upon entrance to the test section. This is achieved by making sure that the contour at the beginning and end of the inlet section has a first and second derivative equal to zero (Wall 2009), (Bell and Mehta 1988), (Brassard 2003). The 4" x 4" test section is attached to and located just downstream of the contoured inlet section, as seen in Figure 25.

The test section, constructed almost entirely of aluminum, has optical access on three sides (the bottom and both sides), as seen in Figure 26. The rectangular side windows are 5" x 6" x 0.5" (with actual viewing area of 4" x 6"). The outside edges (non-wetted edges) of these windows are slightly beveled/chamfered to reduce the probability of chipping. The bottom stepped window is 1" thick and is mounted into the bottom wall of the test section. As seen in Figure 27, the bottom 0.5" of the overall 1" thickness has an area of 3.5" x 12" and the top 0.5" of the overall 1" thickness has an area of 3" x 11" (with an actual viewing area of 3" x 11").

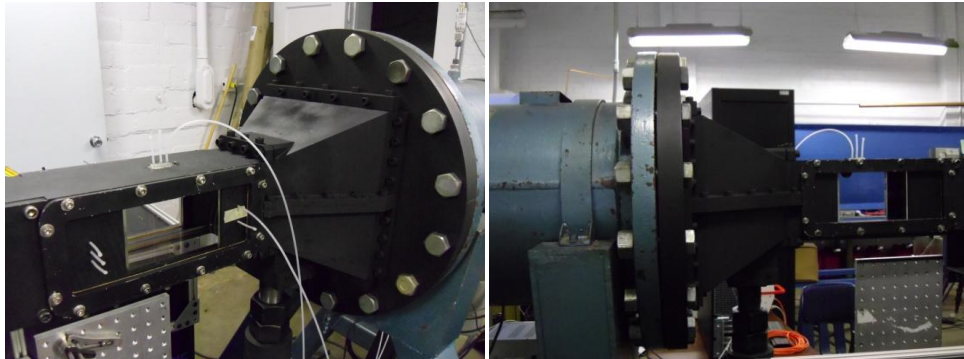


Figure 25: Settling Chamber, Flange, Inlet Nozzle, and Test Section

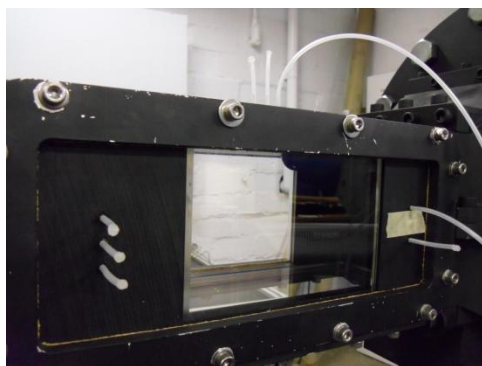


Figure 26: Test Section Optical Access

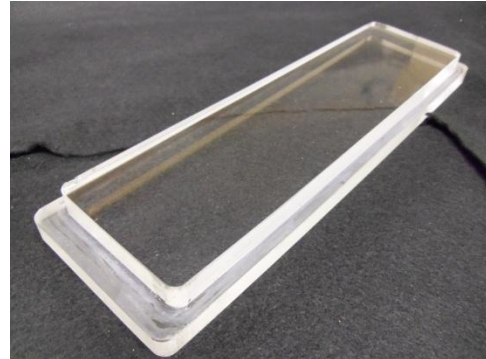


Figure 27: Bottom Stepped Window

All windows are constructed of UV fused silica, but the bottom window also has an AR coating specifically peaked for 266 nm and 532 nm. UV fused silica (from ESCO Products) was selected because it has an optimum transmission range of 180 nm - 2000 nm. The side windows were originally constructed out of BK7; however, it was later found that this choice resulted in the side windows fluorescing during acetone PLIF experiments, creating a large amount of noise which would have greatly affected images if left unchanged. Thus, UV fused silica was selected instead for the side windows and found to perform well.

The side windows and small, black, rectangular delrin insert plates make up the side walls of the wind tunnel test section. The delrin plates upstream of the side windows are 2.5" x 5" x 0.5" and the delrin plates downstream of the side windows are 3.5" x 5" x 0.5". On the left and right side of the test section, a side window is placed in between the upstream and downstream delrin insert plates. Using delrin insert plates gives flexibility to the design because these inserts can be machined to any width, enabling the windows themselves to be placed at any location in the test section. This is valuable if it is desired to gather data at locations far upstream or downstream of the model in the test section. The current delrin insert and optical window configuration (and only configuration used in this work) allows for viewing of 1.5D upstream of the hemisphere and 4.5D downstream of the hemisphere.

One set of the delrin plates are outfitted with static pressure ports for pressure measurements. All windows and delrin inserts are held in place by hollow, aluminum, rectangular brackets that are bolted to the test section, as seen in Figure 28. The brackets provide pressure to the outer edges of each window and delrin insert to hold them in place. These brackets are lined with thin cork sheet for cushioning purposes to protect the glass windows. The test section is also outfitted with o-ring chord in several locations to cushion the windows and also decrease leaks. The entire wind tunnel was painted flat black, including the inside walls of the test section. The inside walls of the test section, as well as the inside walls of the contoured inlet nozzle and choke block section, were also wet sanded to increase smoothness.

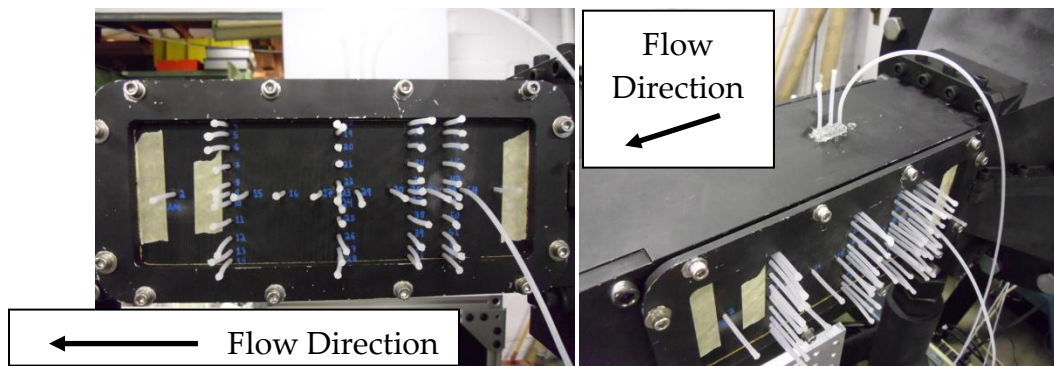


Figure 28: Location of Pressure Ports for Pressure Experiments

B. Hemisphere Model

A 1 inch diameter hemisphere model constructed of aluminum was used in this work. The frontal area of the hemisphere provides a total blockage of approximately 2.5%, which is less than that provided by the choke block ensuring that the model wouldn't choke the entire test section flow. It was fabricated from an aluminum cylinder by using a lathe and a series of filing, sanding, and polishing. It was mounted to the ceiling of the test section, 4 inches downstream

from the beginning of the test section, using a bolt that passed through the top wall of the test section and screwed into the hemisphere. The hemisphere was first painted flat black, but there were still reflection problems when using 532 nm light and slight fluorescence problems when using 266 nm light. It was coated, along with the top wall of the test section, with rhodamine 590/polyurethane during initial PIV experiments, but this was removed for later acetone PLIF experiments.

C. Facility Characterization

Several measurement techniques were used to characterize the flow in the transonic wind tunnel test section with the hemisphere mounted. This included pressure measurements, Schlieren imaging, shadowgraph imaging and PIV.

Pressure Measurements With and Without Hemisphere Mounted

Static pressure, stagnation pressure, and storage pressure values were measured for the transonic wind tunnel with and without the hemisphere mounted. A 12" x 5" delrin insert plate was outfitted with static pressure ports at multiple locations, as seen in Figure 28, and was mounted in the test section in place of one of the side windows and smaller upstream and downstream delrin insert plates. Pressure ports were located along the centerline of this large delrin plate, from the upstream end to the downstream end. This enabled the freestream static pressure values (and thus Mach number values as Mach number is found from the ratio of stagnation pressure to freestream static pressure $P_{0,t}/P_{\infty,t}$) versus downstream location to be obtained.

Several test runs were performed with and without the hemisphere mounted to find the pressure values at the static pressure port locations. Pressure measurements were also taken with no flow to make sure the transducers were correctly making measurements. Pressure measurements were obtained at approximately 10 Hz using Omega PX209 pressure transducers. The stagnation pressure was measured in the settling chamber and the storage pressure was measured in the high-pressure air supply line.

Pressure measurements without the hemisphere mounted revealed many important characteristics for this wind tunnel. Without the hemisphere mounted, it was apparent that the Mach number was constant throughout a test run and the freestream static pressure only changed slightly during a test run. It was also found that the Mach number increased by 0.02 along the length of the test section, presumably due to the growth of the boundary layer on the tunnel walls.

The pressure measurements with the hemisphere mounted also revealed interesting characteristics for this flow field. It was clear that the Mach number was constant throughout the test run and the freestream static pressure slightly changed during the test run. The freestream static pressure decreased (and Mach number increased) as the distance downstream in the test section increased. At the location of the hemisphere, and at the next port, the Mach number jumped to a maximum value (increased more than just a gradual increase) and the static pressure dropped (dropped more than just a gradual decrease). This is consistent with a local acceleration of the flow over the hemisphere.

Pressure measurements were also made for the pressure ports on the wall behind/downstream of the hemisphere. These pressure measurements were vital in quantifying the approximate pressure in the wake region. The pressure ports downstream of the back of the hemisphere revealed that

the port closest to the hemisphere experienced the greatest pressure drop. The second port experienced the second greatest pressure drop and the third port actually experienced a slight pressure increase from the freestream pressure value at this downstream location. The pressure drops are thought to be due to the fact that the pressure port is located in the recirculation region of the wake.

Overall, the pressure measurements showed that the flow conditions remained approximately constant over the course of a run and that the tunnel performed as expected. Pressure measurements were also acquired over the course of PIV and PLIF experiments to ensure consistent operation from one run to the next. More details can be found in the thesis of Reid (2007).

Schlieren and Shadowgraph Imaging

Schlieren images and shadowgraph images were obtained for the flow field with the hemisphere mounted. These images were qualitative in nature and revealed a horseshoe/necklace vortex, a separated shear layer, and a turbulent wake, as seen in Figure 29, which displays a few of the Schlieren images. Shocks and lambda shocks (Houghton and Carpenter 1993) formed on the hemisphere were also present in the images and were located at approximately 90° or slightly upstream, although the exact location is seen to fluctuate from one image to the next. These shocks dissipated with increasing distance from the hemisphere and form Mach waves by the time it reached to the other side of the tunnel such that shock reflections do not appear to interfere with the development of the wake.

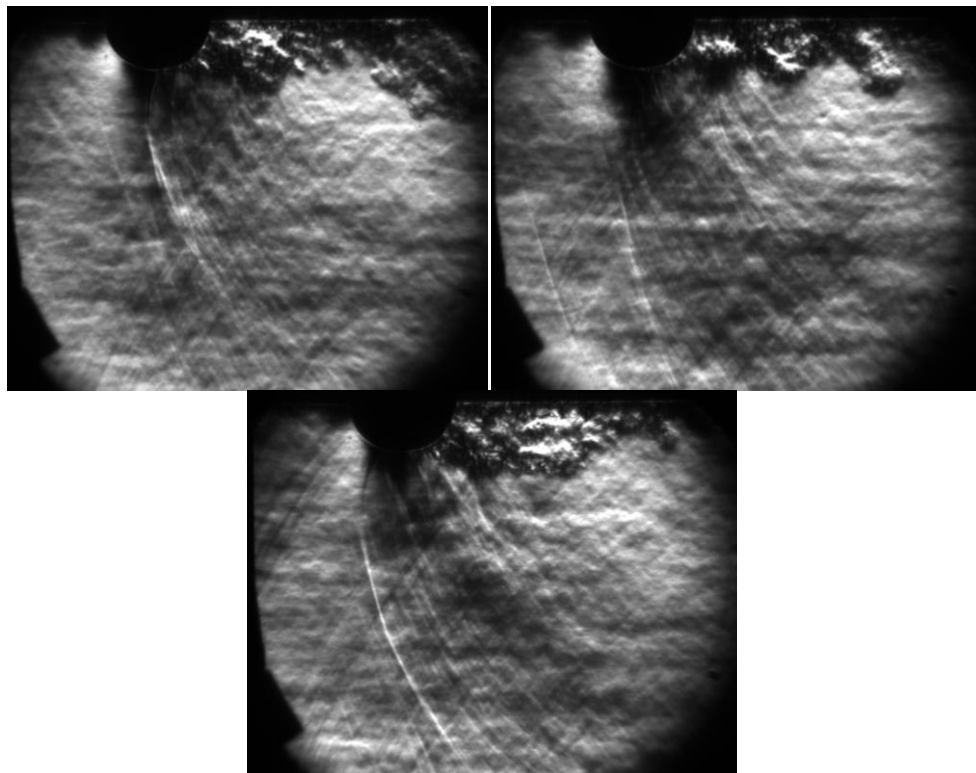


Figure 29: Schlieren Images of Hemisphere–Knife Edge Horizontal

Particle Image Velocimetry (PIV)

PIV was performed to provide quantitative information about the flow field so that assumptions about constant free stream conditions and other flow features could be validated. Seeding was achieved by mixing alumina particles into the acetone prior to seeding. This alumina particle/liquid acetone mixture was injected into the high-pressure air supply line. As the acetone evaporated, it left behind a uniform distribution of 0.3 micron alumina particles for PIV images. Overall, there was significant difficulty in obtaining a reasonable particle density for laser light scattering. This was mainly due to the settling of alumina particles in the liquid acetone before being injected into the flow. For these reasons, a large PIV data set was not able to be obtained for the current experimental facility. However, possible upgrades and improvements to the PIV experiments, are given in Reid (2011) should help in acquiring quality PIV data. These include using a cyclone seeder (with injection in the same location far upstream or in the settling chamber) or a Laskin nozzle (with injection in the same location far upstream) for seeding purposes.

A New Wave Solo III PIV Laser (Nd:YAG), capable of 50 mJ/pulse, was used for laser illumination. The 532 nm laser beam exited the PIV laser head and reflected off of multiple 532 nm mirrors and passed through an $f=-100$ mm spherical lens and then through an $f=150$ mm spherical lens. This beam then reflected off of two more 532 nm mirrors and then passed through an $f=-30$ mm plano-concave cylindrical lens to create a thin 532 nm laser sheet. Width of the laser sheet increased as the sheet propagated away from the cylindrical lens. This laser sheet passed through the bottom window of the wind tunnel test section in a normal orientation and illuminated the centerline plane in the flow field.

Laser sheet scattering off of the alumina particles was captured using a Cooke Corporation Sensicam QE high-resolution (1376 px x 1040 px), unintensified camera. PIVPROC software (on loan from Dr. Mark Wernet, NASA Glenn) was used to calculate pixel displacement for these images. Cross-correlation was applied for the images using a 64 px x 64 px window size on the first pass with a 50% overlap and a 32 px x 32 px window size on each subsequent pass with a 50% overlap. The field of view was 92.95 mm x 49.72 mm and the interpulse timing used was 2 μ s.

PIV experiments, although single-shot and small in number, revealed interesting and useful information about the flow field. With the hemisphere mounted, the freestream velocity was found to be approximately 250 m/s, which is in good agreement with the freestream velocity calculated from pressure measurements. It is also apparent from the plot of velocity magnitude, that the velocity magnitude greatly decreased in the wake region and was a maximum in the separated shear layer region (approximately 290 m/s). There was a stagnation point on the front and the back of the hemisphere where the velocity magnitude dropped to approximately zero. The plot of instantaneous vorticity revealed regions of large vorticity, particularly in the upper wake and separated shear layer region. In general, regions of large vorticity are also regions of pressure drops which also mean density drops. On the upstream half of the hemisphere, before separation, no large vorticity values were present. It can also be seen that the free stream velocity is approximately constant about 1 diameter distance away from the hemisphere providing further credence to the use of this region for in-situ calibration of PLIF images.

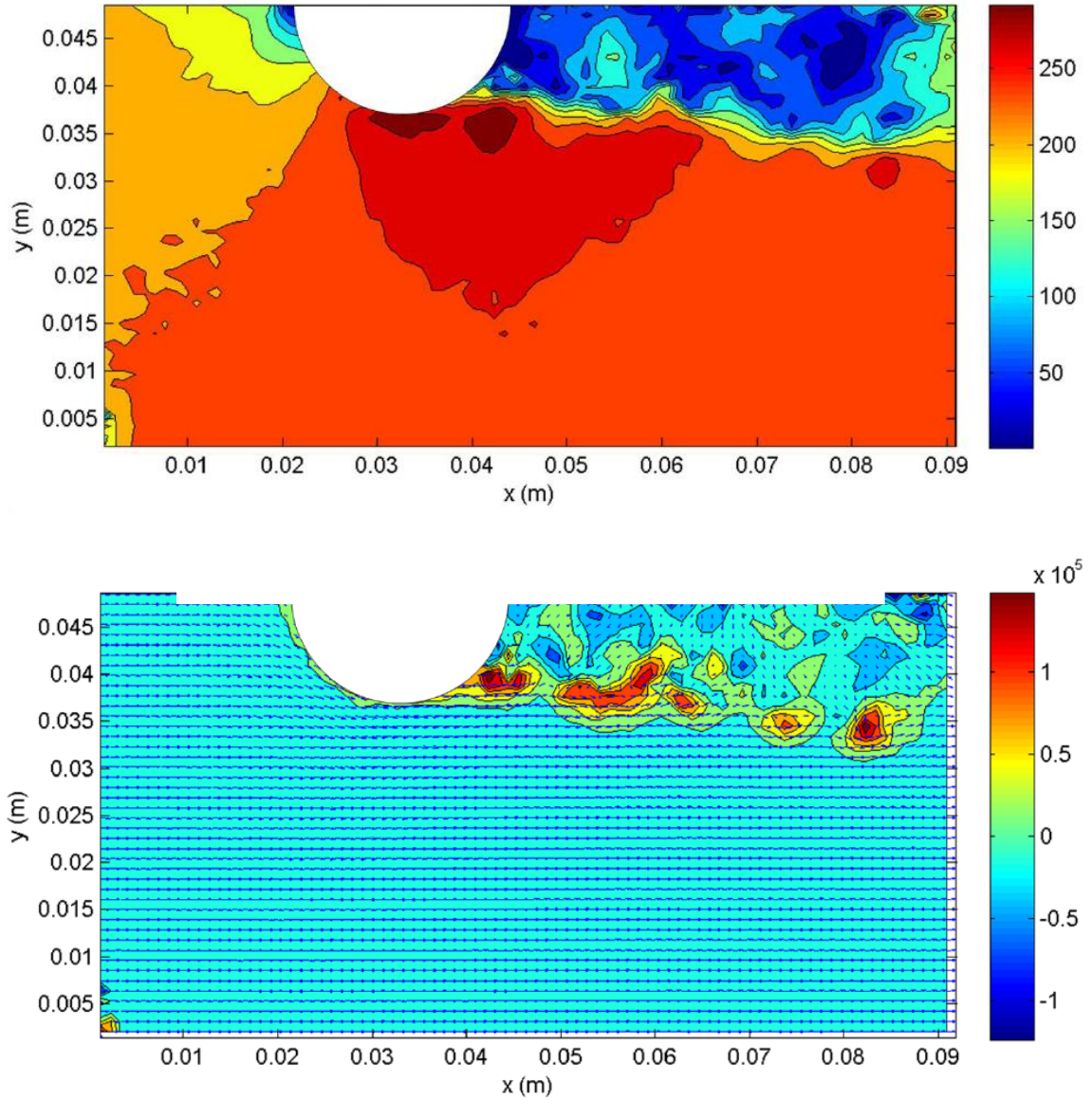


Figure 30: Instantaneous velocity field (m/s) and vorticity field (rad/s)

D. Acetone Seeder Design

The wind tunnel facility had to be outfitted with a means of seeding the flow field with acetone molecules for acetone PLIF and acetone molecules/alumina particles for PIV. The approach used was injecting acetone liquid far upstream of the test section and allowing the liquid acetone to disperse, mix with pressurized dry air, and evaporate by the time it reached the test section. The process for acetone seeding in this work was as follows. A small pressure vessel was filled with liquid acetone and pressurized using a nitrogen tank. An EPDM hose, attached to an exit pipe, was submerged in the liquid acetone, as seen in Figure 31. This exit pipe was attached to a Jefferson 1335 series solenoid valve which was attached to the outside of the pressure vessel. When the solenoid valve was triggered to open, the liquid acetone was pushed upward through the EPDM hose, out of the pressure vessel, and ultimately through a wall fitting. This wall fitting was connected through the wall of the cylindrical high-pressure air supply line pipe (the same air

supply line that received pressurized air from the storage tanks when the wind tunnel was operational and led to the stagnation/settling chamber) and extended to the center of this cylindrical pipe. A spray nozzle was attached to the end of the wall fitting and was oriented to spray in the upstream direction to help break up the liquid acetone and make sure it dispersed quickly and mixed with dry air, so it could evaporate before entering the test section. This ensured that the acetone was in molecular form and not particle form, so only dry air and acetone vapor were in the test section when acetone PLIF images were obtained (for PIV experiments, alumina particles were also present).

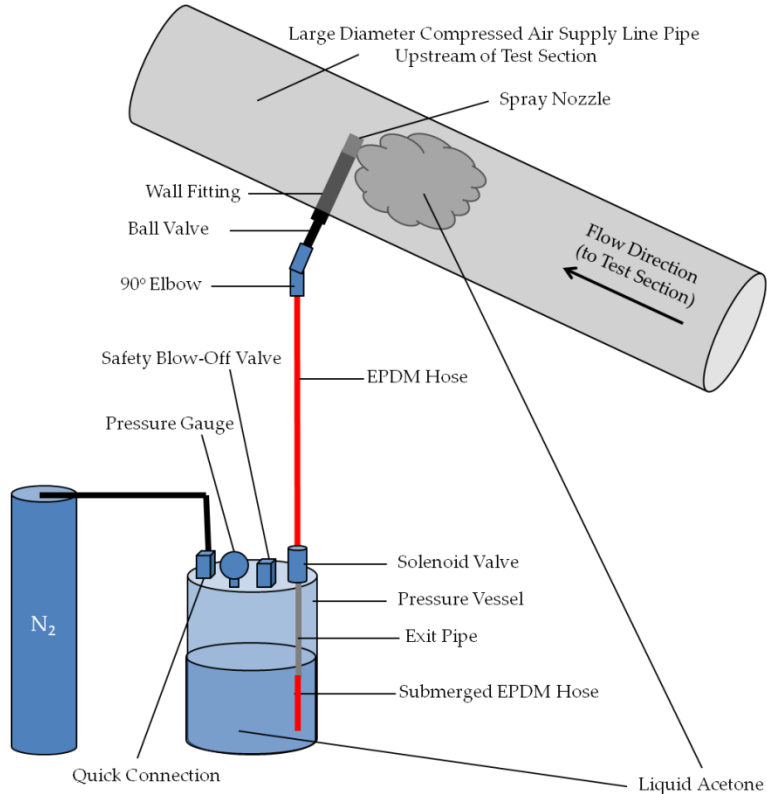


Figure 31: Schematic of Acetone Seeder

Acetone Mole Fraction

The amount of acetone injected into the flow was controlled by the pressure difference, Δp , between the small pressure vessel containing the liquid acetone and the storage pressure in high-pressure air supply line pipe. At the beginning of each acetone PLIF test run, the high-pressure air supply line started at a storage pressure of approximately 120 psig and decreased throughout the test run to 70 psig. As the storage pressure decreased during each test run, so did the storage temperature, stagnation pressure in the settling chamber, and the static pressure in the wind tunnel test section. However, as explained previously, a feedback control valve in the settling chamber kept the ratio of stagnation pressure to static pressure constant during the test run to keep the freestream Mach number constant. The nitrogen tank delivered a constant pressure to

the small pressure vessel via a regulator. Therefore, Δp increased throughout the test run and in turn so did the flow rate of acetone into the dry air stream.

Several spray nozzles were attempted to find a spray nozzle that gave a high enough flow rate at the specific Δp , while also breaking up the flow to enable evaporation of the acetone before entering the test section. The spray nozzle that was chosen was a Bete IS8, $\frac{1}{4}$ " spray nozzle constructed of stainless steel with a rectangular spray pattern. This spray nozzle internally bends the flow, similar to a 90° elbow, and the flow sprays out of the side of the nozzle.

The average acetone mole fraction was estimated to be approximately 3% by measuring the amount of acetone contained in the seeder before and after a run. As the pressure changes over the course of a run, the actual flow rate is expected to increase over time; however, this was not accounted for and only the average value is reported. This could be measured with a more accurate flow meter; however, one was not available for this work.

IV. 2-D Density Measurements of the Turbulent Wake Behind a Hemisphere

A. Experimental Arrangement

Single-shot, high-resolution acetone PLIF images were obtained across multiple planes of the flowfield. A large set of images (approximately 130 images over five wind tunnel runs, although some of these images were discarded due to image processing difficulties) were obtained for the plane that was coincident with the centerline of the hemisphere and smaller sets of images (approximately 26 images per set) were obtained for planes that were off-centerline (equally spaced 1/8 inches apart starting at the centerline and ending at 5/8 inches from the centerline, just past the hemisphere outer edge). The flow field was assumed to be symmetric about the hemisphere's x-axis (x-axis being the flow direction, passing through the centerpoint of the hemisphere, and increasing in value as the distance downstream increases). Therefore, images were only obtained for parallel planes on one side of the hemisphere. In addition, a set of approximately 26 acetone PLIF images, with a slightly smaller FOV, was acquired along the centerline and focused on the separation point and separated shear layer region in effort to better characterize this area of the flowfield. Note that the parallel plane images and the large centerline data set (as well as the separation region images) were obtained on different days.

The optical arrangement for these experiments is shown schematically in Figure 32. A 266 nm laser sheet was passed through the bottom window of the test section and was oriented at an angle of approximately 45-50° with respect to the horizontal, so that it passed through the shear layer/wake region and the centerpoint of the hemisphere (close to the centerline, but slightly yawed off axis). For separation point acetone PLIF images, the laser sheet angle was slightly adjusted so the most intense portion of the laser sheet was near the separation point on the hemisphere.

A New Wave Solo 200XT PIV Laser (Nd:YAG) was used to form a 266 nm laser light sheet. The SOLO 200XT is a dual-head design that creates a 532 nm beam output using frequency doubling crystals. This 532 nm beam output was converted to 266 nm by using a half waveplate and KDP frequency doubling crystal (efficiency approximately 20%). The second pulse was set to fire slightly after the first pulse as it was found that more energy output at 266 nm was achieved with this method, as opposed to both lasers firing simultaneously. The Solo 200XT has a reported initial 532 nm energy of 200 mJ/pulse and a beam diameter of approximately 5.5 mm; however, the measured output 532 nm energy was much less than this reported value. The Solo 200XT, with both lasers firing in the high setting (with a slight delay between them) yielded ~38 mJ/pulse at 266 nm before passing through final optics.

After the 532 nm light was converted to 266 nm light, several additional optics were used to drop out residual 532 nm light, steer the beam, focus/expand the beam, and form a thin laser sheet. The 266 nm beam first reflected off of three 266 nm mirrors and in the process dropped out the majority of the residual 532 nm light. Of the first three 266 nm mirrors in this optical setup, the first 266 nm mirror was mounted to the laser table and the other two 266 nm mirrors were mounted on a large breadboard located beneath the wind tunnel.

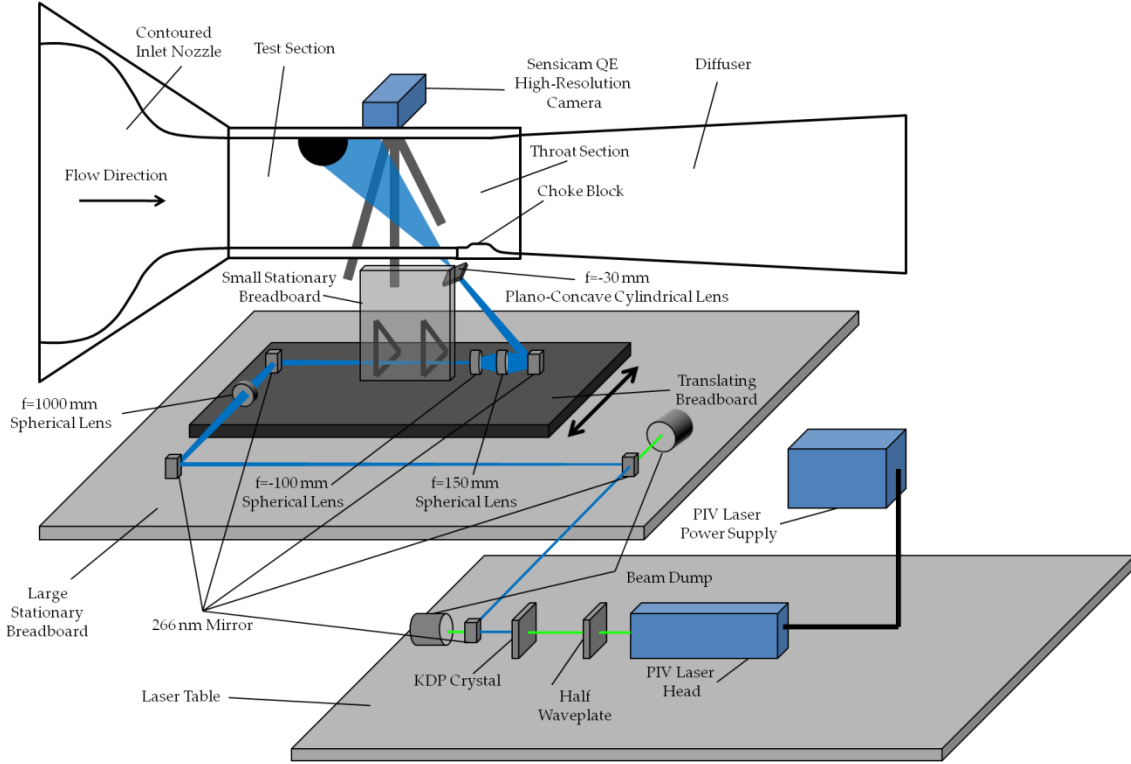


Figure 32: Schematic of Acetone PLIF Experimental Setup

The 266 nm beam then passed through an $f=1000$ mm spherical lens, reflected off of another 266 nm mirror, and then passed through an $f=-100$ mm spherical lens and an $f=150$ mm spherical lens (all four optics were mounted to a small breadboard that could be translated perpendicularly to the freestream flow direction). To counteract the divergence of the laser output beam, an $f=1000$ mm spherical lens was used. The separation distance between the $f=-100$ mm and $f=+150$ mm lenses regulated the thickness of the laser sheet in the imaging region in the test section. An $f=-30$ mm plano-concave cylindrical lens formed the focusing beam into a thin laser sheet by spreading the beam in a single direction. The laser sheet passed through the bottom window of the test section in an angled orientation, so a larger portion of the shear layer could be excited by the most intense portion of the laser sheet whose intensity profile was roughly Gaussian. This increased signal levels over a large portion of the shear layer, yielding higher quality images. In early acetone PLIF experiments, the laser sheet was passed through the bottom window of the test section in a normal orientation. However, it was concluded that this did not position enough of the most intense portion of the laser sheet on the most relevant flow features. In the imaging region the width and thickness of the laser sheet were approximately 25mm and 1mm, respectively.

In between test runs, the laser was fired at a continuous repetition rate, even when the camera was not acquiring images because the 266 nm energy output increased and leveled-off when the KDP crystal was heated by laser pulses passing through it as a thermal equilibrium state was reached. The half waveplate and KDP crystal were periodically adjusted to obtain maximum 266 nm energy output. Laser energy of approximately 38 mJ/pulse at 266 nm was achieved

(measured after the $f=1000$ mm spherical lens). Accounting for optical losses through the system, it is estimated that approximately 31 mJ/pulse of 266 nm light was present in the test section.

Acetone PLIF images were captured with a Cooke Corporation Sensicam QE high-resolution (1376 x 1040 pixels), CCD camera. The pixel size for the CCD is $6.45 \mu\text{m} \times 6.45 \mu\text{m}$ and the quantum efficiency is approximately zero at 266 nm and 58% at the peak of the fluorescent spectrum. The analog to digital converter is 12-bit providing for a digital count between 0 and 4095. The analog to digital conversion factor is 4 electrons per count for low gain and 2 electrons per count for high gain. The maximum electrons that can be captured per pixel for high gain is 8,192 electrons and for low gain is 16,384 electrons. The full well capacity for this CCD is 18,000 electrons. The Sensicam was mounted to a tripod and pitched downward slightly in order to block some of the reflection on the surface of the top wall of the test section and the surface of the hemisphere (approximately 4° for wake centerline and multiple parallel plane data sets and approximately 2° for separation point centerline data set). The top wall of the test section does not transmit light and the 266 nm laser sheet was reflecting off of this surface and causing the wall to fluoresce. A 25 mm focal length lens was used with an aperture setting of f/1.6. A small extension tube was also used (length approximately 5mm). The spatial resolution and field of view for the planes in the flowfield are shown in Table 1.

Table 1: Spatial Resolution and Field of View for Planes Investigated

		Spatial Resolution ($\mu\text{m}/\text{pixel}$)	Field of View (mm x mm)
Wake	Region	33.07	45.51 x 34.40
Centerline	(All Sets)		
D/8		32.56	44.81 x 33.87
D/4		31.44	43.26 x 32.69
3D/8		31.05	42.73 x 32.29
D/2		30.24	41.61 x 31.45
5D/8		29.13	40.08 x 30.29
Separation	Region	23.35	32.12 x 24.28
Centerline			

B. Results and Discussion

1. Centerline Images

Figures 33 – 40 present samples of images obtained along the centerline of the hemisphere wake. Additional images can be found in the thesis of Reid (2011). The images have been fully processed as described earlier in the report with grayscale intensity values given in terms of the density ratio ρ/ρ_∞ . The colorbar has been scaled for appearance. In addition, the x and y axis are normalized by the hemisphere diameter. Only the portion of the image with adequate signal-to-noise ratio is displayed with the rest of the image filled in with zero values.

A common feature to all the images acquired is a large wake region separated from the free stream by a turbulent shear layer consisting of a series of vortices. The density in the wake varies depending on downstream distance and can be 20 – 40% lower than the free stream value. In general, the wake thickness is approximately the same height as the hemisphere, however, a

flapping motion is present producing large-scale structures with size on the same order of the hemisphere height.

A notable feature in these images is the severe drop in density at highly localized regions. These regions are thought to be associated with the low-pressure region of vortices formed in the weakly compressible shear layer separating the wake from the free stream. In some instances (e.g. Figs. 34 and 38), the density drop is as much as 50% of the freestream density. In general, however, the drop is on the order of 30% and varies from one vortex to the next. The magnitude of the decrease in density appears to correlate well with the size of the depression with larger drops associated with smaller cores. This picture is consistent the notion that stronger vortices possess smaller, tighter cores.

This observation alone is quite significant and possibly the most important outcome of the present work. As alluded to in the introduction, Jumper et al. have spent considerable time and effort developing a weakly compressible model to estimate the density fluctuations associated with the passage of large-scale structures in a shear layer. Their results indicated that vortices are marked by deep pressure and density wells that are not generally accounted for in other works. This is in contrast to the work of Catrakis et al. who did not detect the same density wells as predicted by Jumper et al. Their work, however, notably neglected the compressibility effects that would have led to these depressions and assumed density fluctuations are the results of mixing. This led to a mild debate about the nature of aero-optic distortions in compressible free shear layers. The results presented here clearly show the presence of these deep depressions. Furthermore, these results establish that these depressions can be quite significant in magnitude and must be accounted for to properly model the flow for aero-optics purposes.

The wake region is also marked by a severe flapping motion as the shear layer separating the wake fluid from the free stream fluid flaps significantly in the transverse direction. This flapping motion is marked by structures on the scale of the hemisphere height and can be observed in Figures 35 – 37. In general, when the wake is observed to be flapping, the free stream fluid and wake fluid are separated by a sharp interface with fewer shear layer vortices observed. In other instances, such as Figure 39, the flow exhibits a series of large vortices while in other cases (Figure 40) the shear layer/wake region is rather calm. Understanding what led to the flow in Figure 40 would be highly beneficial for aero-optic motivated flow control.

While it is too early to draw definitive conclusions, the flow appears to be dominated by two modes: a shear layer mode and a flapping wake mode. In the shear layer mode, the shear layer is dominated by strong vortices with deep density wells. The flapping is significantly reduced in this case. In the flapping mode, it appears as if the shear layer mode doesn't get a chance to fully develop and the flow is characterized by large sweeping motion of free stream fluid into the low density wake with a sharp interface between the two regions.

Ensemble average and standard deviation of the centerline wake region images are presented in Figures 41 and 42, respectively. The ensemble average consists of 98 images like those appearing in Figures 33 – 40. The density is lowest near the hemisphere and slowly increases with downstream distance as the free stream fluid mixes back in with the wake fluid. It should be noted that ensemble average reveals some room for improvement with respect to the image calibration process as discussed earlier. Low spatial frequency variations in density in the free stream are believed to be associated with a vignetting issue with the camera where the corners of

the image are ‘shaded’ relative to the center. A flat-field calibration can be used to correct for this, however, it was not implemented in time for this study.

The standard deviation of the normalized density images (the same 98 images used for the ensemble average calculation of normalized density), shows the locations where density fluctuation are the greatest. It should be noted that this measurement is not affected by the bias error discussed earlier. As expected, the fluctuations are most intense in the shear layer region where they are measured to be on the order of 12 – 14%. This is significantly less than the peak fluctuations observed in the instantaneous images and illustrative of the limitations one would face in the application of a RANS type of flow simulation for analyzing the aero-optics characteristics of the flow. The fluctuations extend into the wake region with downstream distance in accordance with the flapping motion observed earlier. The fluctuations in the free stream are indicative of the random error discussed earlier and can be reduced through imaging binning or low-pass filtering of the images in pre-processing.

Overall, this set of images is quite revealing as it illustrates several of the aero-optically interesting features of the flow in a manner that is directly applicable to the aero-optics problem. Unfortunately, time did not permit the acquisition of a larger set of images, which would have allowed for the application of techniques such as proper orthogonal decomposition to further characterize the feature observed in the flow.

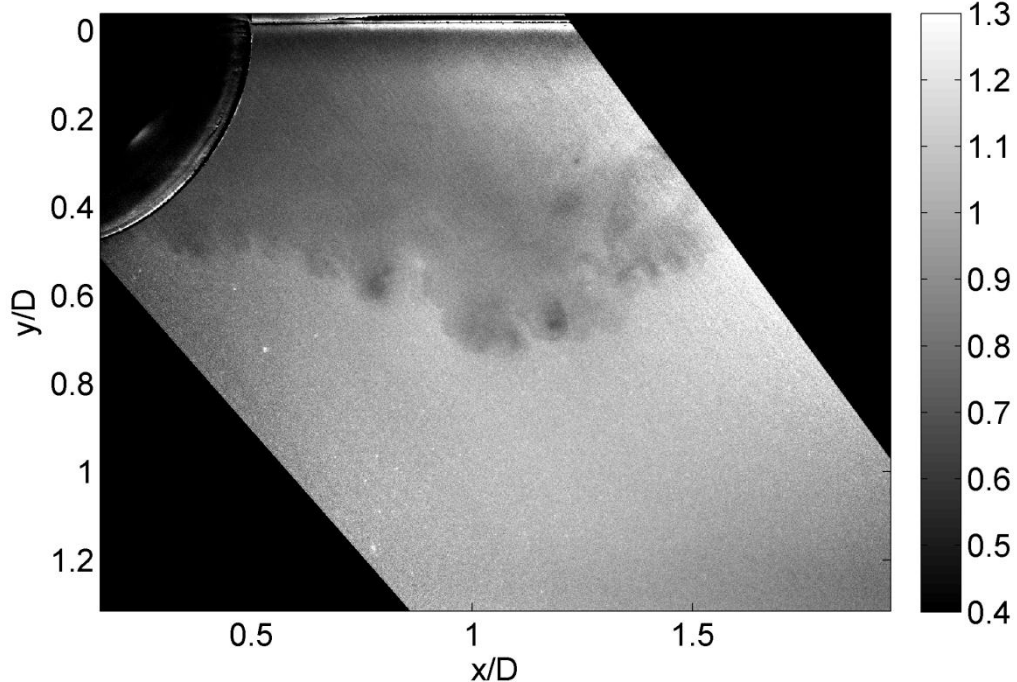


Figure 33: Example Single-Shot Acetone PLIF Density Image (values normalized to freestream)
– Centerline – Wake Region

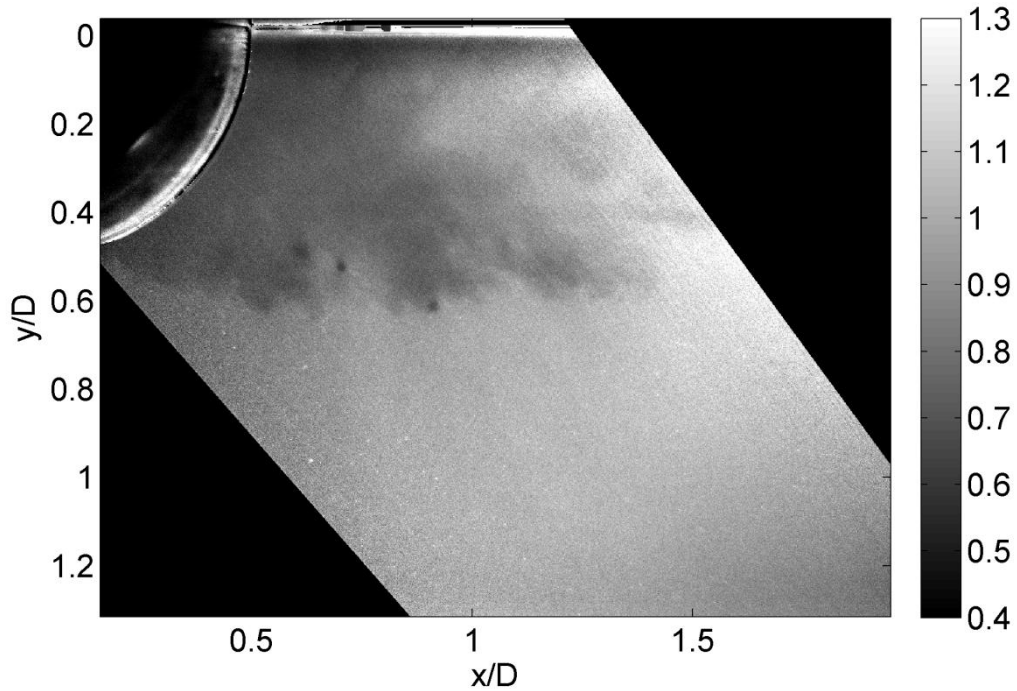


Figure 34: Wake Thickness of Single-Shot Acetone PLIF Density Image (values normalized to freestream) – Centerline – Region

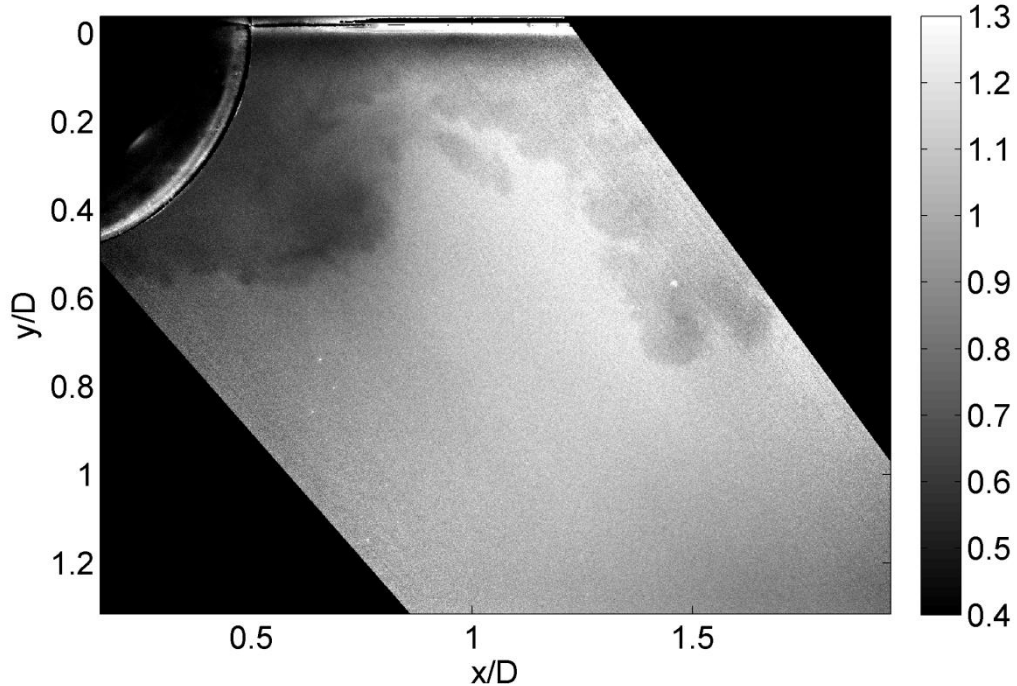


Figure 35: Flapping Motion in Single-Shot Acetone PLIF Density Image (values normalized to freestream) – Wake Region

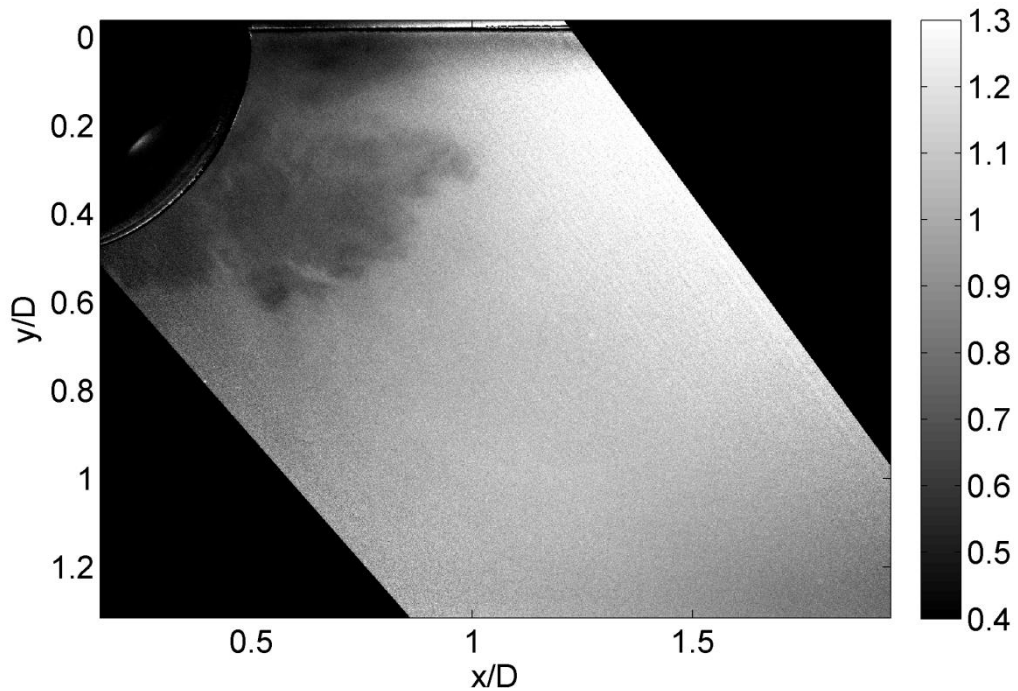


Figure 36: Abrupt Drop in Wake Thickness in Single-Shot Acetone PLIF Density Image (values normalized to freestream) – Centerline – Wake Region

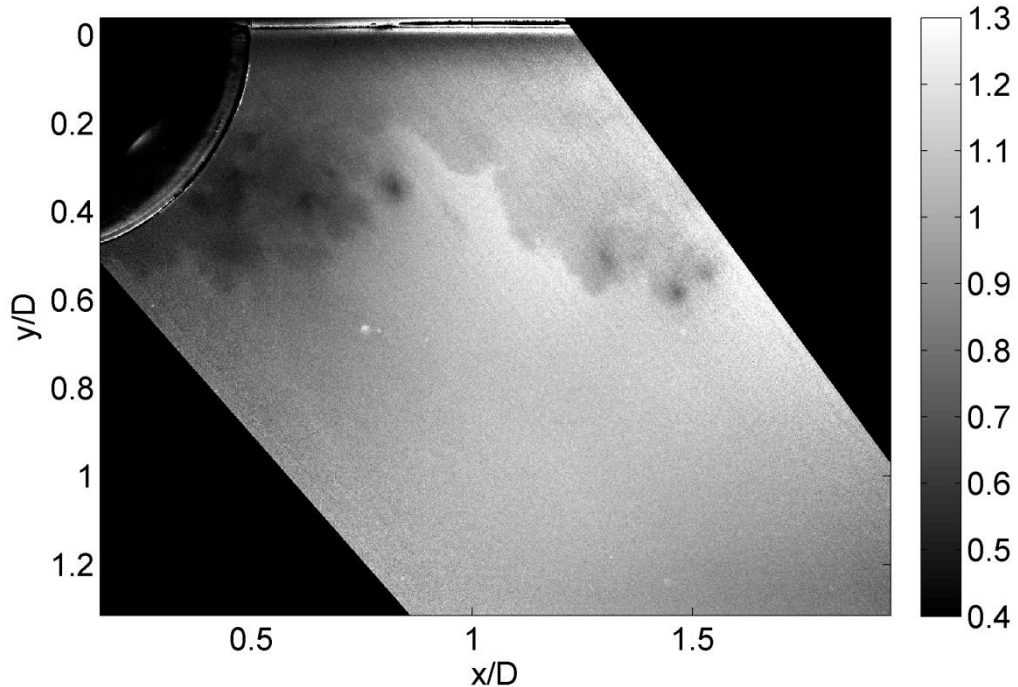


Figure 37: Vortex Cores in Single-Shot Acetone PLIF Density Image (values normalized to freestream) – Centerline – Wake Region

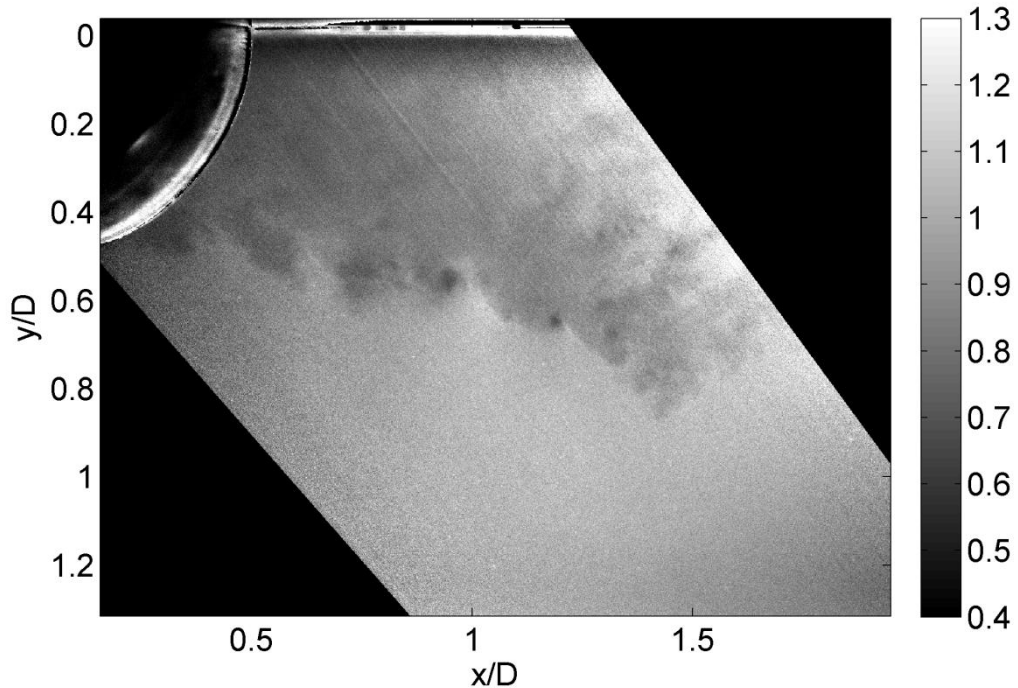


Figure 38: Swirling/Folding Motion Near Vortex Cores in Single-Shot Acetone PLIF Density Image (values normalized to freestream) – Centerline – Wake Region

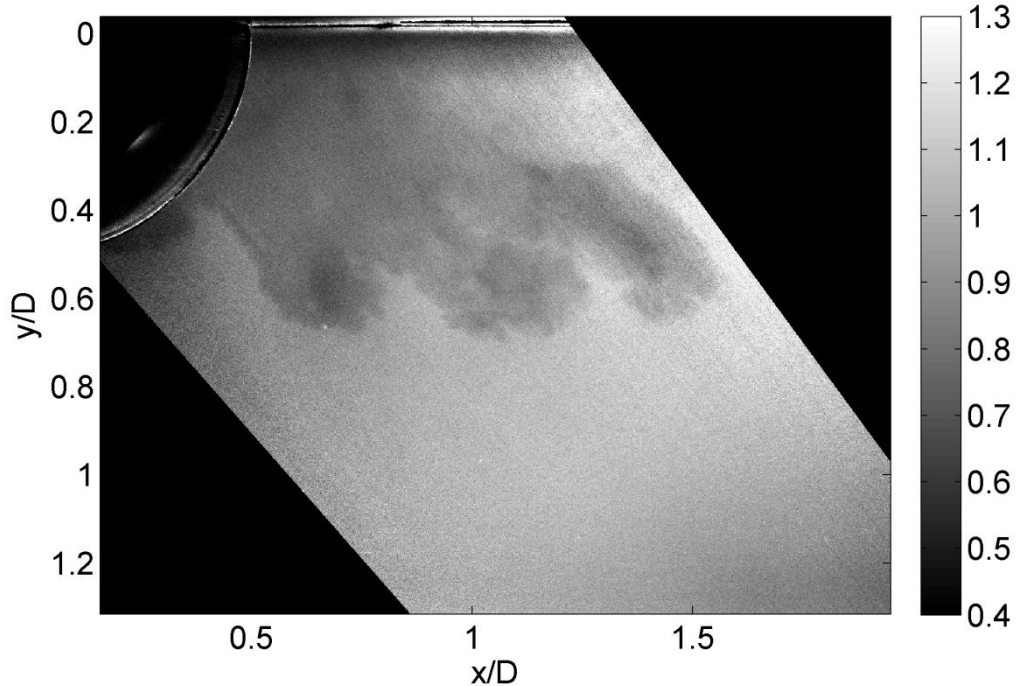


Figure 39: Large Protruding Structures in Single-Shot Acetone PLIF Density Image (values normalized to freestream) – Centerline – Wake Region

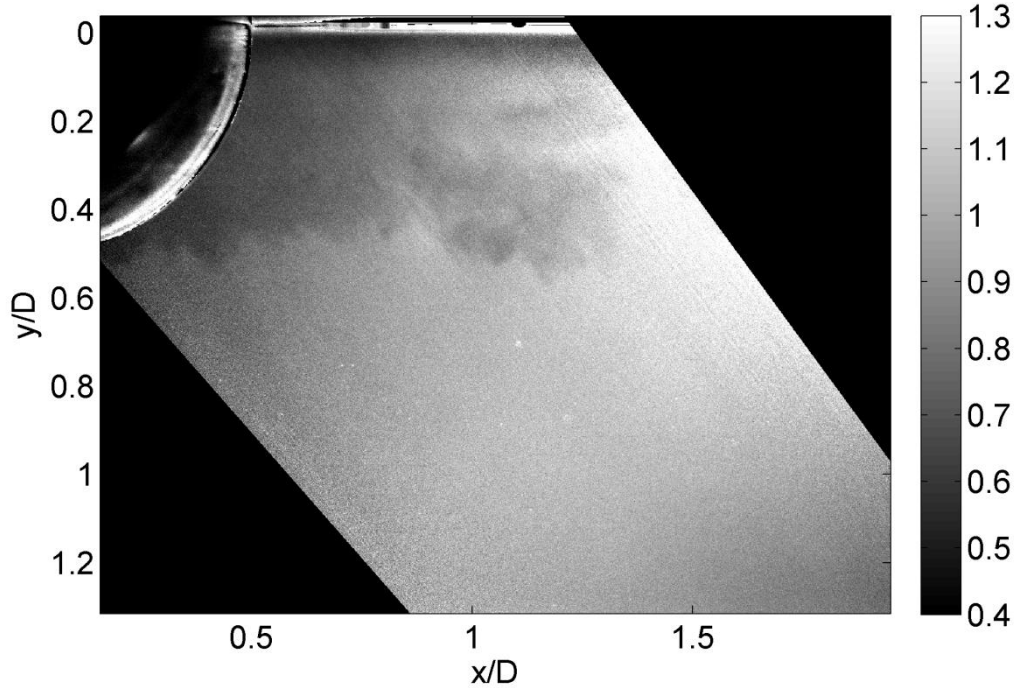


Figure 40: Fairly Calm Shear Layer and Wake in Single-Shot Acetone PLIF Density Image (values normalized to freestream) – Centerline – Wake Region

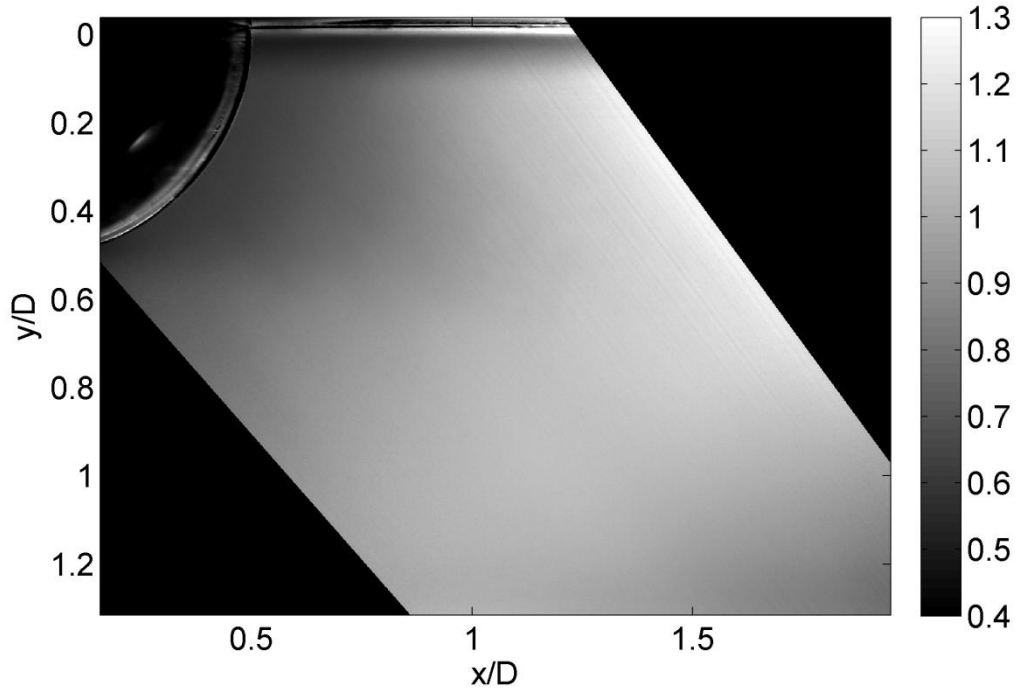


Figure 41: Ensemble Average of Single-Shot Acetone PLIF Normalized Density Images – Centerline – Wake Region

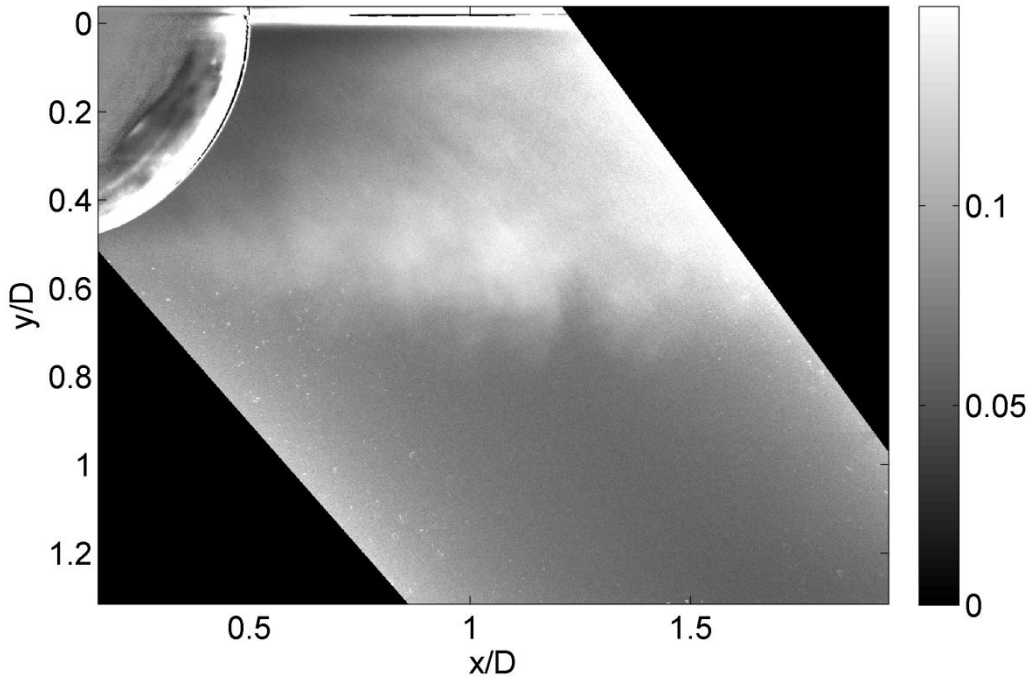


Figure 42: Standard Deviation of Single-Shot Acetone PLIF Normalized Density Images – Centerline – Wake Region

2. Off-Centerline Images

Images were also acquired along streamwise-transverse planes shifted off of the centerline of the hemisphere. The purpose of these images was to investigate some of the three-dimensionality of the structures shed from the hemisphere. Images were acquired for a shift of $D/8$, $D/4$, $3D/8$, $D/2$ and $5D/8$ with approximately 25 images acquired at each location. Figures 43 – 47 show a sample image acquired at each plane. Additional images can be found in the thesis of Reid (2011).

The $D/8$ plane images revealed characteristics similar to the centerline plane, as expected due to proximity. The wake was still clearly present in each image along with flapping motions and vortex cores as discussed previously. The magnitude of the density wells is similar as well.

Images from the $D/4$ plane revealed a similar structure with dark vortex cores and a flapping wake still observed; however, several images, such as Figure 44, show a wake region significantly smaller than observed earlier with the free stream fluid approaching quite close to the wall. This could be indicative of an out-of-plane flapping motion in addition to an in-plane flapping motion.

Images from the $3D/8$ plane continue to reveal fairly tight and strong vortex cores in the shear layer and upper wake region indicating that the shear layer is formed over a significant portion of the top of the hemisphere. The flapping motion of the wake continues as expected, but is slightly smaller as the imaged plane is moved further from the centerline.

The $D/2$ plane corresponds to the forward edge of the hemisphere and is marked by a much more sporadic appearance of low density fluid, presumably due to the growth of the shear layer region

and flapping of the wake in the out-of-plane direction. Tight vortex cores are not visualized in this region with the low density structures being more in the form of large puffs. The density drops in these puffs were comparable to the density drops experienced in the planes closer to the centerline. In some images, the bottom portions of the wake could be seen, but the thickness was frequently less than half of the diameter of the hemisphere. In other images no wake could be seen at all.

The 5D/8 plane images did not show much detail at all as the plane is located outside of the extent of the wake region. Only a few images showed any relative changes in the density downstream of the hemisphere. Again these changes in density were characterized by dark puffs that appeared in the middle to lower portion of the wake region, but again these puffs were very infrequent.

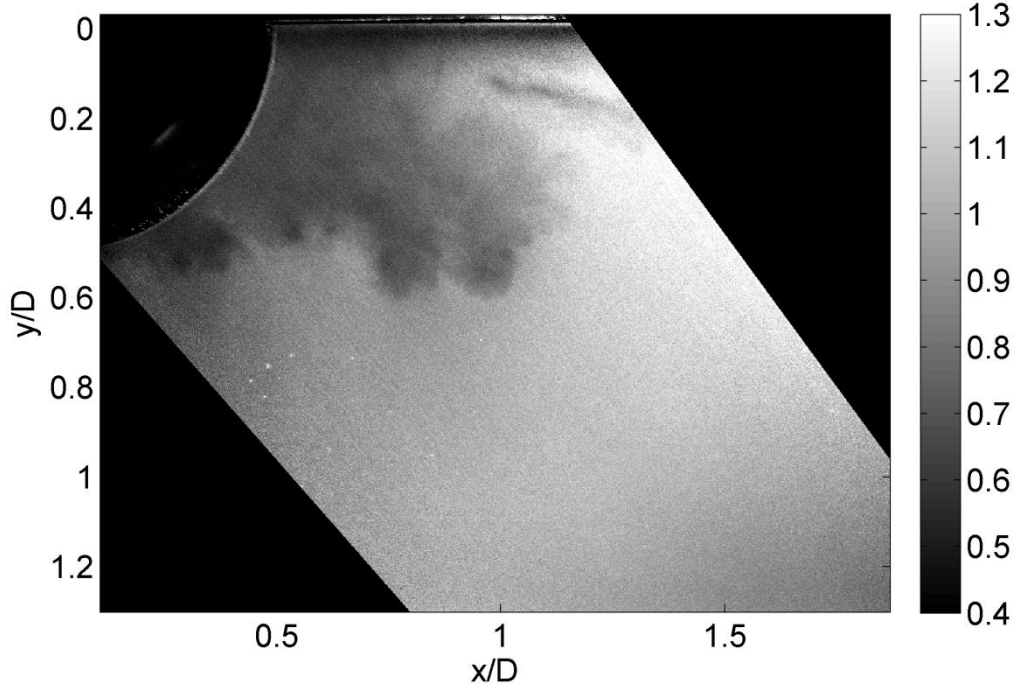


Figure 43: D/8 Plane Single-Shot Acetone PLIF Density Image (values normalized to freestream)

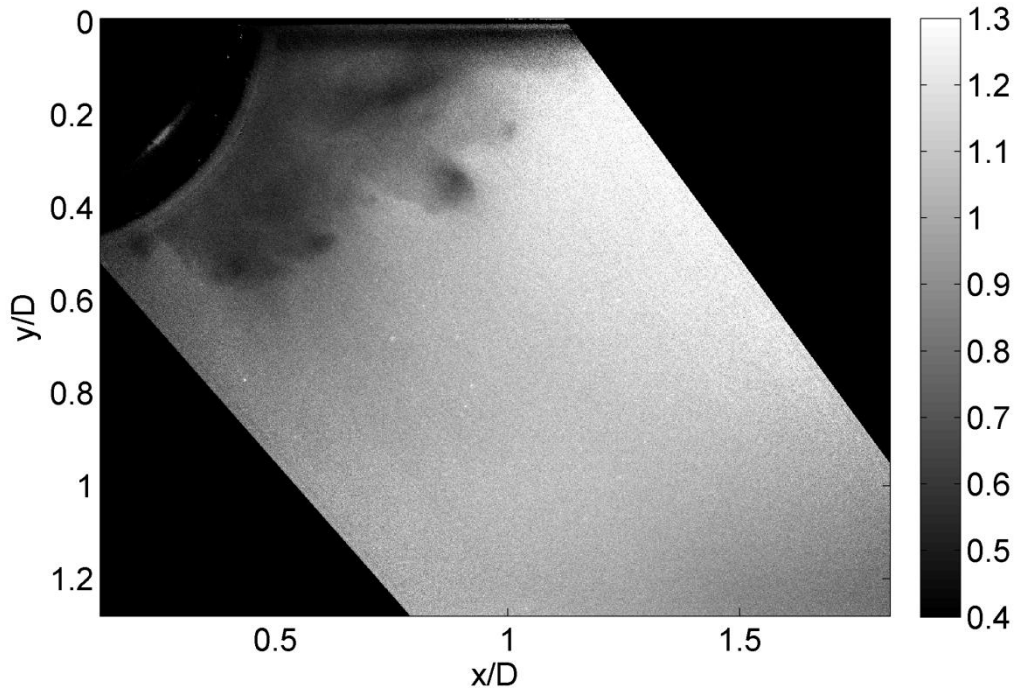


Figure 44: $D/4$ Plane Single-Shot Acetone PLIF Density Image (values normalized to freestream)

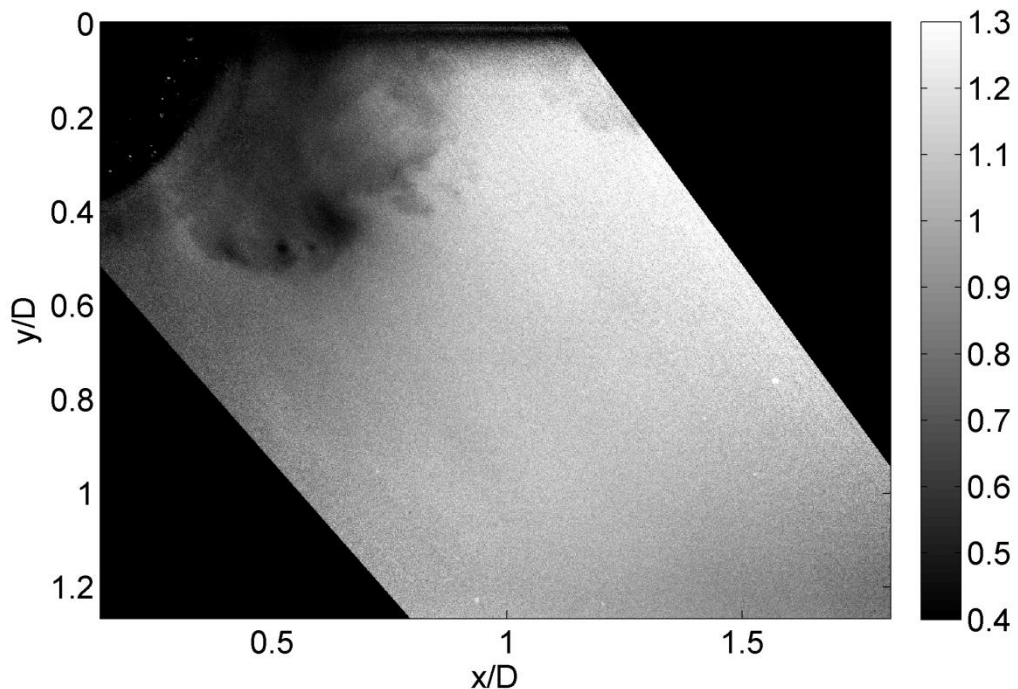


Figure 45: $3D/8$ Plane Single-Shot Acetone PLIF Density Image (values normalized to freestream)

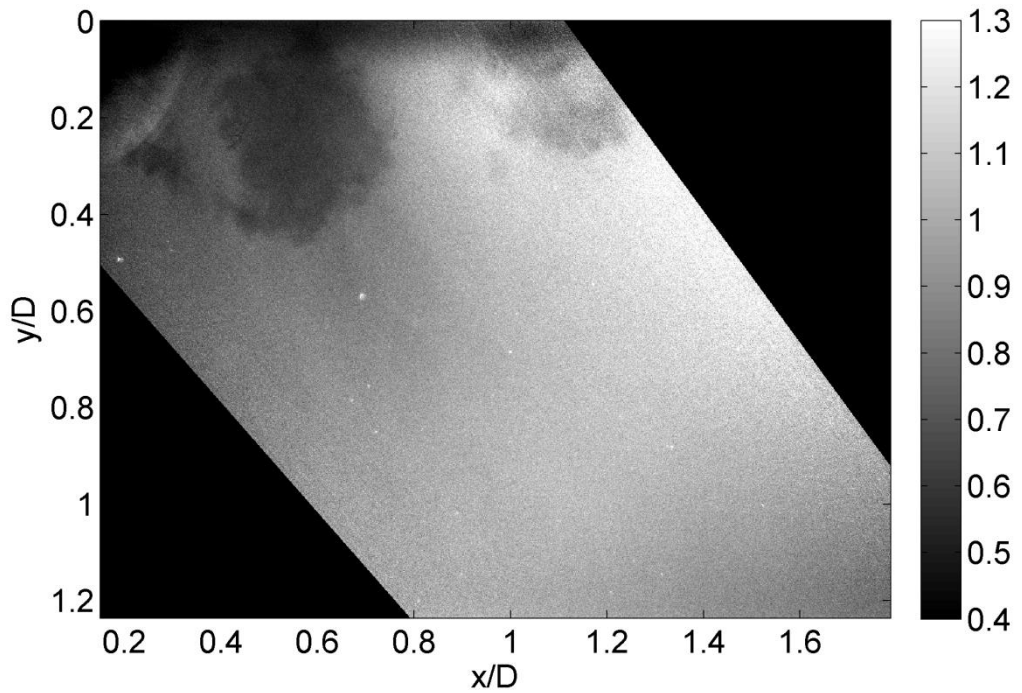


Figure 46: D/2 Plane Single-Shot Acetone PLIF Density Image (values normalized to freestream)

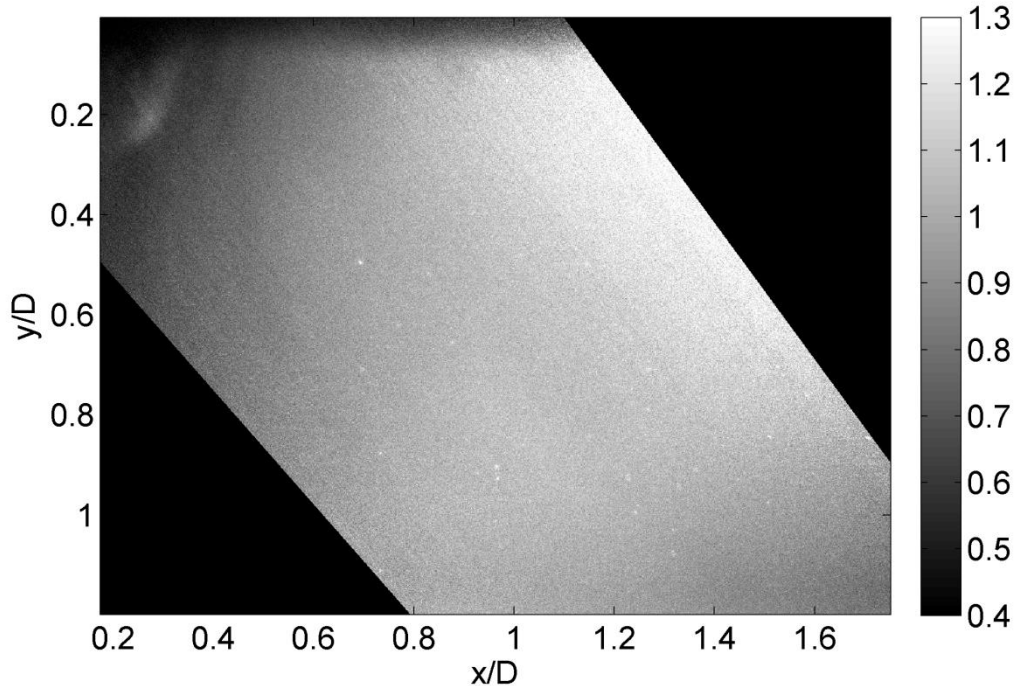


Figure 47: 5D/8 Plane Single-Shot Acetone PLIF Density Image (values normalized to freestream)

3. Separation Region – Centerline

An additional set of experiments was conducted along the centerline, but with the field of view focused more closely on the separation region on the top of the hemisphere. Figures 48 and 49 show two images acquired in this region of the flow. The most striking features of these images is the visualization of the shock induced separation and the different forms that it takes in this case. In Figure 48, fairly weak shocks are observed emanating from the shear layer region. Strong vortex cores are not yet observed, presumably since they haven't had sufficient time/space to form. In Figure 49, a large lambda shock is observed followed by a series of smaller shocks. A comparison between the two images shows the shear layer being shed at a slightly different angle. The separation point was typically located at approximately 80° - 90° from horizontal as there was some variation in this location from image to image.

The presence of shocks creates a certain amount of ‘shading’ in the images as the incident light rays are refracted by the shocks. This is not currently accounted for in the image processing steps; however, it is theoretically possible to devise an iterative scheme that accounts for local changes in laser fluence based on gradients in the density field.

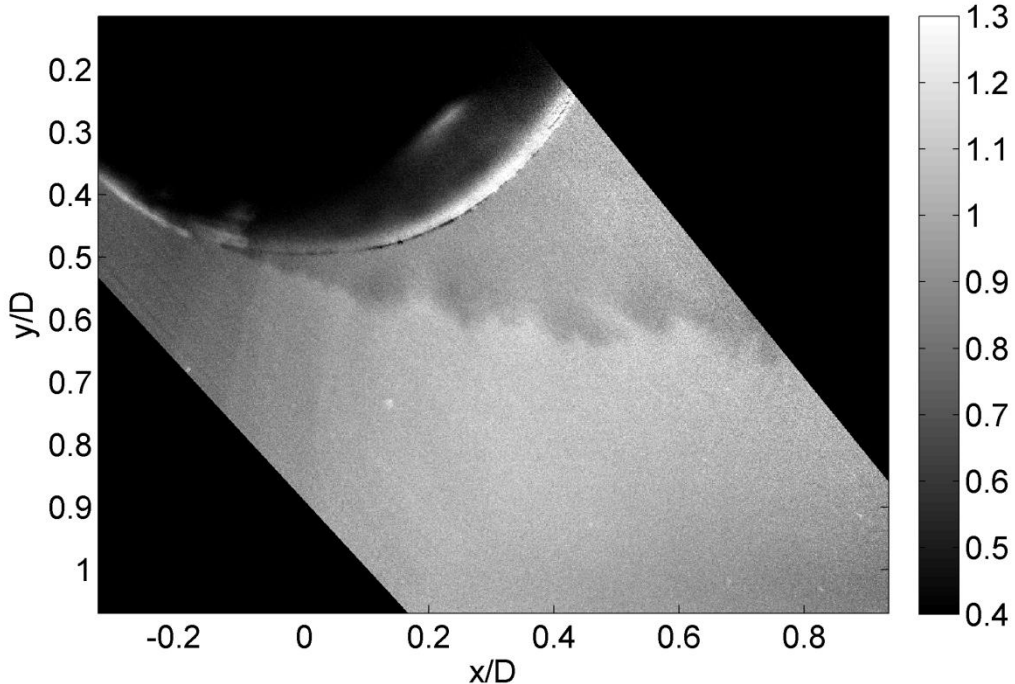


Figure 48: Weak Shocks for Single-Shot Acetone PLIF Density Image (values normalized to freestream) – Centerline – Separation Region

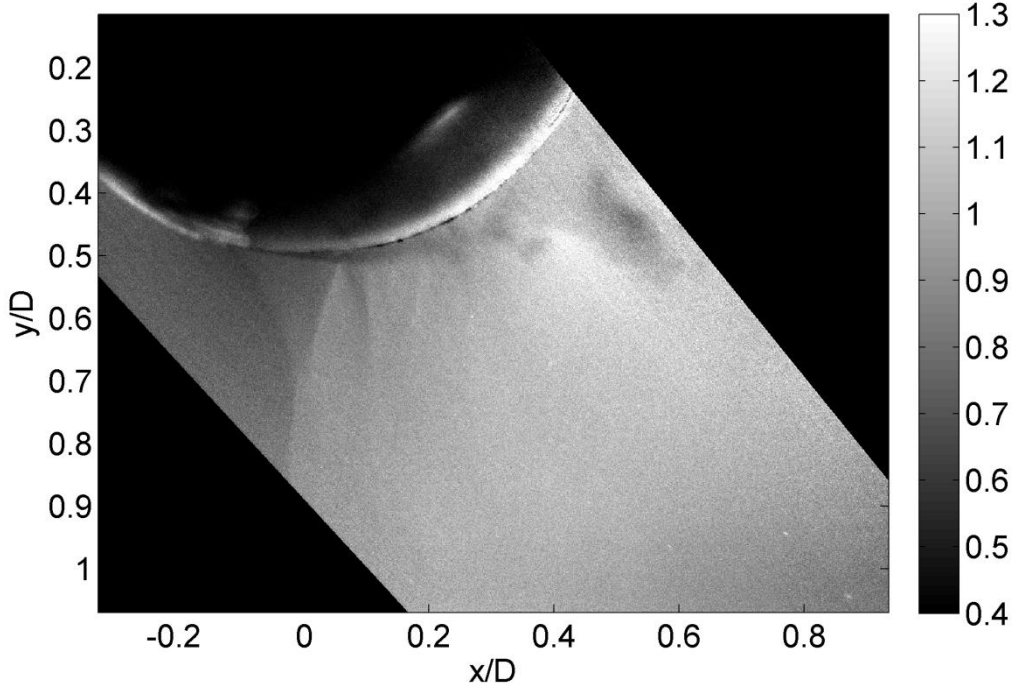


Figure 49: Lambda Shocks for Single-Shot Acetone PLIF Density Image (values normalized to freestream) – Centerline – Separation Region

C. Conclusions and Recommendations for Future Work with Acetone PLIF

Overall, the results presented here clearly demonstrate the utility of acetone PLIF for density measurements in a transonic flow field. The ability to visualize shocks, the decrease in density within the core of a vortex and the large-scale flapping motion of the wake region illustrate the variety of flow features that can be observed with this technique. Tools for understanding the aero-optic characteristics of the flow field are discussed in the next section; however, it can be observed directly from the density data that both the shear layer structure and large scale motion of the wake are of critical importance.

The analysis of images presented here was quite limited in scope for many reasons. First, the main objective of this work was development of the technique, which consumed the vast majority of the time and effort associated with this project. This included design and construction of the transonic test section, acetone seeder and the image processing algorithms used for data reduction. Now that the technique has been developed and the infrastructure is in place, application of the technique for more extensive measurements should be more straightforward. It is recommended that future investigations take a more detailed look at this flow geometry using a much larger set of images over a wider field of view. This will require a more powerful laser; however, the benefits will be a more complete view of the flow as both the separation region and resulting wake structure can be resolved simultaneously. It would be interesting to see how the shock structure formed on the front of the hemisphere correlates with the wake motion. In addition, the number of images acquired should be much larger to allow for reduced order modeling techniques such as POD and 2-D space correlations to be computed so that a more representative look at the structures in the wake can be determined.

V. Wavefront Measurements using Acetone PLIF

From an aero-optics perspective, the main benefit of acetone PLIF is that virtual wavefronts can be propagated through the density field data in order to estimate the wavefront distortion that would be induced by the flow field. Thus, a single image can be used to analyze the degree of distortion for multiple angles and aperture sizes, greatly decreasing the number of experiments that would need to be conducted. As part of this work, several tools were developed to look at the wavefront distortion. This section describes these tools and presents some preliminary results. A more extensive study is recommended for a future investigation.

The first step in the process of calculating aero-optic distortion is calculating the indices of refraction of each density field image using Eq. 3. The value of $K(\lambda_{wf})$ varies slightly depending on the wavelength of the wavefront. For 532 nm, $K(\lambda_{wf}) \approx 2.27 \times 10^{-4} \text{ m}^3/\text{kg}$, and is used here. An index of refraction value of 1.000, which is the index of refraction for air in a vacuum, is assigned to all points inside of the hemisphere using a masking procedure. To make sure that no fluorescence on the surface of the hemisphere is interfering with the wavefront distortion calculations, this masking procedure actually extends slightly beyond the actual radius of the hemisphere. In essence, a slightly larger diameter hemisphere with all index of refraction values equal to 1 is placed over the actual hemisphere in the image.

The beam/wavefront characteristics are specified next. In this work, only planar wavefronts were investigated, each with 100 rays equally spaced apart, physically/geometrically equal in length, and parallel to one another. The beam diameter was set to be 1/3 of the diameter of the hemisphere, which is representative of an actual optical turret and consistent with aperture sizes investigated elsewhere. The wavefront passed from the starting plane at the center of the hemisphere to the freestream at a propagation angle of 0.60 radians (approximately 34.4 degrees) for the centerline wake region images. The beam did not extend all the way to the bottom right corner of each image because of the dark regions that could not be eliminated during image processing. This would appear as a lower index region than the freestream and would alter results. A sample index of refraction field image is shown in Figure (with the propagating wavefront displayed) and in Figure (with only the outline of the propagating wavefront displayed). Additional example wavefronts and their associated distortion values are presented in the thesis of Reid (2011). It should be noted that it is easy to adjust the aperture size, angle and number of rays within the software program so that a user can easily examine different scenarios for a given image. Time did not permit a more detailed investigation within this work.

For a single index of refraction image for a single propagation angle, the *OPL* was calculated for each ray. This was done by integrating the index of refraction values for each ray from the starting plane at the center of the hemisphere to the freestream region using Equation 3. It is implicitly assumed that the deflection of a ray is sufficiently small such that the path over the image area can be assumed to be along a straight line. \overline{OPL} , the mean spatial *OPL* across the aperture, was calculated and subtracted from the *OPL* value for each ray to yield an *OPD* value for each ray. This entire process was repeated for all instantaneous images to yield a set of *OPD* values for each image for a single propagation angle.

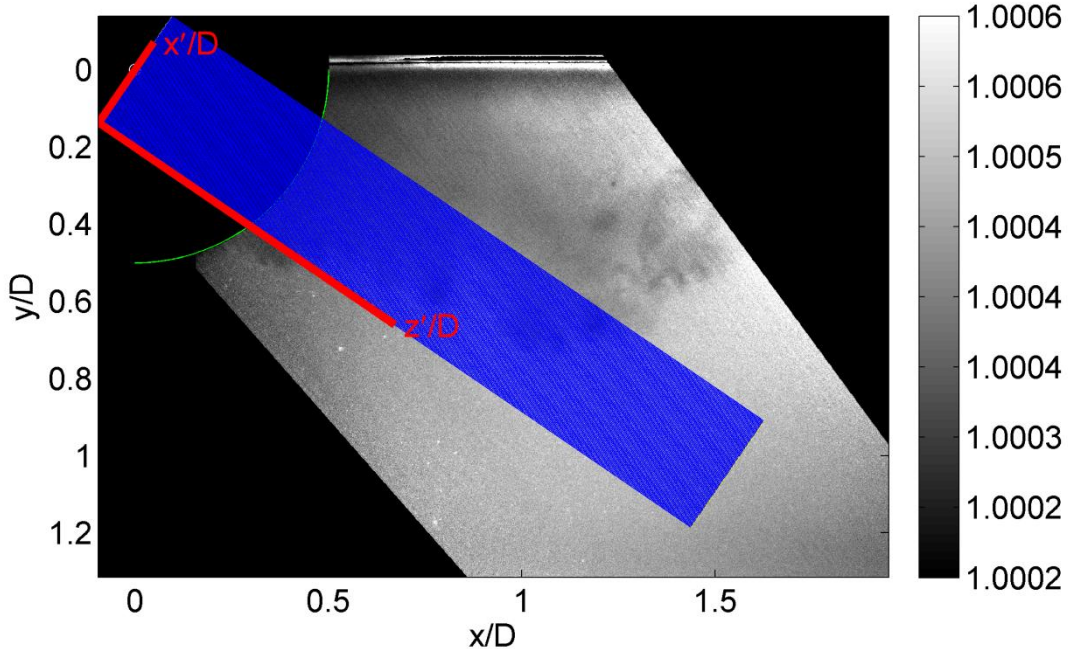


Figure 50: Example Index of Refraction Image with Wavefront Geometry Drawn

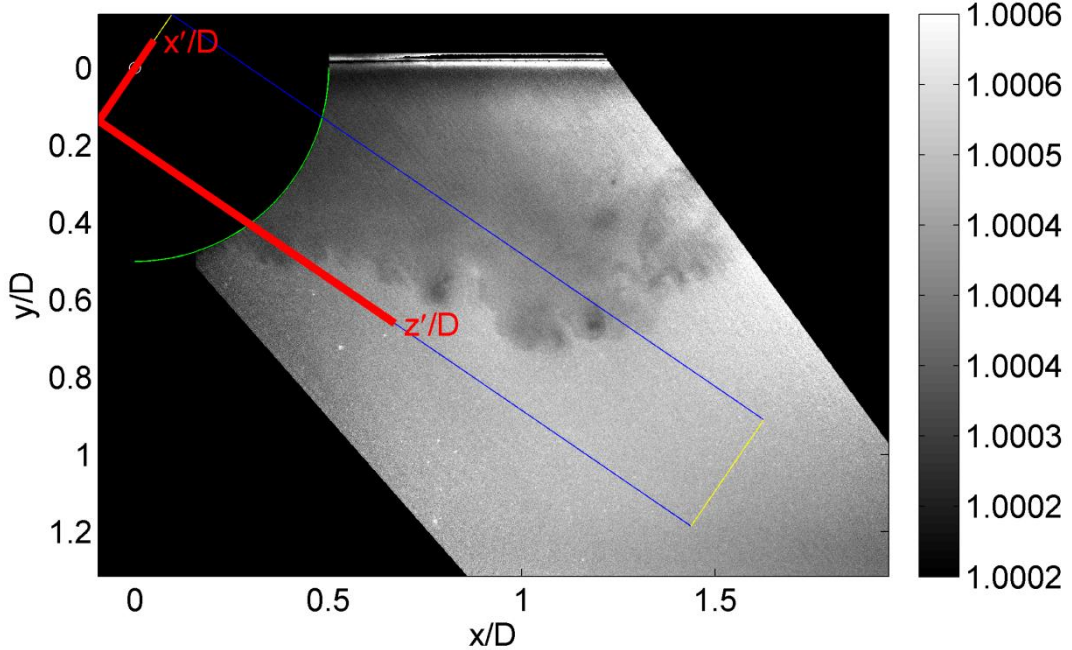


Figure 51: Example Index of Refraction Image with Outline of Wavefront Geometry Drawn

A plot of OPD for the index of refraction image in Figure and Figure 51 is shown in Figure. As can be seen, the OPD is greatest near $x/D=0$ as the wavefront must pass through a greater portion of higher density free stream fluid. This distortion would lead to a tilting of the wavefront and cause the beam to be steered off of its original axis. It is interesting to note that for this particular angle of propagation, the position of the wake causes a more significant amount of

distortion than individual structures contained within the shear layer. This tends to be true for all of the images acquired in this study indicating that the wake dynamics are more important than the shear layer dynamics. Thus, one might be able to tolerate a certain amount of vortices in the shear layer if it stabilizes the wake region.

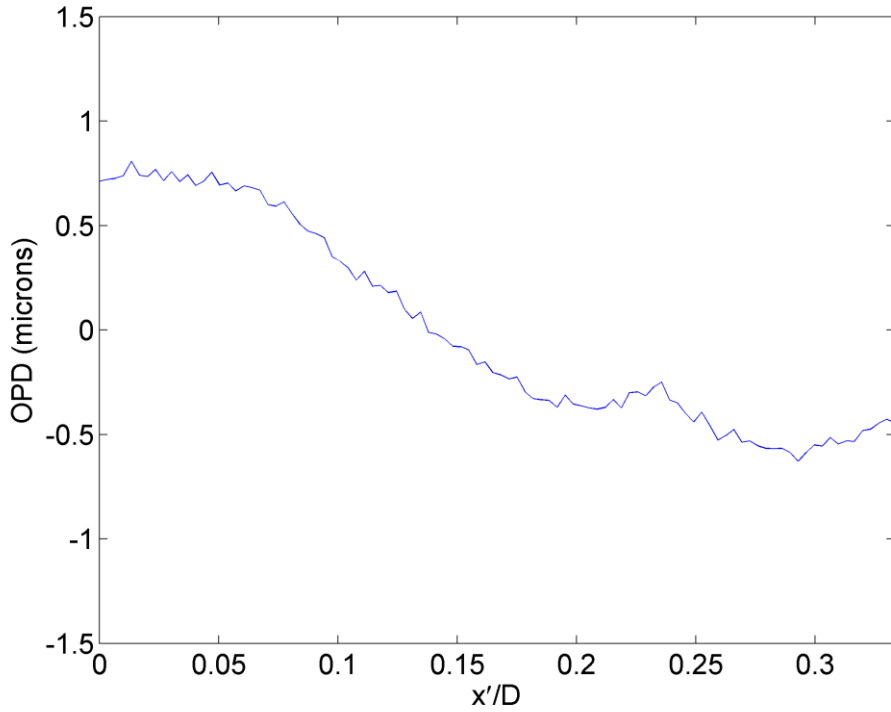


Figure 52: Plot of OPD vs. x'/D for Example Index of Refraction Image

One measure of the degree of wavefront distortion is the magnitude of fluctuations in the OPD. The magnitude of these fluctuations, OPD_{rms} , for the images acquired here is shown in the scatter plot of Figure 53 and the histogram of Figure 54. Here it can be seen that the degree of wavefront distortion varies significantly with time with the magnitude of fluctuations ranging from 0.1 to 0.6 microns.

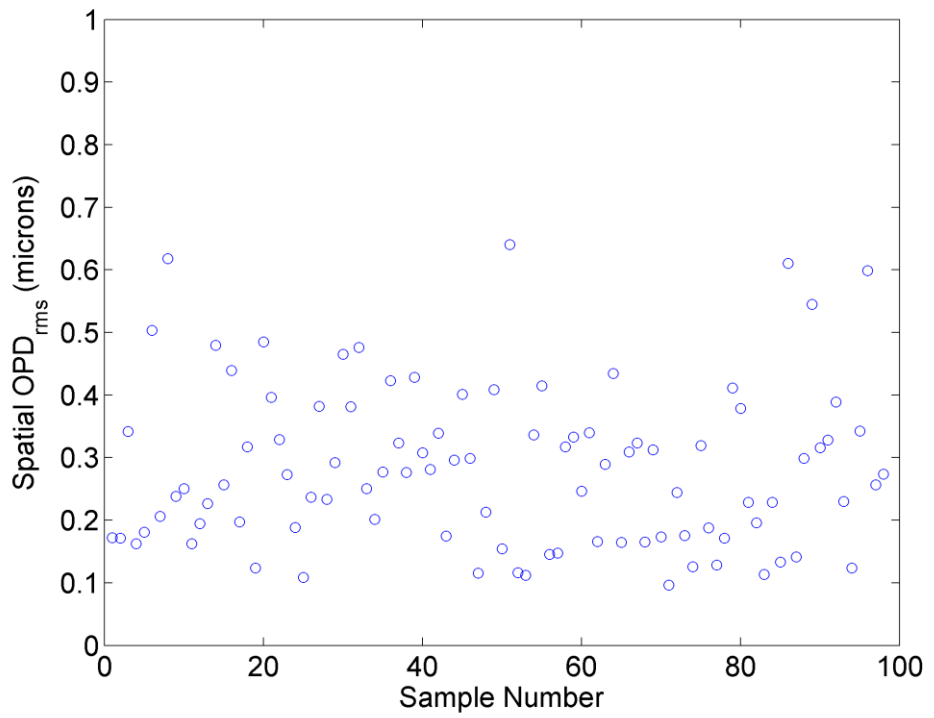


Figure 53: Scatter Plot of Spatial OPD_{rms} Values for Images

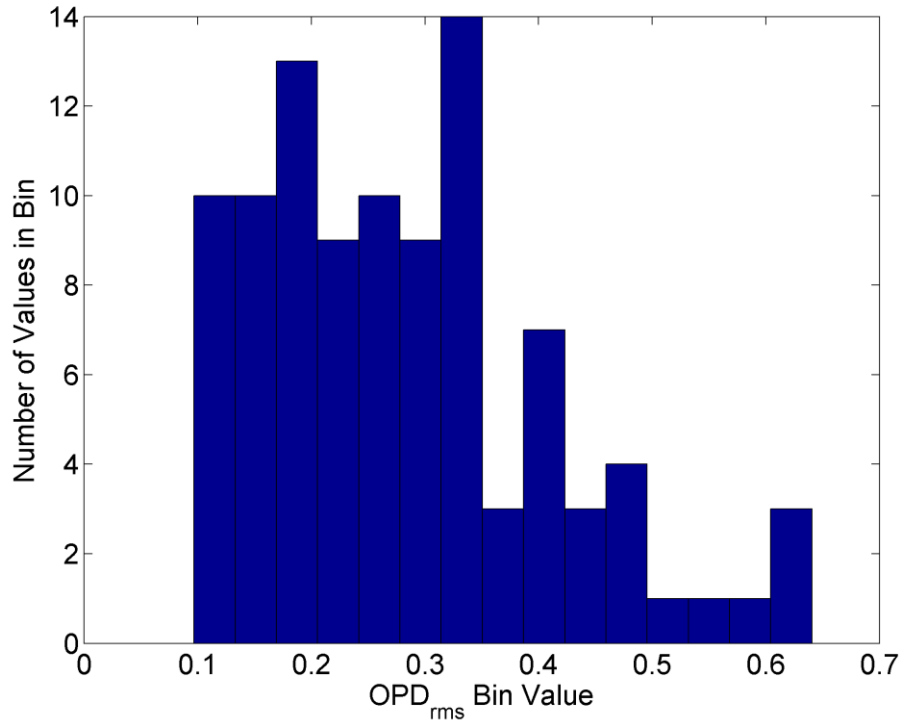


Figure 54: Histogram of OPD_{rms} Values for Images (15 bins)

The OPD includes a steady component associated with the time average flow and the propagation of the planar wavefront through the hemisphere. This portion was found by calculating the ensemble average $\langle OPD \rangle$ and is shown in Figure 55. The concave shape observed in the time average distortion is believed to be mostly due to the curvature of the hemisphere, which would cause the beam to focus. The magnitude of the ensemble average is between -0.1 and 0.1 over a large portion of the flow as compared to the larger variations observed in the instantaneous wavefronts.

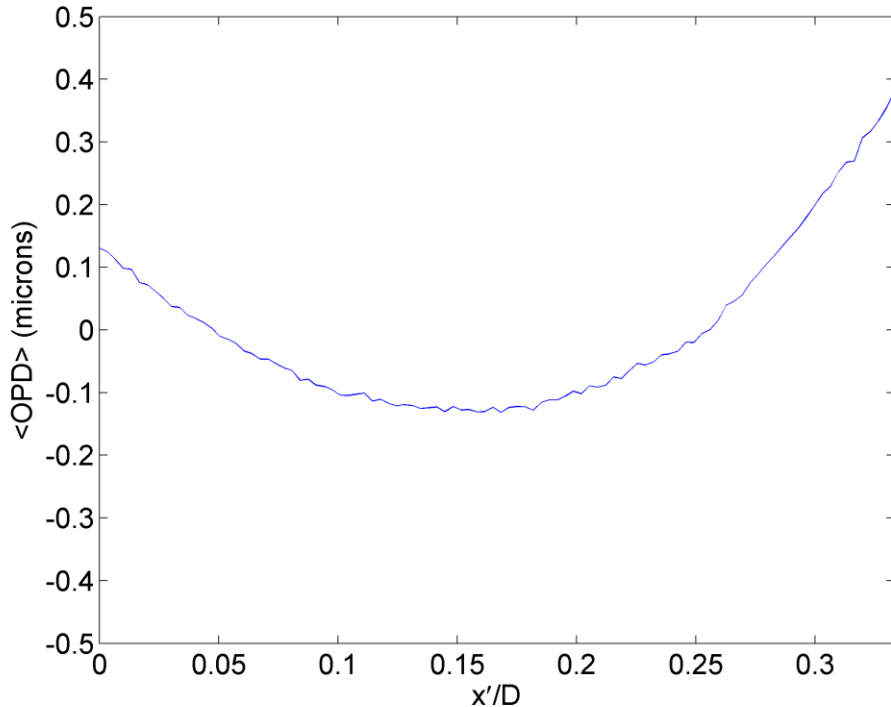


Figure 55: Plot of $\langle OPD \rangle$ vs. x'/D

For a real application, however, it is the unsteady component of the distortion that is of the most significance as the steady component can be removed through adaptive optics and other beam control systems. The unsteady portion of the wavefront distortion is given as $OPD' = OPD - \langle OPD \rangle$. A plot of OPD' vs. x'/D for the image shown earlier is given in Figure 56. In this case, removal of the steady component only has a modest effect on the shape of the wavefront. Again, the wake can be seen to impose a large degree of tilt on the beam with lower magnitude smaller scale features associated with the shear layer structures riding on top.

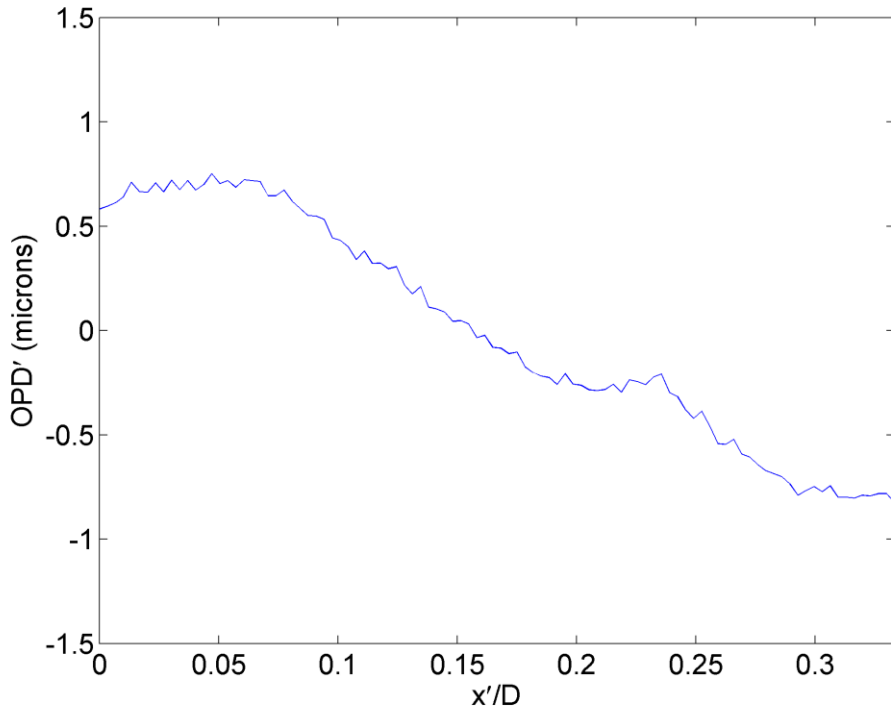


Figure 56: Plot of OPD' vs. x'/D for Example Index of Refraction Image

Overall, these results illustrate the ability to calculate wavefront distortions from acetone PLIF images. While results are preliminary, it appears that the large-scale motion of the wake plays a more significant role than the smaller structures contained in the shear layer. It is recommended in future work to use these tools to investigate the characteristics over a wider range of conditions (beam size, propagation direction). This ability would be significantly enhanced through the use of images with a wider field of view as recommended in the previous section.

VI. Time-Resolved & 3-D LIF

As indicated in the title and objective, the long-term, far-reaching goal of this project was to develop acetone PLIF into a 3-D measurement technique. The basis for this idea is the availability of a unique MHz rate pulse burst laser system whereby a high repetition rate laser sheet is scanned through the flow field using a galvanometric scanning mirror and imaged with a high-speed camera. This technology has successfully been utilized for 3-D flow visualization, such as the 3-D images of a turbulent jet shown in Figures 57 and 58. The jet was seeded with smoke and illuminated using the 532 nm output of the laser. These images were constructed from a sequence of 100 images acquired at a framing rate of 1 MHz.

For 3-D LIF, the challenges are to convert the output of the pulse burst laser to 266 nm and image the acetone PLIF signal with a high-speed camera. In this work, a time-resolved measurement was attempted under the premise that extension to 3-D would simply involve adding a scanning mirror to the arrangement. This effort was attempted using two types of cameras with the details given below. We note that while this effort was not successful, there are still plenty of reasons to be optimistic about the application of 3-D acetone PLIF in the future. These reasons are also discussed in this section.

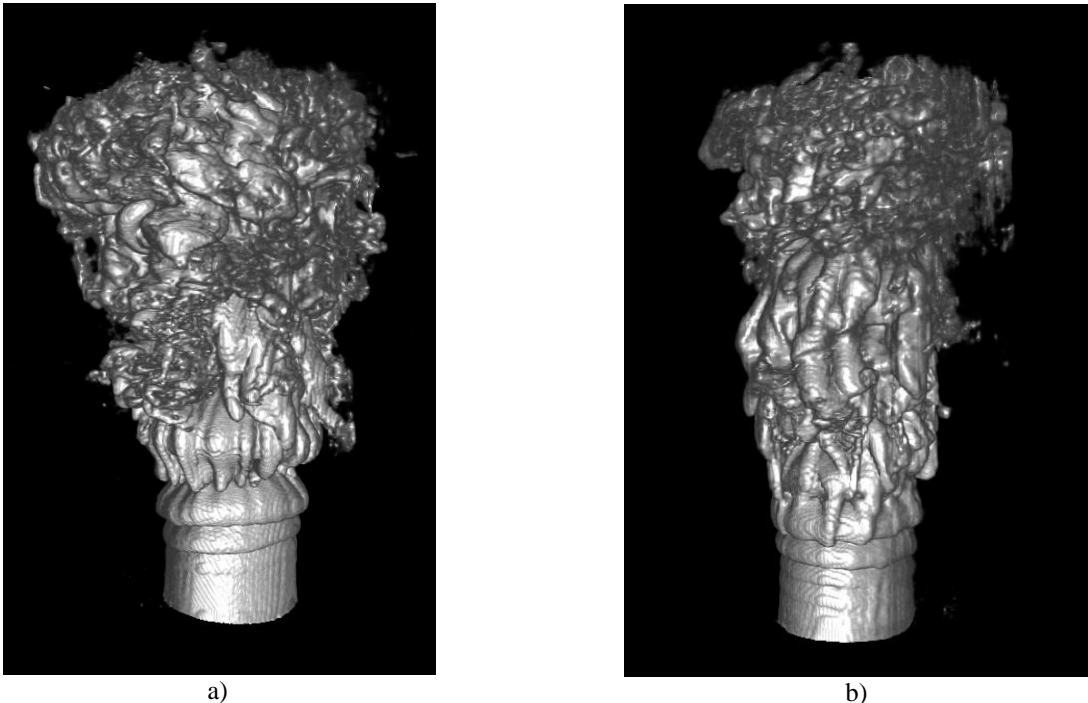


Figure 57: 3-D Flow Visualization Images of a turbulent jet at $Re = 10,200$. Images depict an iso-surface based on image intensity from the 3-D data cube.

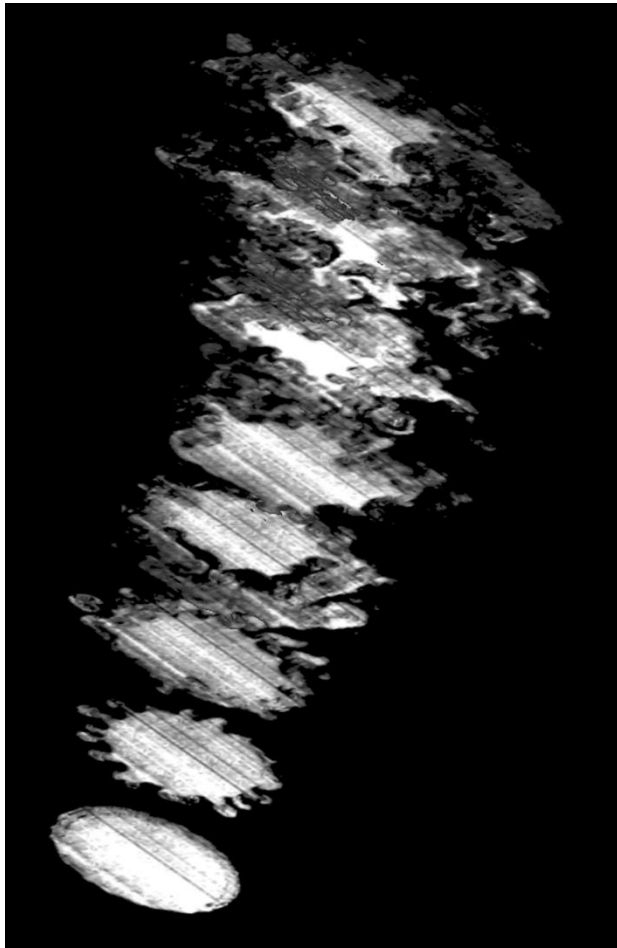


Figure 58: Cross-sectional views of the jet at $Re = 10,200$. Rendering spans from x/D 0.6 to 3.9.

Excitation for time-resolved acetone PLIF was provided by a megahertz rate pulse burst laser system (B. a. Thurow 2009), (B. S. Thurow 2009), (J. L. Reid 2010). This laser is currently capable of creating 15 mJ/pulse of 532 nm light at 500 kHz, which corresponds to the framing rate of an available high-speed camera. In this optical setup, the 532 nm light was converted to 266 nm (resulting in an energy output of approximately 4 mJ/pulse) using a BBO crystal. The laser sheet was passed through the bottom window of the test section in a normal orientation (not angled as was done in the single-shot experiments because time-resolved tests were performed prior to the single-shot experiments). The laser sheet was located along the centerline of the hemisphere and did not move position. An $f=100$ mm spherical lens, an $f=150$ mm spherical lens, and an $f=30$ mm plano-concave cylindrical lens were used to create the approximately $200 \mu\text{m}$ thick and 3.5 inches wide laser sheet. As in the single-shot acetone PLIF experiments, the first spherical lens expanded the beam, the second spherical lens focused the beam, and the cylindrical lens formed a thin laser sheet when the focusing beam passed through it.

For the first attempt at time-resolved acetone PLIF, a DRS Hadland Ultra 68 camera was used for imaging and the pulse burst laser for illumination. This camera has a resolution of 220px x

220px and can operate at up to 500,000 frames per second in bursts of 68 images (B. a. Thurow 2009). A 50 mm focal length lens was used with no extension tube.

For the second attempt at time-resolved acetone PLIF, a Specialised Imaging SIM02 – Multi-Channel Framing Camera was used for imaging and a SOLO III PIV laser used to provide a single illumination pulse. This camera has a much greater spatial resolution than the Ultra 68 camera, having a resolution of 1360 px x 1024 px. This setup was actually not time-resolved per se, but the goal behind this particular attempt was to see if this camera could obtain an adequate acetone PLIF image under the same conditions that a conventional CCD camera yields adequate results.

In both attempts, the cameras were unable to acquire sufficient signal to visualize the turbulent wake behind the hemisphere. There are distinct reasons why the time-resolved acetone PLIF experiments did not yield quality data. One reason is that the pulse burst laser system only provides 266 nm excitation energy of approximately 4 mJ/pulse, whereas the SOLO III PIV Laser and SOLO 200XT PIV laser provide approximately 22 mJ/pulse and 38 mJ/pulse (before passing through final optical components), respectively. This in principle should cause the signal to drop by an order of magnitude when using the pulse burst laser system versus the SOLO 200XT PIV Laser although we note that attempts with the SOLO III were also unsuccessful.

The most important factor, however, is associated with the sensitivity of the high-speed cameras. While both of the cameras used in these tests are intensified, their architecture significantly handicaps their ability to image at low light levels. Both cameras utilize multiple beam splitters to divide the image into separate paths. In addition, the optical arrangement of the cameras limited the collection f#. Taken together, it is estimated that the number of photons reaching the intensifier is approximately 2 orders of magnitude less than that experienced with the Sensicam QE used in the single shot experiments. Thus, the intensifier did not receive enough signal to yield quality images. The reason we remain optimistic, however, is that these cameras were used based on their availability as opposed to acquiring a camera expressly for the purposes of acetone PLIF. The Ultra68 camera was acquired prior to this grant for use in a 3-D flow visualization system and the SIM02 was used as part of a 1 day demo by its manufacturer.

The reason for our optimism is that several high-speed camera technologies are available, or are in production, with the characteristics necessary to achieve sufficient image quality. These include technology from Shimadzu, MIT's Lincoln Laboratories (in development), and Princeton Scientific Instruments. These camera designs are based on custom CCD sensors that utilize on-chip storage so that beam splitters and intensifiers are not necessary. In addition, the cameras have large pixels so that more photons are collected at each pixel location. In addition, the pulse burst laser is being upgraded to yield higher output power providing an additional boost in signal.

As an example, consider the Princeton Scientific Instruments, Inc. PSI-4 camera, a camera which the PI has used in the past. The camera has a resolution of 80 px x 160px and can operate at up to 3,000,000 frames per second in bursts of 28 images. Quantum efficiency of the PSI-4 camera CCD is 35% at 256 nm and 313 nm and is 55% at 660 nm. It is assumed that for the fluorescence spectrum of acetone, the quantum efficiency would be approximately 45%. The size of each pixel for the PSI-4 camera CCD is 115 μm x 115 μm (area of CCD is 18.4 mm x 9.2 mm), which is approximately 318 times larger than the physical area for a single pixel on the Sensicam QE

CCD. After taking into account optical fill factor and QE for each CCD (optical fill factor for PSI-4 CCD is 48% and optical fill factor for Sensicam QE CCD is approximately 80-81%) it is found that each pixel for the PSI-4 CCD will collect approximately 150 times more photons per pixel than the Sensicam. This is an increase of over two orders of magnitude in signal collected compared to the Sensicam and 4 orders of magnitude compared to the high-speed cameras tested in this work.

Combined with the success of the conventional acetone PLIF images, it is quite clear why we remain optimistic that 3-D LIF is a viable technique for 3-D density measurements. The key to implementation of 3-D LIF, however, will be the acquisition of a suitable high-speed camera to collect the relatively weak signal.

VII. Background Oriented Schlieren Wavefront Sensor

A unique development over the course of this project was the realization that a relatively simple flow visualization technique, background oriented schlieren (BOS) imaging can be used to measure the distortion of a wavefront passing through the flow field. Although not a part of the original research plan, development of this sensor was added to the objectives in light of its relevance to aero-optics and its potential to open doors for other researchers interested in the aero-optics problem, but not possessing traditional (and relatively expensive) wavefront sensors such as a Shack-Hartmann wavefront sensor. We note that this work did not take away significant resources from the other work described in the project. We describe the development of this sensor here as well as some ongoing efforts to further characterize and improve its performance.

A. Introduction

Traditionally, the distortion of an optical wavefront has been measured using a Shack-Hartmann Wavefront Sensor [(Neal, et al. 1998), (Lena 2009)], although earlier works have also described the applications of other wavefront sensors like the Malley probe [(Jumper and Fitzgerald 2001), (Malley, Sutton and Kincheloe 1992)]. This device uses a lenslet array and a CCD to discretize the incident wavefront and measure the local wavefront tilt. Each lenslet focuses the incident wavefront onto a focal spot on the CCD surface. The location of the spot on the CCD will change depending on the angle of incidence of the incident wavefront. Thus, by measuring the displacement of the spot, one can determine the local tilt of the wavefront and reconstruct the full 2-D wavefront using an array of lenslets. The resolution of the measurement is thus determined by the number of lenslets with the sensitivity dependent on the focal length of each of the lenslets. Although well developed, Shack-Hartmann wavefront sensors suffer from some limitations (Primot, Rousset and Fontanella 1990). For one, the spatial resolution is limited by the number of lenslets in the array and the number of pixels on the CCD required in determining the spot position. Second, the size of the measured wavefront is restricted to the size of the CCD, which is generally on the order of 10 – 15 mm. This latter point can be worked around using telescoping optics to reduce the beam aperture to the size of the sensor, but this increases system complexity and cost, and is limited by the size of available optics. In addition, a well collimated laser source is required to produce the incident wavefront upon which the measurement is made. Lastly, a complete system (laser source, collimating optics, sensor and software) can be quite expensive.

For aero-optic measurements in medium to large-scale wind tunnel facilities where the size of the wavefront to be measured is larger (order 2" or greater) and high spatial resolution is needed, these limitations can be difficult to overcome in an economical fashion. Presented here are preliminary results on the development of a new wavefront sensor based on the principles of background oriented Schlieren (BOS) imaging. Background oriented Schlieren imaging is a well developed technique that has the advantage that it is relatively simple and cost effective and can be used for the measurement of large aperture wavefronts. It requires only a CCD camera with lens, a random background and a light source to illuminate the background image. In fact, BOS has been demonstrated in real flight tests using a conventional CCD camera, a forest as a background and the sun as an illumination source.[(Raffel, Richard and Meier 2000), (Sommersel, et al. 2008), (Settles 1999)] As will be seen, the image distortion measured in a BOS experiment is directly related to the wavefront distortion, a fact which we seek to exploit to

obtain quantitative measurements of the wavefront distortion. In this regards, BOS has the potential to outperform Shack-Hartmann wavefront sensors with respect to spatial resolution, field-of-view and cost. The focus of this paper is on our preliminary efforts to adapt BOS for wavefront measurements. We present the fundamental principles of BOS with respect to wavefront measurements and show preliminary results obtained in a supersonic wind tunnel to demonstrate these capabilities.

B. BOS Wavefront Sensor Concept

Background Oriented Schlieren (BOS), as implied in the name, is a Schlieren based imaging technique where the refraction of light rays by density gradients in the flow is used as a means of flow visualization. The method varies from traditional Schlieren imaging, however, in that the deflection of light rays is detected by observing the spatial distortion of a background image as opposed to intensity gradients created using a large spherical mirror and a knife edge. While not as sensitive as traditional Schlieren, BOS is more amenable to quantitative analysis, a feature which is exploited in this work.

The basic concept of BOS is illustrated in Fig. 59. A CCD camera (shown here in a pinhole configuration) is used to capture an image of a target placed in the background of the flow field at a distance, s_o , from the camera lens. In the absence of any density gradients, light rays emitted from the center of the background will be imaged onto the center of the CCD, as shown by the solid line. In the presence of an inhomogeneous optical medium, however, light rays are deflected by an angle, ε , such that the center of the background is displaced by a distance, d_i , on the CCD. Thus, the influence of refraction is to shift the location on the CCD where an image is formed, leading to a distorted image. By imaging a background with high contrast, high frequency content, such as a random dot pattern, image processing algorithms can be applied to measure the local image displacement with subpixel accuracy. We use a PIV based algorithm due to its familiarity, however, optical flow algorithms are also applicable and have the potential to improve the performance described here.

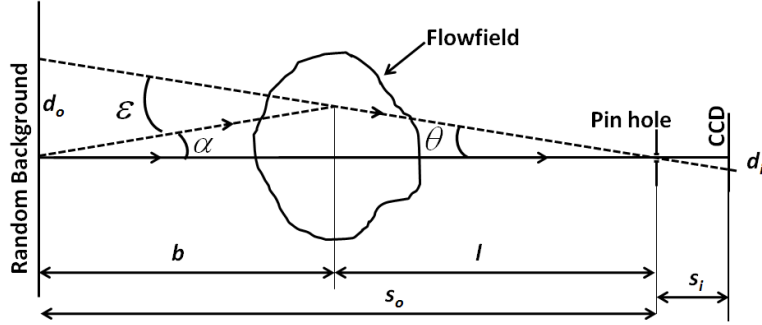


Figure 59. Schematic illustrating basic principles of background oriented Schlieren imaging. A pinhole is shown here instead of a lens for illustrative purposes.

For our application, we must relate the displacement, d_i , observed in the image to the refraction angle, ε . The procedure is fairly straightforward and based on geometrical optics. We note that a key element of this analysis is the assumption of a “thin” flow region relative to the distances l and b such that the effect of the flow can be modeled as thin interface located a distance, l , from the camera lens. We begin by considering the angles in Fig. 59 and noting the relationship:

$$\varepsilon = \alpha + \theta \quad (14)$$

These angles are further related using the trigonometric identity:

$$\tan \varepsilon = \tan(\alpha + \theta) = \frac{\tan \alpha + \tan \theta}{1 - \tan \alpha \tan \theta} \quad (15)$$

The angles α and θ are related to the distance from the flow to the background, b , and from the flow to the camera lens, l , using:

$$b \tan \alpha = l \tan \theta \quad (16)$$

Substituting Eq (16) into (15) for $\tan \alpha$, we arrive at

$$\tan \varepsilon = \frac{\left(\frac{l}{b} + 1\right) \tan \theta}{1 - \frac{l}{b} \tan^2 \theta} \quad (17)$$

For small angles (we measure angles of less than 1 mrad in this work), this reduces to:

$$\varepsilon \approx \tan \varepsilon = (1 + l/b) \tan \theta \quad (18)$$

From similar triangles, we have

$$\tan \theta = d_i / s_i \quad (19)$$

Which leads to:

$$\varepsilon = (1 + l/b)(d_i / s_i) \quad (20)$$

Where we note that b , l and s_i are constants from the experimental arrangement. Thus, Eq. 14 relates the refraction of a light ray to the measured image displacement for small angular deflections.

The angle, ε , shown in Fig. 59 and in Eq. 14 is a direct measurement of the wavefront distortion for every point in the image:

$$\varepsilon = \nabla(OPL) = \left(1 + \frac{l}{b}\right) \left(d_i / s_i\right) \quad (21)$$

The full 2-D wavefront, $OPL(x, y)$, can be reconstructed by considering the displacement measured at each location within the image. In this work, image displacements are calculated using PIV algorithms, which have proven to be capable of subpixel accuracy. Once the displacements are known, the local angle of the wavefront is calculated using Eq. 20 and the known values of l , b and s_i from the experimental setup.

To determine the magnitude of the wavefront itself, integration must be performed to reconstruct the distorted wavefront. Previous works on Shack-Hartmann wavefront sensors, which must also reconstruct the wavefront from local tilts, have generally used two methods for the reconstruction problem: discrete gradient based methods and iterative methods. [(Southwell 1980) Thurow et. al. (2003) describe a method whereby the wavefront is discretized and finite

difference approximations are applied for each point. The resulting matrix problem is then solved using a singular value decomposition (SVD) approach. This approach becomes computationally expensive with the increasing size of the vector matrix. Another approach, based on iteration, is described by Southwell. In this work, we use the approach described by Southwell, although both methods give similar results.

C. BOS Sensitivity

The sensitivity of a BOS wavefront sensor is determined by the minimum displacement that can be measured within the image. For this analysis, we model the image sensor as a CCD camera with 6.45 micron square pixels and resolution of 1376 x 1024 pixels (i.e. Cooke Corp. Sensicam QE) and assume 0.1 pixel accuracy in determination of displacements, which is consistent with the accuracy generally assumed in PIV image analysis. In addition, we also assume that the field-of-view (FOV) of the camera is held constant such that the full test section height of 4" remains in view for all configurations. This latter point is important when comparing our analysis to others found in the literature where the FOV is implicitly dependent on other parameters.

In examining Eq. 21, to first order, sensitivity can be improved by minimizing l/b (i.e. by placing the camera as close to the flow field as possible and moving the background as far away as possible) and by maximizing s_i (choosing a long focal length lens). Practical considerations related to the imaging conditions of the experiment, however, limit one's ability to arbitrarily adjust these parameters. As such, a more detailed analysis is conducted here.

The main constraint that we include in our analysis is the fact that both the test section and the background should be kept nominally in focus. The background must be kept in focus to produce a suitable image for displacement measurements whereas the test section should be kept in focus such that the corresponding location in the flow field can be properly identified. To satisfy this condition, we model the depth-of-field (DOF) of the imaging lens using the approach outlined in (Kingslake 1992). Figure 60 shows the schematic defining the DOF for a given aperture d on the lens. In this figure, the lens imaging condition (i.e. the thin lens equation) is set to focus on the plane located a distance S_f from the lens such that all points originating from this plane form a sharp focal point on the CCD sensor. Rays originating from in front of or behind the focal plane will appear blurred. The DOF is defined by the conical set of rays that fill a spot size, C (also known as the circle of confusion), on the object plane such that the blurred spot is indistinguishable from a spot formed from a point source on the object plane. The size of the spot is typically chosen to correspond to the size of a single pixel; however, this is a rather conservative value as displacements can be accurately determined for mildly blurred images. As will be seen, allowing some image blur can have significant benefits to the overall experiment. As can be seen in the figure, the total DOF consists of the region spanning from $S_f - L_1$ to $S_f + L_2$.

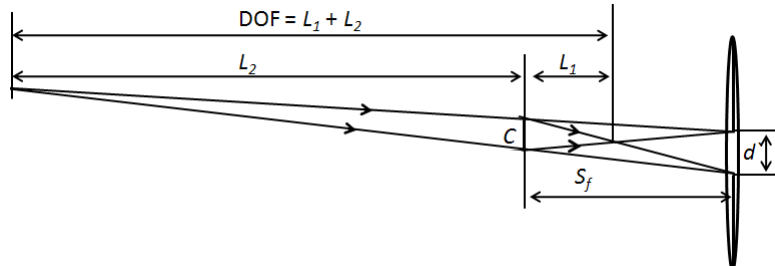


Figure 60. Schematic showing the effect of the lens aperture on the depth of field.

The procedure for calculating the DOF follows the geometry shown in Fig. 60 and is consistent with a geometric optics description of the problem (i.e. we do not include the effects of diffraction, which depend on the lens quality and usually become important for f-numbers of around 16-32). Briefly, we begin with the thin lens equation and associated magnification:

$$1/S_f + 1/S_i = 1/f \quad (22)$$

$$M = S_i / S_f \quad (23)$$

The circle of confusion in object space is related to the pixel size, p , in image space by:

$$C = p/M \quad (24)$$

Using the geometry shown in Fig. 2, it is then straightforward to show:

$$L_1 = \frac{CS_f}{d + C} \quad (25)$$

$$L_2 = \frac{CS_f}{d - C} \quad (26)$$

An important parameter that arises from this analysis is the f-number ($f/ \#$) of the lens, which is defined as the focal length divided by the lens aperture:

$$f\text{-number} = f/\# = \frac{f}{d}$$

Figure 61 shows the effect of the f-number and the focal distance S_f on the DOF for a lens with 75 mm focal length. As can be seen, the DOF increases with increasing S_f and increasing f-number. In the context of this work, both the test section and the background must be placed within the DOF of the lens.

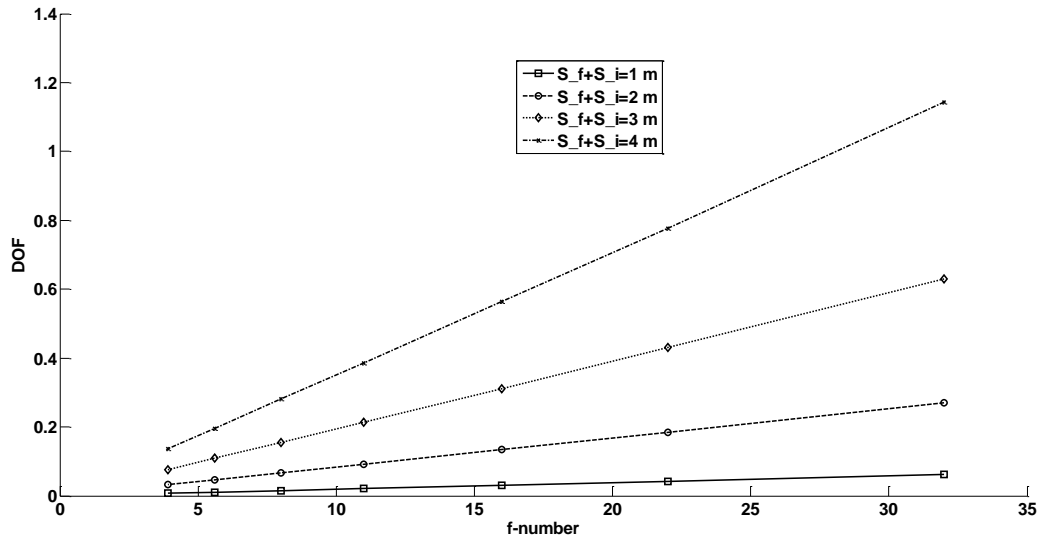


Figure 61. Effect of f-number and the S_f on the depth-of-field of the imaging setup.

To assess the capabilities of this technique in a practical environment, an analytical model that accounts for all of these effects was built in Matlab. As mentioned, both the type of camera and FOV are held constant to simulate the test environment of the Auburn University transonic wind tunnel, which has a 4" x 4" square test section. Three camera lenses were considered: a 25 mm focal length lens with maximum f/# of 16, a 50 mm focal length lens with maximum f/# of 22 and a 75 mm focal length lens with maximum f/# of 32. In the analysis that follows, we explore the influence of both the focal length and f/# of the lens on sensitivity. We do so under two imaging conditions. In the first case, we assume that the experiment is set up such that the test section is at the focal plane of the camera and the background is simply placed as far back while staying within the depth of field. The second case corresponds to the focal plane location optimally being adjusted such that the test section lies at the near DOF location (while still maintaining a FOV of 4" at this location) and the background lies at the far DOF location.

Figure 62 illustrates the change in sensitivity (as defined by minimum detectable angle) with focal length for both these cases. The f-number of all three lenses is held fixed at f/#=16. In both cases, the sensitivity remains almost constant contrary to increasing with increasing focal length, which is expected from Eq. 21. In the second case, the sensitivity is improved though nearly constant across the range of focal lengths considered here. This latter result is somewhat surprising as we expected focal length to play a more important role. It turns out that the increased sensitivity due to focal length is counteracted by the limited DOF and associated increase in the ratio l/b that is forced when one includes the effects of DOF. Optimizing the experimental arrangement to account for these effects balances these competing factors and leads to a situation where focal length is not important. This is a crucial point as longer focal length lenses also require a much larger experimental footprint, which may not be practical in some lab environments. In addition, a longer arrangement requires a larger background target and higher intensity illumination to cover a larger area.

The other factor considered here is the influence of lens f/# as larger f/# creates a larger DOF. Figure 63 illustrates the influence this has on the sensitivity for the 75 mm lens. Again, the background is placed at the furthest possible distance away as constrained by the lens DOF, however, the f-number of the lens is adjusted to limit this distance. The influence is striking with a nearly order of magnitude improvement allowed by operating the lens at the highest f-number possible. As mentioned, the DOF calculations assume a 1 pixel size circle of confusion. The image analysis procedure used here and based on PIV, however, is expected to remain accurate for even slightly blurred images. In fact, the accuracy of PIV is known to improve if the particles are intentionally blurred such that they are 2-3 pixels in diameter. We also note that PIV correlation algorithm typically use interrogation windows of 16 x 16 pixel size further reducing the demands on spatial resolution. The associated improvement in sensitivity is illustrated in Figure 63 where curves are shown for circles of confusion corresponding to 3 and 5 pixels, respectively. As can be seen, the potential gains in sensitivity are substantial.

We note that increasing the DOF has two limitations. For one, at high f/#'s the image resolution will eventually be limited by diffraction as opposed to the geometrical analysis considered here. Secondly, the amount of light collected decreases exponentially with increasing f/# such that a brighter illumination source is required. This latter point is somewhat circumvented, however,

by the realization that short focal length lenses can yield nearly the same sensitivity thus allowing for the background to be placed much closer to the camera.

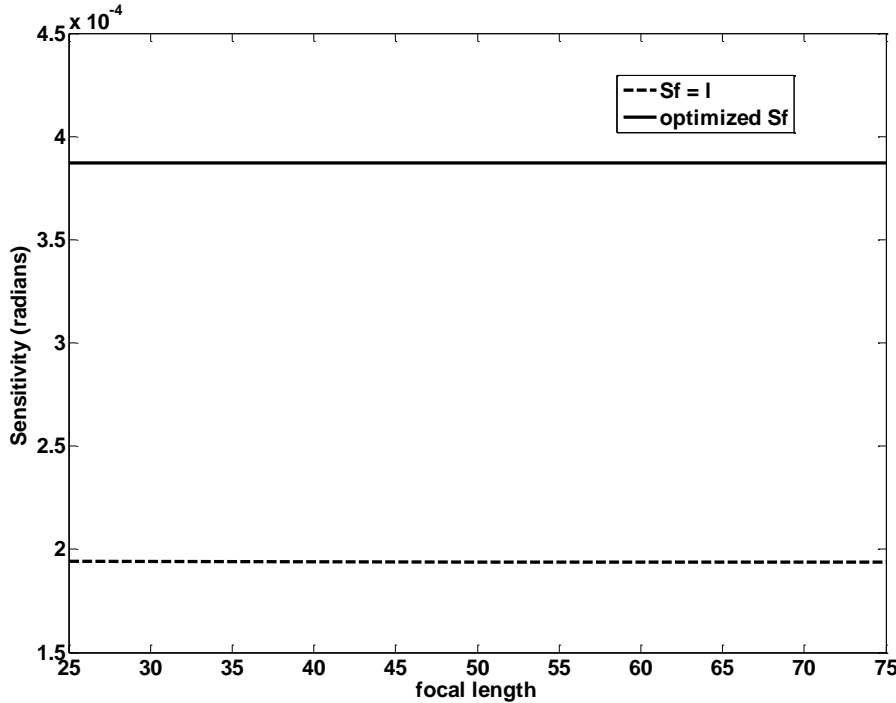


Figure 62. Effect on the sensitivity of the system with varying focal length lenses with the maximum f-number possible for each and keeping the 4" test-section in focus.

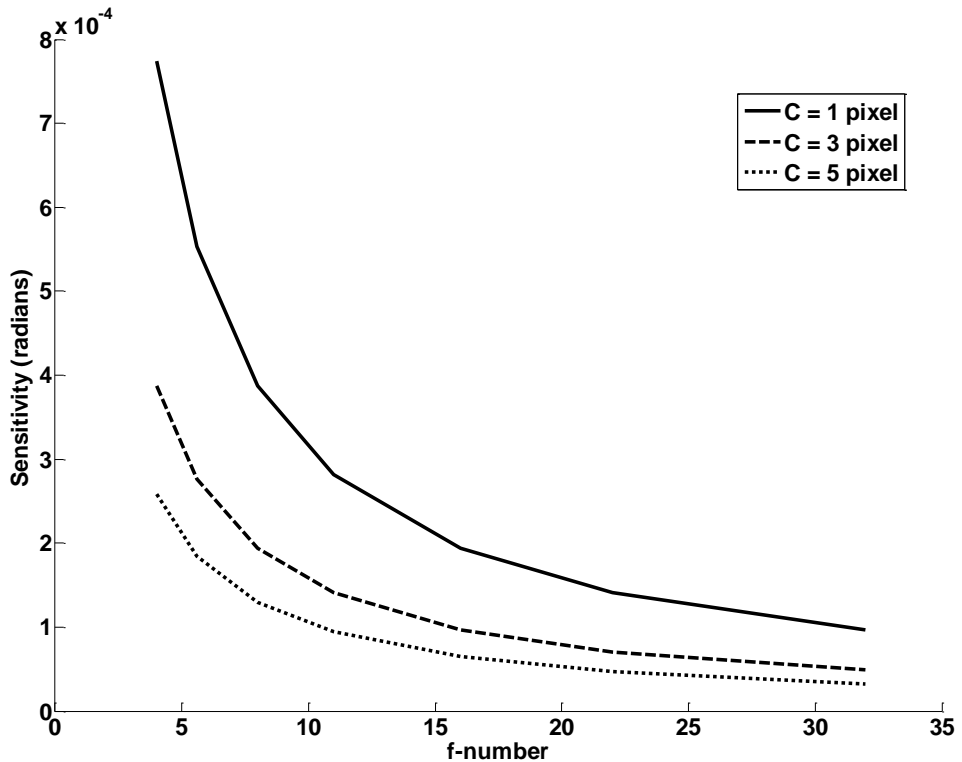


Figure 63. Effect of the f-number on the sensitivity of the system with 75 mm lens with 4" test-section in focus.

D. Test Case

To test the ability of BOS to be used for wavefront measurements, an experimental test case was generated using a cone placed in a supersonic flow. This flow was chosen as it creates a stable flow with large enough density gradients to create a measurable wavefront distortion. Perhaps more importantly, an analytical solution to the flow is possible by solving the Taylor-Maccoll equation (Eq.27), thus allowing us to compute the expected wavefront distortion values. Figure 64 shows a schematic of a cone placed in a supersonic flow and the resulting conical shock that originates from the nose. This is a well known problem described by the Taylor-Maccoll equation:

$$\frac{\gamma-1}{2} \left[V_{\max}^2 - V_r^2 - \left(\frac{dV_r}{d\theta} \right)^2 \right] \left[2V_r + \frac{dV_r}{d\theta} \cot \theta + \frac{d^2V_r}{d\theta^2} \right] - \frac{dV_r}{d\theta} \left[V_r \frac{dV_r}{d\theta} - \frac{dV_r}{d\theta} \left(\frac{d^2V_r}{d\theta^2} \right) \right] = 0 \quad (27)$$

where,

γ , ratio of specific heats of air,

V_r , velocity along the ray,

V_θ , velocity perpendicular to the ray,

θ , is the angle between the axis of the cone and the ray,

V_{\max} , is the square root of two time the stagnation enthalpy.

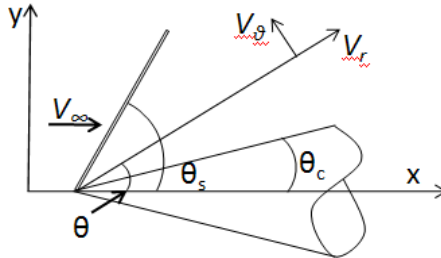


Figure 64. Schematic of the cone model.

Eq. 27, which is given in terms of θ and r was solved numerically to obtain a 2-D function of density. The field was then revolved azimuthally about the cone axis to produce a 3-D function of density for the flow behind the conical shock. The 3-D density data was then converted to index-of-refraction using Eq. 1 and integrated along the z-axis, according to Eq. 6 to simulate the wavefront distortion that would occur due to the presence of the cone. Figure 65 shows the resulting OPD for a 15.5° cone placed in a Mach 2.0 free stream. As can be observed, the conical shock produces a gradual wavefront distortion that increases in the downstream direction. Figure 65 presents the ideal case where there are no disturbances in the free stream and no boundary layers on the wind tunnel windows.

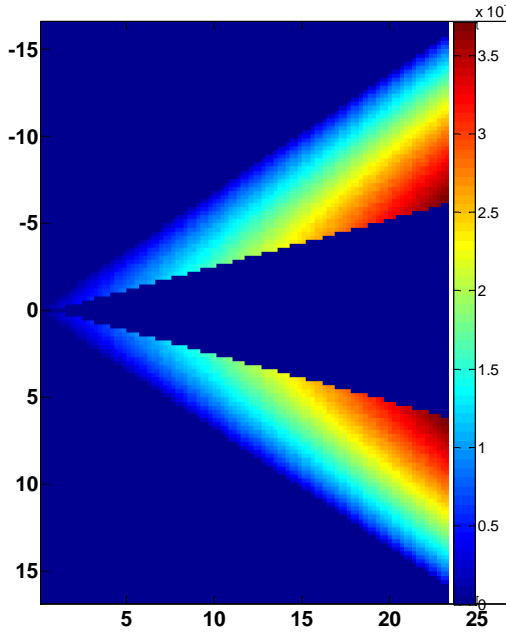


Figure 65. OPD for the analytical model generated in Matlab.

Experimental Arrangement

Experiments were conducted in the Auburn University Supersonic wind tunnel facility using a conical geometry nearly identical to that simulated above. The wind tunnel has a 4" x 4" cross-section and is capable of generating Mach numbers between 1.5 and 3.5. The tunnel Mach number was nominally set to Mach 2.0 for the current experiments with a sting mounted cone model placed in the test section. The 23 mm long, 12.77 mm diameter (15.5°) cone was connected to a 12.77 mm diameter cylinder. Figure 66 shows the typical experimental setup for the BOS experiments. The analytical model employed in the sensitivity analysis helped guide the details of the experimental arrangement. For the experiments discussed herein, space limitations limited us to a 50 mm focal length lens with f-number 22, s_t and s_o are 31.5 and 51 inches respectively. A General Radio 1539A strobeslave strobe light was used for the light source and the images were captures using a Cooke corporation sensicam qe camera at 10 Hz. Both the camera and the strobe light were controlled using a quantum composer digital pulse delay generator. The pulse duration for the strobe light was set at 10 usec and the exposure time on the camera was set at 5 usec. The random background used in the experiments was generated using the algorithm described by (Cook and DeRose n.d.) starting with a 768 X 768 sized random matrix.

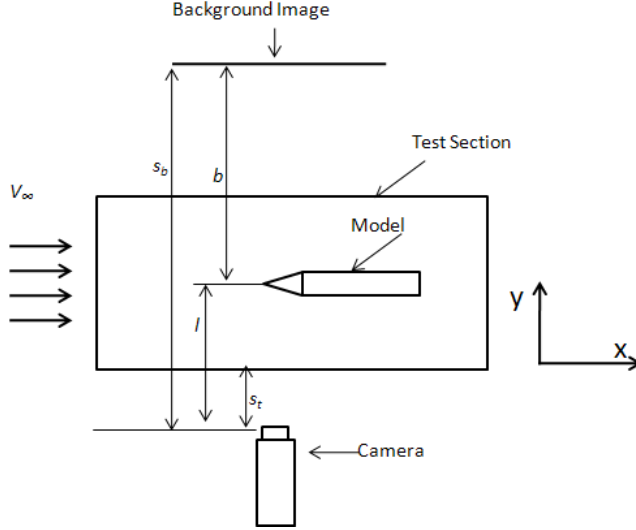


Figure 66. Schematic of experimental arrangement.

Raw images obtained from the experiments were then analyzed with the DPIVB software, PIV analysis software from Innovative Scientific Solutions Inc., Dayton, with 16 pixel X 16 pixel interrogation regions with a 50% overlap. No extra filters were used during the analysis. Deviation vectors thus obtained were analyzed in Matlab to generate the distorted wavefront.

Experimental Results

Three types of data were collected during the experiments: a) background image with no flow; b) background with flow but no model; and c) the background with model in the flowfield.

No Flow

Several images were acquired under static conditions (i.e. no flow). These images served several purposes. One, the images form the reference image from which displacements are to be calculated. Secondly, these images can be used to assess the noise floor of the measurement system such that the time-dependent effect of lighting intensity, uniformity, camera noise and other non-flow related factors can be assessed. Figure 67 shows a raw image of the background. The illumination is non-uniform and brighter at the center of the image, which is an artifact of the strobe lighting employed in this experiment. We have found enough image information in the dark wings of the image to determine accurate displacement values throughout the entire image. This ability is enhanced by the 12-bit resolution of the camera. PIV analysis of different pairs of flow images gave an average displacement of 0.008 pixels, which is an indication of the stability of the experimental arrangement and small compared to the general assumption of 0.1 pixel accuracy in the PIV based calculations.

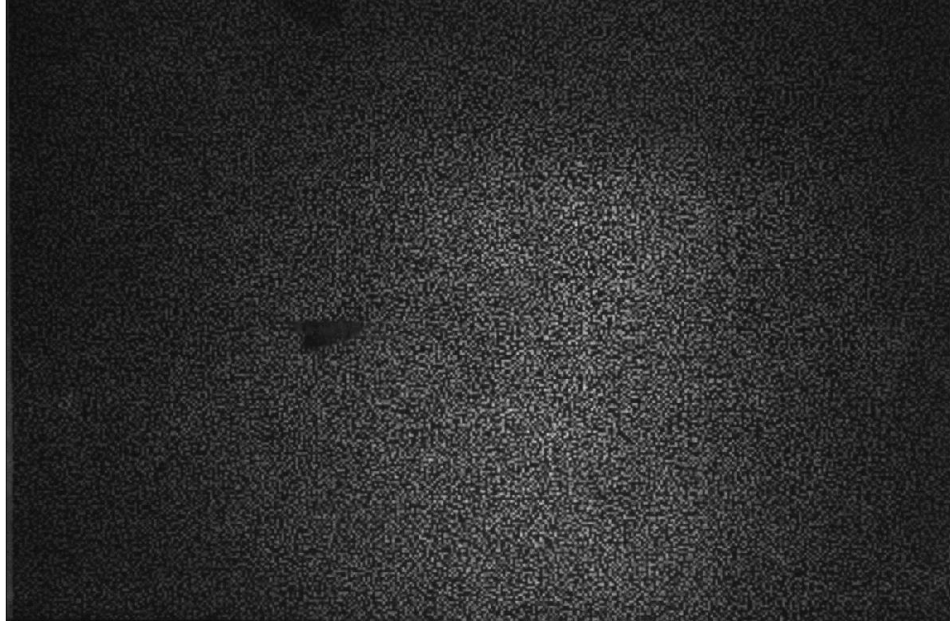


Figure 67. Background image with no flow.

Model Free Flow

Ideally, the cone would be the only source of density changes in the flow; however, boundary layers on the tunnel walls and Mach waves associated with supersonic flow will also distort the wavefront passing through the flow. In addition, vibrations can also play a role as the movement of the tunnel windows will create a uniform shift in the background image. To assess the magnitude of these effects, the tunnel was run without the cone model. Figure 68 shows the displacement vectors calculated from one representative image during the tunnel run. The vectors are displayed at 5 times their relative size to emphasize their magnitude, which would be difficult to observe otherwise. In this instance, the average magnitude of displacement is 0.3 pixels. This value was found to decrease in subsequent images, presumably due to the drop in test section pressure that occurs over the duration of a single run. One interesting observation from these images is the appearance of Mach waves originating on the upper surface of the tunnel, a characteristic that is typical in conventional Schlieren images and illustrative of the sensitivity of the technique.

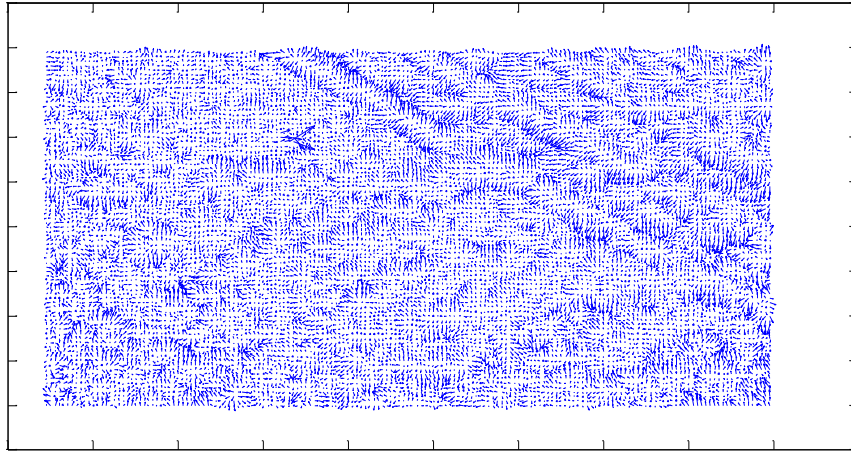


Figure 68. Displacement vectors calculated for Mach 2.0 flow without the cone model present.
All vectors shown are 5 times the actual size.

Cone Model

Experiments on the cone model were conducted at Mach 2.0. Figure 69 shows an instantaneous (flash duration of 5 microsecond) raw image acquired with the cone in place. Both the background and cone appear to be in focus. This image was correlated with the no-flow image shown above with the instantaneous displacement vectors shown in Figure 70. The appearance of the cone shock is quite apparent. In addition, the formation of an expansion fan at the trailing edge of the cone is also observed as well as another set of shocks associated with fins placed at the rear of the model. In addition, it can be observed that the free stream flow ahead of the shock also experiences displacement due to the turbulent boundary layer formed on the wind tunnel walls, as shown in the previous section.

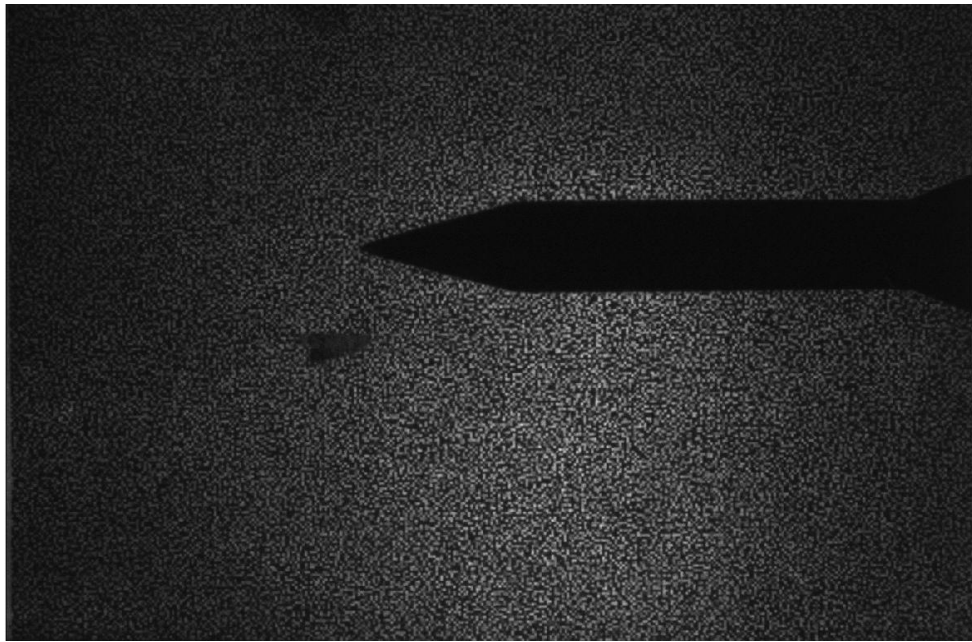


Figure 69. Raw image of the cone model in Mach 2.0 flow.

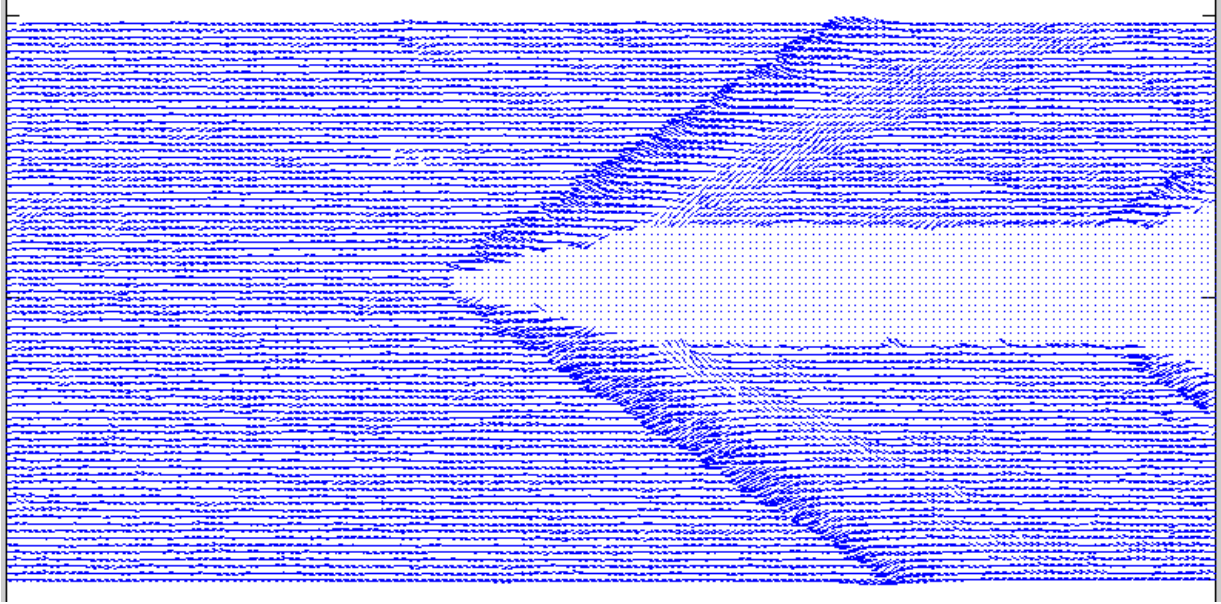


Figure 70. Instantaneous deviation vectors obtained from correlating the Mach 2.0 images with no flow images. All vectors in the image are twice the actual size.

The displacement data was used to reconstruct the wavefront distortion resulting from this flow field as described. The wavefront is shown in Figure 71. Qualitatively, the features are similar to that observed in the analytical model shown in Figure 65. One difficulty in comparing the two images is the influence of the tunnel boundary layers on the wavefront distortion. In an effort to minimize this influence, the wavefront was calculated using only the displacement values found behind the shock. This wavefront is shown in Figure 72. It also qualitatively agrees with that shown in Figure 65. More importantly, the magnitude of the change in OPL across the cone is close to that predicted with the analytical model. It was not possible to determine an average wavefront distortion as the cone model was found to vibrate during experiments. This also has the effect of creating an asymmetric geometry (i.e. the instantaneous position of the cone possessed a non-zero angle of attack) such that the assumptions employed in the analytical cone solution are strictly not valid.

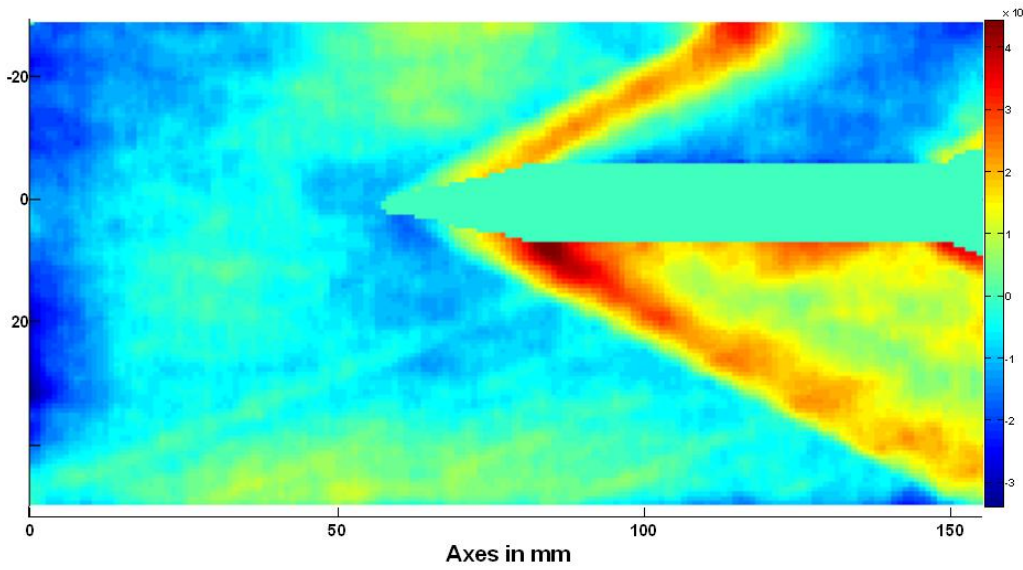


Figure 71. Reconstructed wavefront using the iterative method.

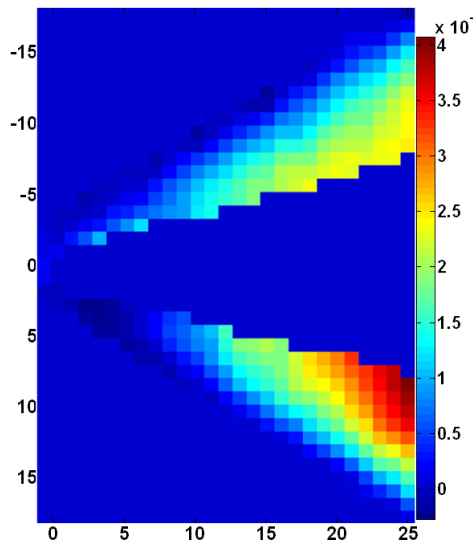


Figure 72. Reconstructed wavefront after the values ahead of the shock are made equal to zero.

E. BOS Wavefront Sensor Conclusions

The use of BOS imaging is shown to be a viable technique for wavefront measurements. An analytical sensitivity analysis of the BOS wavefront sensor showed accuracy of measuring deviation vectors up to 20 micro-radians. It is found that the sensitivity of the BOS wavefront sensor is a function of the focal length and f-number of the lens when restricted by the field-of-view and DOF of the imaging system. In an optimized configuration taking advantage of the full DOF available, it is found that the sensitivity only mildly depends on focal length and primarily depends on the lens f/#, which should be as large as possible.

An analytical Mach 2.0 flow over a cone was generated to obtain an analytical wavefront distortion. Experiments were also conducted at Mach 2.0 in the supersonic wind tunnel. The deformed wavefront was generated from the experimental data. When compared with the wavefront generated from the analytical procedure, both wavefronts agree qualitatively. This shows the practical applicability of the BOS technique as a wavefront sensor. Simple equipment like the stable light source, camera and any regular lens makes BOS a low cost wavefront sensor.

A detailed and more specific comparison of the BOS wavefront sensor to the Shack-Hartmann sensor is planned along with a further error analysis and the study of limitations of the technique. Application of the BOS wavefront sensing to more generalized turbulent flows, like flow behind the hemisphere in transonic flow, are also planned.

VIII. Synergistic Activities

One of the outcomes of this 3 year effort was the development of professional relationships with other researchers involved in AFRL research. These relationships were fostered through the annual program review meetings held by AFOSR as well as the presentation of this work at professional conferences (e.g. AIAA Aerospace Sciences Meeting). Some specific examples include recent communications with Dr. Michael Ol about the prospects of implementing a high-speed 3-D PIV system for 3-D velocity measurements of the unsteady flow fields visualized in his water tunnel. It is expected that this relationship will lead to a collaborative effort in the future to employ these advance diagnostics in an AFRL facility. Additional activities include the presentation of seminars at the University of Notre Dame and Georgia Tech. The seminar at Notre Dame was hosted by Dr. Eric Jumper and Dr. Stanislav Gordeyev, both of whom are actively working with the Air Force on aero-optics. These discussions led to the development of an NSF proposal where the PI proposed to use simultaneous PIV/PLIF to measure the time resolved velocity and density field in a compressible shear layer. The proposed work is a direct consequence of the interaction between the PI and the ND research group. More recent conversations with Dr. Ari Glezer and Georgia Tech have focused on the potential application of 3-D imaging for analysis of unsteady 3-D flow effects on several projects related to AFOSR sponsored work.

IX. Conclusions and Future Work

The work conducted here resulted in several positive developments that should greatly enhance future research efforts related to aero-optics and other compressible flow problems. The major outcome of this work was the development of an acetone PLIF system for density measurements in compressible flow fields. It was shown that this technique is practical for application in conventional wind tunnel environments and capable of revealing some of the most important features of a turbulent compressible flow including shock waves, the flapping motion of a turbulent wake and the density fluctuations associated with the low pressure region at the core of vortices formed in a weakly compressible shear layer. With the proper instrumentation, this technique can be adapted for use in facilities with higher Mach numbers and/or larger test sections. In addition, the technique can potentially be extended to provide 3-D density measurements if the proper high-speed camera technology is available. Outside of this work, very few options exist to measure the instantaneous density field of a compressible flow field. Thus, this work is expected to have an impact far beyond that of the aero-optics work discussed here.

Related to the acquisition of high resolution density images, computational tools were also developed to virtually project an optical wavefront through the flow field. These tools are essential for using acetone PLIF in an aero-optics context. By defining a beam aperture size and propagation direction, integration through the acquired density data yielded OPD measurements for the turbulent flow behind a hemisphere. Preliminary data using these tools showed that for an angle looking back through the shear layer/wake region, the flapping motion of the wake plays a larger role than the formation of smaller vortices in the shear layer between the wake and free stream.

Another development related to aero-optics was the assessment of the use of background oriented Schlieren (BOS) imaging for wavefront measurements. Analysis of the BOS concept and preliminary experiments clearly indicated that BOS presents a low-cost alternative for the acquisition of wavefront distortion data in high-speed wind tunnels. In addition, BOS allows for the measurement of large aperture wavefronts that might be not be feasible through other means.

While the development of these diagnostics represents the most noteworthy outcome of this work, effort was also made to apply these tools for aero-optic relevant measurements. To facilitate such an application, a special transonic test section was designed and constructed to produce a Mach 0.78 flow so that separating flow behind a hemisphere could be examined. Acetone PLIF measurements of this flow field were used to examine the shock-induced separation on top of the hemisphere, the low density cores associated with the separated shear layer and the large-scale flapping motion of the hemisphere's wake. These measurements showed that the density drops in the vortex cores are significant (up to 50%) and greater than might be initially expected. This was an important observation as it helped clarify/validate the notion that compressibility effects can lead to significant decrease in density at the core of a

vortex, thus better defining the relationship between the turbulent flow and wavefront distortions. The measurements also indicated that the flapping motion of the wake is even more significant from an aero-optics perspective as the high density free stream and low density wake are generally marked by a relatively sharp interface with large scale fluctuations in its location.

In terms of future work, the work discussed herein does an excellent job of laying the ground work for more detailed aero-optic investigations, but did not produce an extensive enough set of data for a comprehensive analysis of this particular flow field. In terms of the turret geometry investigated in this work, it is recommended that a follow on effort utilize a more powerful laser and more sensitive camera to visualize a larger field of view such that the shock induced separation region and the full extent of the wake can be visualized at a single instant. In addition, the image processing algorithms should employ a more robust flat field calibration to reduce bias errors. With these changes implements, a large set of data would allow for advanced analysis such as POD to be employed to characterize the flow and explore the relationship between the separation point and the large-scale motion of the wake. The images presented here hinted that different modes of wake behavior are possible. Future work should also allow for different Mach numbers, so that the influence of Mach number can be better understood.

With this said, the diagnostics developed here also have the potential to be applied to investigate more canonical flow problems, such as a simple planar free shear layer where the nature of density fluctuations within a structure are still poorly understood. This problem would be fairly easy to investigate using a simultaneous PIV/PLIV experiment. In fact, a proposal to the National Science Foundation was recently submitted to explore this problem. The fundamental nature of density measurements in compressible flow fields is bound to have implications in other geometries and compressible flow problems as well.

X. Works Cited

Adrian, R J, and J Westerweel. *Particle Image Velocimetry*. New York, New York: Cambridge University Press, 2011.

Aggarwal, M, and N Ahuja. *On Cosine-fourth and Vignetting Effects in Real Lenses*. Urbana, Illinois: IEEE, 2001.

Aguirre, R C, J C Nathman, P J Garcia, and H J Catrakis. "Turbulent Refractive Fluid Interfaces and Aero-Optical Wavefront Distortions: Experiments and Computations." *AIAA Paper 2005-1080*. 2005.

Bell, J H, and R D Mehta. *Contraction Design for Small Low-Speed Wind Tunnels*. Stanford, California: Joint Institute for Aeronautics and Acoustics - National Aeronautics and Space Administration - Ames Research Center - Stanford University, 1988.

Braeuer, A., F. Beyrau, and A. Leipertz. "Laser-induced fluorescence of ketones at elevated temperatures for pressures up to 20 bars by suing a 248 nm excitation laser wavelength: experiments and model improvements." (*Applied Optics*) 45, Number 20 (2006).

Brassard, Daniel. *Transformation of a Polynomial for a Contraction Wall Profile*. Ontario, Canada: Undergraduate Student, Lakehead University, 2003.

Brokaw, R.S. "Predicting Transport Properties of Dilute Gases." (*Industrial and Engineering Chemistry Process Design and Development*) 8, Number 2, pp. 240-253 (1969).

Bryant, R.A., J.M. Donbar, and J.F. Driscoll. "Acetone laser induced fluorescence for low pressure/low temperature flow visualization." (*Experiments in Fluids*) 28, pp. 471-476 (2000).

Cain, A.B., T.T. Ng, E.J. Jumper, D.J. Wittich, D. Cavalieri, and E.J. Kerschen. "An Optical Propagation Improvement System and the Importance of Aeroacoustics." Seattle, Washington: AIAA - 39th Plasmadynamics and Lasers Conference, 2008.

Catrakis, H. *Equipment for Aero-Optical Flow Imaging*. Irvine, California: Final Report, Air Force Office of Scientific Research, University of California (UC) - Irvine, 2004.

Catrakis, H.J. *Aero-Optical Wavefront Propagation and Refractive Fluid Interfaces in Large-Reynolds-Number Compressible Turbulent Flows*. Irvine, California: Final Report to the Air Force Office of Scientific Research, University of California (UC) - Irvine, 2006.

Catrakis, H.J., P.J. Garcia, and J.C. Natham. "Cumulative Aero-Optical Interactions Along Laser Beam Propagation Paths: Experiments and Computations." Reno, Nevada: American Institute of Aeronautics and Astronautics (AIAA) - 44th AIAA Aerospace Sciences Meeting and Exhibit, 2006.

Catrakis, H.J., R.C. Aguirre, and J. Ruiz-Plancarte. "Large-scale dynamics in turbulent mixing and the three-dimensional space-time behaviour of outer fluid interfaces." (*Journal of Fluid Mechanics - Cambridge University Press*) 471, pp. 381-408 (2002).

Chew, L, and W Christiansen. "Experimental investigation of transitional free shear layer optics." *AIAA Journal* 31 (1993): 2290-2295.

Choi, H.J., Y.S. Ko, and S.H. Chung. "Visualization of Concentration Field in a Vortex Ring Using Acetone PLIF." (*Journal of Visualization*) 5, No. 2, pp. 145-152 (2002).

Clemens, N.T. *Flow Imaging*. New York: Encyclopedia of Imaging Science and Technology, John Wiley and Sons, 2002.

Cook, R.L., and T. DeRose. "Wavelet Noise." *Pixar Animation Studios*. <http://graphics.pixar.com/library/WaveletNoise/paper.pdf> (accessed 2010).

Danehy, P.M., et al. "Planar laser-induced fluorescence (PLIF) investigation of hypersonic flowfields in a Mach 10 wind tunnel (invited)." San Francisco, California: 25th AIAA Aerodynamic Measurement Technology and Ground Testing Conference, 2006.

Dean, J.A. *Lange's Handbook of Chemistry Fifteenth Edition*. New York, New York: McGraw-Hill, Inc., 1999.

Dimotakis, P.E., H.J. Catrakis, and D.C. Fourguette. "Flow structure and optical beam propagation in high-Reynolds-number gas-phase shear layers and jets." (*Journal of Fluid Mechanics - Cambridge University Press*) 433, pp.105-134 (2001).

Fitzgerald, E.J., and E.J. Jumper. "The optical distortion mechanism in a nearly incompressible free shear layer." (*Journal of Fluid Mechanics - Cambridge University Press*) 512, pp.153-189 (2004).

Ghaemi, S., Schmidt-Ott, A., and Scarano, F. "Nanostructured tracers for laser-based diagnostics in high-speed flows." (*Measurement Science and Technology*) 21 (2010).

Gierczak, T., J.B. Burkholder, S. Bauerle, and A.R. Ravishankara. "Photochemistry of acetone under tropospheric conditions." (*Chemical Physics*) 231, pp. 229-244 (1998).

Gordelyev, S., and E. Jumper. "Fluid Dynamics and Aero-Optical Environment Around Turrets." Notre Dame, Indiana: AIAA, 2009.

Gordelyev, S., and E. Jumper. "Fluid dynamics and aero-optics of turrets." (*Progress in Aerospace Sciences*) 46, pp. 388-400 (2010).

Gordelyev, S., E. Jumper, B. Vukasinovic, A. Glezer, and V. Kibens. "Fluidic Control of a Turret Wake, Part II: Aero-Optical Effects." Orlando, Florida: 47th AIAA Aerospace Sciences Meeting and Exhibit, 2009.

Gordelyev, S., E.J. Jumper, T.T. Ng, and A.B. Cain. "Aero-Optical Characteristics of Compressible, Subsonic Turbulent Boundary Layers." Orlando, Florida: 34th AIAA Plasmadynamics and Lasers Conference, 2003.

Gordelyev, S., M.L. Post, T. McLaughlin, J. Ceniceros, and E.J. Jumper. "Aero-Optical Environment Around a Conformal-Window Turret." (*American Institute of Aeronautics and Astronautics (AIAA) Journal*) 45, No. 7 (2007).

Gordelyev, S., T.E. Hayden, and E.J. Jumper. "Aero-Optical and Flow Measurements Over a Flat-Windowed Turret." (*American Institute of Aeronautics and Astronautics (AIAA) Journal*) 45, No. 2 (2007).

Hanson, R.K. *Laser Diagnostics for Reacting Flows*. Stanford, California: Final Technical, Air Force Office of Scientific Research, Stanford University, 2010.

Hartwig, J.W. *Acetone-LIF at Elevated Pressure and Temperature for 282NM Excitation: Experiments and Modeling*. Cleveland, Ohio: Case Western Reserve University, 2010.

Hirschfelder, J.O., C.F. Curtiss, and R.B. Bird. *Molecular Theory of Gases and Liquids*. New York, New York: John Wiley & Sons, Inc., 1954.

Houghton, E.L., and P.W. Carpenter. *Aerodynamics for Engineering Students Fourth Edition*. New York, New York: Halsted Press An imprint of John Wiley & Sons, Inc., 1993.

Hugo, R. J., E. J. Jumper, Havener, and C Stepanek. "Time-resolved wavefront measurements through a compressible free shear layer." *AIAA Journal* 35 (1997): 671.

Jumper, E., and E. Fitzgerald. *Recent Advances in Aero-Optics*. University of Notre Dame - Notre Dame, Indiana and The Boeing Company - Houston, Texas: Progress in Aerospace Sciences - Pergamon - Elsevier Science Ltd., 2001.

Jumper, E.J. *Adaptive Optics for Turbulent Shear Layers*. Notre Dame, Indiana: Final Report, Air Force Office of Scientific Research, University of Notre Dame, 2006.

Kearney, S.P., and F.V. Reyes. "Quantitative temperature imaging in gas-phase turbulent thermal convection by laser-induced fluorescence of acetone." *(Experiments in Fluids)* 34, pp. 87-97 (2003).

Kingslake, R. *Optics in Photography*. Bellingham, Washington: SPIE Optical Engineering Press, 1992.

Koch, J.D., R.K. Hanson, W. Koban, and C. Schulz. "Rayleigh-calibrated fluorescence quantum yield measurements of acetone and 3-pentanone." *(Applied Optics)* 43, No. 31, pp. 5901-5910 (2004).

Kohse-Hoinghaus, K., and J.B. Jeffries. *Applied Combustion Diagnostics*. New York, New York: Taylor & Francis, 2002.

Laskaris, N. *Vignetting*. Edinburgh, Scotland: University of Edinburgh.

Laufer, G. *Introduction to Optics and Lasers in Engineering*. New York, New York: Cambridge University Press, 1996.

Lena, Pierre. "Adaptive optics: a breakthrough in astronomy." *Experimental Astronomy* 26 (2009): 35-48.

Lozano, A. *Laser-Excited Luminescent Tracers for Planar Concentration Measurements in Gaseous Jets - PhD Dissertation*. Stanford, California: Stanford University, 1992.

Malley, M M, G W Sutton, and N Kincheloe. "Beam-Jitter Measurements of Turbulent Aero-optical Path Differences." *Applied Optics* 31 (1992).

Mani, A., Wang, M., and Moin, P. *Computational study of aero-optical distortions by a turbulent wake*. Notre Dame, Indiana: Center for Turbulence Research Annual Research Briefs, 2006.

Merzkirch, W. *Flow Visualization - Second Edition*. Orlando, Florida: Academic Press, Inc., 1987.

Mourits, F.M., and F.H.A. Rummens. "A critical evaluation of Lennard-Jones and Stockmayer potential parameters and of some correlation methods." (*Canadian Journal of Chemistry*) 55, pp. 3007-3020 (1977).

Murakami, E., and D. Papamoschou. "Eddy Convection in Coaxial Supersonic Jets." (*AIAA Journal*) 38, Number 4, pp. 628-635 (2000).

Neal, D R, E Hedlund, M Lederer, A Collier, Charles Spring, and Bill Yanta. "Shack-Hartmann Wavefront Sensor Testing of Aero-Optic Phenomena." *AIAA Paper 98-2701*. 1998.

Nygren, J., et al. "Three-Dimensional Laser Induced Fluorescence of Fuel Distributions in an HCCI Engine." (*Proceedings of the Combustion Institute*) 29, pp. 679-685 (2002).

Ponder, Z.B., Rennie, R.M., Abado, S., and Jumper, E.J. "Span-wise Wavefront Measurements Through a Two-Dimensional Weakly-Compressible Shear Layer." Chicago, Illinois: American Institute of Aeronautics and Astronautics (AIAA) - 41st Plasmadynamics and Lasers Conference, 2010.

Primot, J, G. Rousset, and J.C. Fontanella. "Deconvolution from wave-front sensing: a new technique for compensating turbulence degraded images." *Journal of the Optical Society of America* 7, no. 9 (1990): 1598-1608.

Raffel, M, H Richard, and G. E. A. Meier. "On the Applicability of Background Oriented Schlieren Tomography for Large Scale Aerodynamic Investigations." *Experiments in Fluids* 28 (2000): 477-481.

Raffel, M., Willert, C.E., Wereley, S.T., and Kompenhans, J. *Particle Image Velocimetry A Practical Guide Second Edition*. New York, New York: Springer-Verlag Berlin Heidelberg, 2007.

Ragni, D., Schrijer, F., can Oudheusden, B.W., and Scarano, F. "Particle tracer response across shocks measured by PIV." (*Experiments in Fluids*) 2010.

Reid, J.Z., Lynch, K.P., and Thurow, B.S. "Further Development of a High-Speed 3-D Density Measurement Technique for Aero-Optics." Chicago, Illinois: American Institute of Aeronautics and Astronautics (AIAA) - 40th Fluid Dynamics Conference and Exhibit, 2010.

Reid, R.C., J.M. Prausnitz, and T.K. Sherwood. *The Properties of Gases and Liquids Third Edition*. New York, New York: McGraw-Hill Book Company, 1977.

Rennie, M., Z. Ponder, S. Gordeyev, A. Nightingale, and E. Jumper. "Numerical Investigation of Two-Dimensional Compressible Shear Layer and Comparison to Weakly Compressible Model." Monterey, California: Directed Energy Professional Society Beam Control Conference, 2008.

Schrijer, F.F.J., Scarano, F., and van Oudheusden, B.W. "Application of PIV in a Mach 7 double-ramp flow." (*Experiments in Fluids*) 41, pp. 353-363 (2006).

Settles, G S. "Schlieren and Shadowgraph Imaging in the Great Outdoors." *Proceedings of PSFPIV-2*. Honolulu, 1999.

Sommersel, O K, D Bjerketvedt, S O Christensen, O Kerst, and K Vaagsaether. "Application of background oriented schlieren for quantitative measurements of shock waves from explosions." *Shock Waves* 18 (2008): 291-297.

Southwell, W. H. "Wave-Front Estimation from Wave-Front Slope Measurements." *Journal of Optical Society of America* 70 (1980): 998-1006.

Stanek, M, N Sinha, J Seiner, B Pearce, and M Jones. "High Frequency Flow Control - Suppression of Aero-Optics in Tactical Directed Energy Beam Propagation and the Birth of a New Model (part I)." *AIAA Paper 2002-2272*. 2002.

Thurber, M.C. *Acetone Laser-Induced Fluorescence for Temperature and Multiparameter Imaging in Gaseous Flows - PhD Dissertation*. Stanford, California: Stanford University, 1999.

Thurow, B, M Samimy, and W Lempert. "Simultaneous High-Resolution Optical Wavefront and Flow Diagnostics for High-Speed Flows." *AIAA Paper 2003-3613*. 2003.

Thurow, B, M Samimy, W Lempert, S Harris, J Widiker, and B Duncan. "Simultaneous MHz Rate Flow Visualization and Wavefront Sensing for Aero-optics." *AIAA Paper 2003-0684*. 2003.

Thurow, B.S. and Lynch, K.P. "Development of a High-Speed Three-Dimensional Flow Visualization Technique." (*AIAA Journal*) 47, No. 12 (2009).

Thurow, B.S., Satija, A., and Lynch, K.P. "Third-generation megahertz-rate pulse burst laser system." (*Applied Optics*) 48, No. 11 (2009).

Tran, T. *Acetone Planar Laser-Induced Fluorescence and Phosphorescence for Mixing Studies of Multiphase Flows at High Pressure and Temperature*. Atlanta, Georgia: Georgia Institute of Technology, 2008.

Tran, T., Y. Kochar, and J. Seitzman. *Measurements of Acetone Fluorescence and Phosphorescence at High Pressures and Temperatures*. Atlanta, Georgia: American Institute of Aeronautics and Astronautics, Inc. (AIAA) - Georgia Institute of Technology, 2006.

Troe, J. "Theory of thermal unimolecular reactions at low pressures. II. Strong collision rate constants. Applications." (*The Journal of Chemical Physics*) 66, Number 11, pp. 4758-4775 (1977).

Trolinger, J. "High Speed Digital Wavefront Sensing for Aero-Optics and Flow Diagnostics." *20th International Congress on Instrumentation in Aerospace Simulation Facilities (ICIASF)*. Gottingen, Germany, 2003.

Truman, C R, and M J Lee. "Effects of Organized Turbulence Structure on the Phase Distortion in a Coherent Optical Beam Propagating Through a Turbulent Shear Flow." *Physics of Fluids* 2 (1990): 851-857.

Urban, W.D. and Mungal, M.G. "Planar Velocity Measurements in Compressible Mixing Layers." Reno, Nevada: AIAA - 35th Aerospace Sciences Meeting, 1997.

Vukasinovic, B., A. Glezer, S. Gordeyev, E. Jumper, and V. Kibens. "Fluidic Control of a Turret Wake, Part I: Aerodynamic Effects." Orlando, Florida: American Institute of Aeronautics and Astronautics (AIAA) - 47th AIAA Aerospace Sciences Meeting Including The New Horizons Forum and Aerospace Exposition, 2009.

Wall, David. "Design of a Solid Wall Transonic Wind Tunnel." Huntsville, Alabama: American Institute of Aeronautics and Astronautics (AIAA) - AIAA Region II Student Conference, 2009.

Wyckham, C.M., Zaidi, S.H., Miles, R.B., and Smits, A.J. "Characterization of Optical Wavefront Distortions Due to a Boundary Layer at Hypersonic Speeds." Orlando, Florida: American Institute of Aeronautics and Astronautics (AIAA) - 34th AIAA Plasmadynamics and Lasers Conference, 2003.

Yanta, W J, et al. "Near- and Far-field Measurements of Aero-Optical Effects Due to Propagation Through Hypersonic Flows." *AIAA Paper 2000-2357*. 2000.

Zhao, Y., Han, Y., Fan, Z., Qiu, F., Kuo, Y., Kaufman, A., and Mueller, K. *Visual Simulation of Heat Shimmering and Mirage*. Kent, Ohio: Kent State University, To appear at IEEE Transactions on Visualization and Computer Graphics.

Zheng, Y., Lin, S., and Kang, S.B. *Single-Image Vignetting Correction*. Shanghai Jiaotong University and Microsoft Research Asia.